Tunneling Injection and Recombination of Carriers in Self-Assembled Quantum Dots

Amrik Richard Chaggar, MSci (Hons)

Thesis submitted to the University of Nottingham
for the degree of Doctor of Philosophy

October 2008

Abstract

This thesis describes an experimental investigation of the resonant injection of carriers into self-assembled indium arsenide (InAs) quantum dots incorporated in the intrinsic region of gallium arsenide (GaAs) p-i-n resonant tunneling diodes, and of the resulting electroluminescence spectrum associated with carrier recombination in the quantum dots, wetting layer and GaAs matrix. A series of devices of different designs have been measured and it is shown that *bipolar resonant injection*, i.e. resonant injection of both electrons and holes, into the zero-dimensional states provided by the InAs quantum dots is possible. It is shown that bias-tunable tunneling of carriers into the dots provides a means of controlling injection and light emission from a small number of individual dots within a large ensemble. Magnetotunneling spectroscopy is used to investigate the possibility that fluctuations in the potential profile of the GaAs emitter layer play a significant role in the carrier dynamics of such devices. We also show that the extent of carrier energy relaxation prior to recombination can be controlled by tailoring the morphology of the quantum dot layer.

Additionally, a study into the phenomenon of low-temperature up-conversion electroluminescence (UCEL) is presented. Injection of carriers into the quantum dot states at an applied bias well below the GaAs flat-band condition results in near-band-edge GaAs electroluminescence, i.e., emission of photons with energies much larger than that supplied by the applied bias and the thermal energy. The origin of this UCEL is discussed and is attributed to carrier excitation resulting from (non-radiative) Auger recombination of electron-hole pairs in the quantum dot ground states.

Acknowledgements

The completion of a thesis cannot take place without the help and advice of a surprisingly large number of people:

Firstly my supervisors, Laurence Eaves and Amalia Patanè, who were always enthusiastic and willing to share their knowledge. The group post-docs, Lyuda, Oleg and especially Andreas, who all helped me with experiments and ideas. Thanks also to Mohamed Henini at Nottingham and Mark Hopkinson and Robert Airey at Sheffield for the growth and fabrication of the samples used in this thesis, and to Erik Stock and Prof. Dieter Bimberg at TU Berlin for collaborating on the micro-electroluminescence measurements in Chapter 5. I am also indebted to EPSRC for providing my funding during the past three years.

The time and help of all the support staff at Nottingham was also greatly appreciated, in particular Chris Pallender, Malcom Carter, Dave Holt and Steve Tabreham, who were invaluable in helping to keep my experiments running.

It would be remiss of me not to thank those people who, while hindering rather than helping my work rate, certainly made my time at Nottingham immensely more enjoyable. Olly, Giles and Spas, who made for the kind of office it's a pleasure to work in. Vicki, Chris, Adam and Jacs for all the lunches. The tea-room crew for some great nights out and the excellent conversations. Dan, Helen, Jimbo, Pete, Shannon and Sweets for the constant flow of emails. The guys in the Dave Jephcote XI and Tangerine Monolith for some awesome football and anyone I forced to play cricket.

Thank you to my family for their greatly appreciated love, support and encouragement, and to Amanda, David and Bill for being such great "in laws" and for the many relaxing breaks. Finally I'd like to thank Charlotte, for dealing with having a physicist for a boyfriend with grace and understanding, and for simply making my life better by being in it.

List of publications

Publications

1. L. Turyanska, A. Baumgartner, A. Chaggar, A. Patanè, L. Eaves, and M. Henini, "Sharp-line electroluminescence from individual quantum dots by resonant tunneling injection of carriers", *Applied Physics Letters*, **89**, 092106, (2006).

2. A. Baumgartner, L. Turyanska, A. Chaggar, A. Patanè, L. Eaves and M. Henini, "Sharp Electroluminescence Lines Excited by Tunneling Injection Into a Large Ensemble of Quantum Dots", *Proc. Physics of Semiconductors, 28th International Conference*, **CP893**, 759, (2007)

3. A. Baumgartner, A. Chaggar, A. Patanè, L. Eaves, and M. Henini, "Upconversion electroluminescence in InAs quantum dot light-emitting diodes", *Applied Physics Letters*, **92**, 091121, (2008).

Contents

Introduction

A *quantum dot (QD)* is a nanostructure that confines the motion of a carrier in all three spatial dimensions. QDs were first investigated over 20 years ago [1, 2] and have continued to be the subject of considerable research, see for example the review by Yoffe [3]. Much of the early interest in these structures stemmed from their status as "artificial atoms" [4, 5] with strong analogies to the discrete energy levels of atoms that exist in nature. The highly quantised nature of QDs gives rise to a δ-like density of states, with the number of states at a given energy directly related to the number of QDs and the degeneracy of the state. The small size of a QD also leads to strong many-body effects, meaning that the properties of the dot can be changed significantly by adding one extra carrier. One advantage of quantum dots over actual atoms is that their properties can be changed and controlled by electrostatic gates, modified dot geometries and material composition [6].

The ability to isolate single electronic states has made QDs a favoured medium for investigating the transport of single carriers. Single electron transport and many-body effects have been investigated extensively both theoretically [7, 8] and experimentally [9, 10]. Excellent reviews of both the theory and experimental observation of electron transport in QDs exist in the literature [11, 12]. Investigations of the photoluminescence (PL) of QD ensembles [13] and individual QDs [14] have also been carried out.

This thesis investigates InAs self-assembled quantum dots (SAQDs), which can be induced to form during the epitaxial growth of a semiconductor crystal. SAQDs are typically smaller in size and thus have stronger confining potentials

than lithographically defined quantum dots [15]. SAQDs are relatively easy to fabricate and process into useable devices, making them an important tool in investigating the properties of zero-dimensional systems. Commercial devices, such as lasers and photo-detectors, based on SAQDs are already available and investigations continue into their suitability as single particle sources for use in quantum information processing. With the amount of research being carried out on InAs SAQDs, it seems likely that they will have an important role to play as a basis for future novel devices and as a tool for investigating the fundamental physics of low-dimensional systems.

The structure of the thesis is as follows:

Chapter 1 gives an introduction to the composition of the samples grown for this thesis and a brief summary of low-dimensional systems is provided. The main focus of the chapter is a literature review of the development and relevance of InAs SAQDs for applications.

Chapter 2 discusses the concept of resonant tunneling of carriers in semiconductor structures. The discussion is extended to encompass specific theories and techniques based upon resonant tunneling that are relevant to this thesis.

Chapter 3 gives a summary of all the samples used in the experiments that have gone into this thesis. Details of the experimental apparatus and techniques are also provided.

Chapter 4 is an experimental chapter investigating a series of resonant tunneling diodes in order to prove the concept of bipolar resonant injection into an ensemble of QDs.

Chapter 5 is an experimental chapter building upon the work of Chapter 4 and looking at using bipolar resonant injection to induce photon emission from a single quantum dot within a large ensemble.

Chapter 6 presents a study of the phenomena of up-conversion electroluminescence in semiconductor diodes.

Chapter 7 presents an investigation into the effect of a magnetic field on the current-voltage characteristics of a QD ensemble. Magnetotunneling spectroscopy (MTS) is used to map the electron wave-function for the QD ground state.

Chapter 8 draws together the conclusions of this thesis and presents the prospects for future work in this area.

Chapter 1

Material properties and low-dimensional systems

1.1 Material properties

The samples studied in this thesis are made from a combination of three semiconductor alloys: GaAs, AlAs and InAs. All three are III-V compounds with a zinc-blende structure consisting of two interpenetrating face-centered cubic sub-lattices. GaAs and InAs are direct gap materials with the lowest point in the conduction band occurring at the Γ-point of the Brillouin zone. AlAs is an indirect gap material with the lowest point in the conduction band occurring at the X-point. Table 1.1 shows a list of the relevant properties of these materials.

Property	GaAs	AlAs	InAs	Unit
Lattice constant (300K)	0.5653	0.5660	0.6058	nm
LO phonon energy (300K)	36	50	30	meV
Band gap (300K)	1.42	2.15	0.35	eV
Band gap (0K)	1.52	2.23	0.42	eV
Heavy hole mass	0.5	0.5	0.41	m_e
Light hole mass	0.082	0.15	0.026	m_e
Electron mass	0.067	0.150	0.022	m_e
Dielectric constant	13.2	10.2	15.1	
Electron mobility (300K)	0.92		3.3	$m^2V^{-1}s^{-1}$
Hole mobility (300K)	0.04		0.05	$m^2V^{-1}s^{-1}$

Table 1.1: Material properties of GaAs, AlAs and InAs. Data from Davies 1998 [16].

1.2 Low-dimensional systems

Consider an electron inside a three-dimensional box of sides L_x, L_y and L_z, where the potential inside the box is zero and outside is infinity. The wave function of the electron in the box is given by

$$\Psi = \sin(\frac{n_x \pi x}{L_x}) \sin(\frac{n_y \pi y}{L_y}) \sin(\frac{n_z \pi z}{L_z}), \tag{1.1}$$

where n_x , n_y and n_z are positive integers [17].

The corresponding density of states per unit energy and per unit volume is

$$n_{3D}(E) = \frac{m^*}{\pi^2 \hbar^3} \sqrt{2m^* E}, \tag{1.2}$$

where E is the carrier energy and m^* is the carrier effective mass.

Reducing the number of dimensions in which carriers are free to move leads to a change in the density of states. Figure 1.1 shows the density of states versus

carrier energy for a three dimensional (bulk), a two dimensional (quantum well), a one dimensional (quantum wire) and zero dimensional (quantum dot) system.

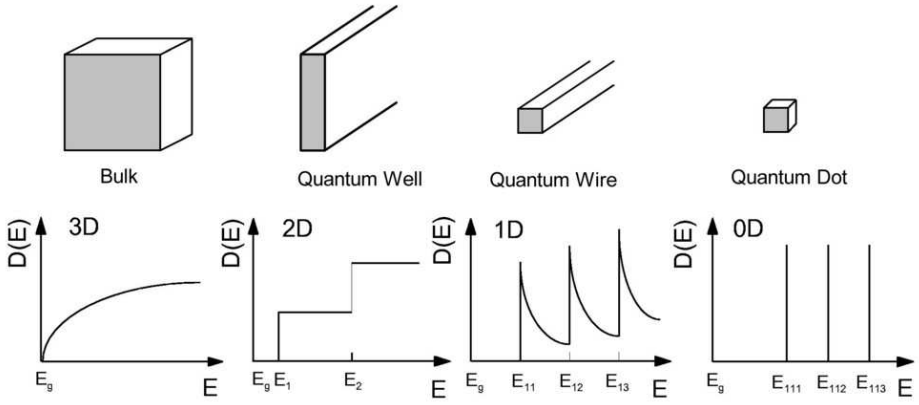

Figure 1.1: Density of states versus energy for a 3D, 2D, 1D and 0D system. The subscripts of the energy axis correspond to the energy eigenvalues of the Schrödinger equation. Figure taken from http://www-opto.e-technik.uni-ulm.de/lehre/cs/DOS-DIM.jpg.

Reducing L_x, L_y or L_z in equation 1.1, such that the carriers become confined in a given direction, for example along the z-axis, leads to a quantisation of the kinetic energy of carriers along the z-axis. The energy of a carrier confined along z is given by

$$E = E_z + \frac{\hbar^2(k_x^2 + k_y^2)}{2m^*}, \tag{1.3}$$

where k_x and k_y are the k-vectors in the x and y directions, respectively. This equation consists of two parts, the first is the contribution of the quantised energy in the z-axis and the second is due to the kinetic energy of the carriers in the x-y plane. For a QW of infinite depth E_z is given by

$$E_n = \frac{\hbar^2 \pi^2}{2m^* L_z^2} n^2, \tag{1.4}$$

where the set of states for a given, integer value of n is referred to as a *sub-band*.

The density of states for each 2D sub-band is given by

$$n_{2D}(E) = \frac{m^*}{\pi \hbar^2} \tag{1.5}$$

and is independent of the energy.

In semiconductors this type of quantum-well (QW) system can be achieved, for example, by placing a thin layer of GaAs between two barriers of AlAs, and devices such as this have been studied extensively throughout the literature [18]. A quantum wire is a structure in which carriers are confined in all but one dimension, meaning that properties such as the conductance of the wire become quantised [19]. Quantum dots are nanoscale structures in which the carriers are confined in all three spatial dimensions. There are a number of ways to make quantum dots, for example: epitaxial Stranski-Krastanov growth, lithographic processing and synthesis from precursor compounds to create colloidal QDs.

1.2.1 InAs/GaAs self-assembled quantum dots

Much of the early fabrication of QDs was carried out starting from a two-dimensional system and using etching, nanolithography, or thin film processing to create zero-dimensional structures, see for example Randall *et al.* [20], Lee *et al.* [21] and Kitada *et al.* [22]. These techniques are capable of producing QDs

of ∼100nm in size. However, a major advance in the field was made possible by the use of molecular beam epitaxy (MBE) and metal-organic vapour-phase epitaxy to produce QDs of the order of 10-50nm in lateral size [23].

MBE was initially developed in the mid-1960s [24] and is a process allowing the deposition of single crystals. Atoms of the desired growth material are subliminated from a solid source and are deposited onto a heated substrate in collimated beams. After deposition the atoms diffuse on the surface prior to their incorporation into the growing crystal. The kinematics of the growth has a substantial effect on the morphology of the final structure and is influenced by a number of factors such as surface temperature, deposition rates and the material properties [25].

The Stranski-Krastanov morphology occurs in systems where there is an appreciable lattice mismatch between the constituent materials, such as the 7% mismatch between InAs and GaAs. Initially the InAs forms a single, near uniform, wetting layer (WL) on top of the GaAs layer, but, as more material is deposited, the strain build-up causes a transition from a two-dimensional to a three-dimensional growth regime accompanied by the formation of islands, also called SAQDs. Figure 1.2(a) shows a schematic diagram of a strained semiconductor crystal forming an InAs WL and QDs in GaAs. Figure 1.2(b) shows a cross-sectional scanning tunneling microscope (X-STM) image of an InAs QD.

The formation of InAs QDs and the structural properties of the crystals containing them is still a topical area of research [27]. Of particular importance to the electronic structure and optical properties of the final system is the formation of the 2D WL [28] and the morphology of the QDs [29].

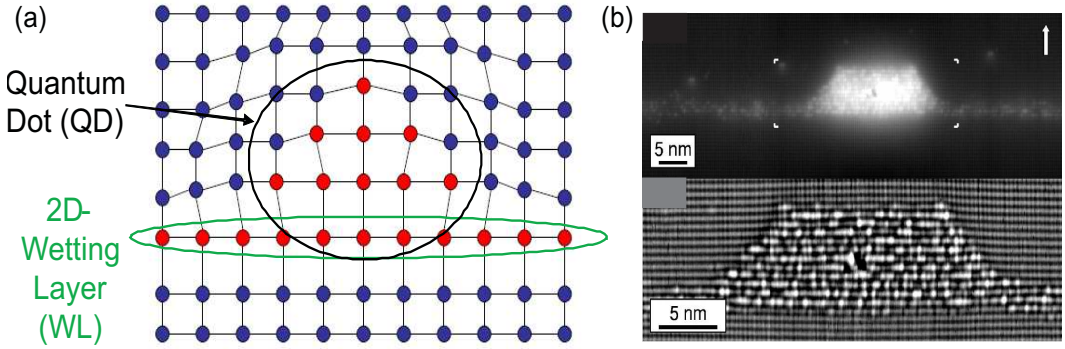

Figure 1.2: Formation of InAs QDs and WL in a GaAs matrix due to Stranski-Krastanov growth. (a) Schematic diagram showing a strained GaAs/InAs/GaAs heterostructure. The built-in strain leads to the formation of a WL and QDs. (b) The top half of the figure shows a X-STM image of an InAs/GaAs QD, the arrow indicates the growth direction. The bottom half of the figure shows a filtered section, indicated by the four markers, of the top image. Image taken from Gong *et al* (2004) [26].

Fluctuations in the size of the QDs arise naturally as a consequence of the growth process. The distribution of dot sizes is approximately Gaussian and leads to a similar distribution of energy levels for the dots [30]. QDs like the ones studied in this thesis have been shown to have an average lateral size of 18.7±4.2nm and a height of 4.5±1.7nm, as measured by scanning tunneling microscopy (STM) [31].

The electronic energy levels of SAQDs are generally difficult to model. This is due to several factors including the complex strain profile caused by the lattice mismatch between InAs and GaAs, indium segregation effects, the three-fold degeneracy of the valence band maximum and the strong confinement of carriers inside the dot [32]. The situation is further complicated by the strong Coulomb effects exhibited by the dots when they are occupied by more than one carrier [33, 34] and the presence of the 2D WL [35, 36]. Much work has gone into the theoretical and experimental characterisation of the electronic

structure of QDs [37, 38, 39, 40, 41] as this is the basis for understanding and exploiting their optical and transport properties.

Much of the experimental work on SAQD systems has focussed on isolating individual QDs in order to observe single photon emission. Emission from individual QDs in a lithographically patterned cross-gate device [42] has been observed, as has single photon emission from QDs situated in the active channel of an etched small-area (2μm) device [43]. There has also been work on single-photon devices that use the Coulomb blockade effect to control the injection of single electrons and holes [44]; however, this type of device requires that the electron and hole-charging energies are large compared to the thermal energy, thus limiting the experiment to low temperatures (T$\leq$1K). Michler *et al* [45] have demonstrated single photon emission from a single quantum dot situated in a microcavity structure, while Yuan *et al* [46] have used electroluminescence (EL) from a single quantum dot as an electrically driven single-photon source.

InAs-based semiconductor lasers offer high performance devices in the 1.3μm range used for short-haul telecommunications [47, 48, 49], which is one of the reasons for the interest in the InAs/GaAs system. A collaboration between Fujitsu Ltd and a group at the University of Tokyo has led to the development of a 1.3μm QD laser with a 10 gigabit per second operating capacity and excellent temperature stability, which is to be made commercially available [50].

$In_xGa_{1-x}As$ QD infra-red photodetectors [51] and other novel devices are being developed utilising the optical and electronic properties of SAQDs. Borgström *et al* [52] are proposing that QDs situated in nanowires could be used to construct QD molecules, and work by Kroutvar [53] has demonstrated how a

QD based device could potentially be developed as a new type of computer memory. Photon emission due to carrier recombination in QDs could also lead to the development of single photon sources for quantum information processing and quantum cryptography [54, 55].

The wide range of applications in which InAs QDs are finding use makes them an important current and future technology. The aim of this thesis is to investigate the carrier dynamics in InAs SAQDs via resonant electrical injection of carriers into QDs incorporated in a light emitting p-i-n diode.

Chapter 2

Quantum tunneling in semiconductor heterostructures

2.1 Electron tunneling

In a classical system, when a particle with energy ϵ encounters a potential barrier of height $V > \epsilon$, the particle is reflected from the barrier. In a quantum mechanical system, however, the particle always has a finite probability of passing through the barrier due to the spreading of the particle wave-function. Likewise, a particle with $\epsilon > V$ will also have a finite chance of being reflected from the barrier, even though classically it would always pass over it. In this chapter electron tunneling through a single barrier (2.1.1) and double barrier system (2.1.3) is considered in detail.

2.1.1 Single barrier tunneling

A layer of (AlGa)As sandwiched between two GaAs layers creates the potential profile shown in Figure 2.1.

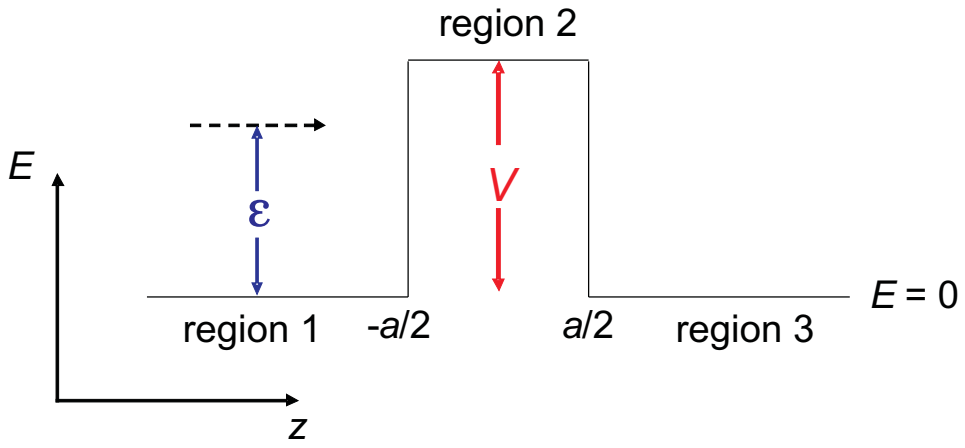

Figure 2.1: Schematic diagram showing a particle with energy ϵ incident on a barrier of width a and height V.

The system shown in Figure 2.1 is described by the one-dimensional Schrödinger equation 2.1

$$\left[\frac{-\hbar^2}{2m^*}\frac{\partial^2}{\partial z^2} + V(z)\right]\Psi(z) = \epsilon\Psi(z), \tag{2.1}$$

where ϵ is the energy of the incident particle, $V(z)$ is the potential and Ψ is given by equation 2.2

$$\Psi(z) = \begin{cases} Ae^{ik_1 z} + Be^{-ik_1 z} & (z < -a/2) \\ Ce^{ik_2 z} + De^{-ik_2 z} & (-a/2 < z < a/2) \\ Fe^{ik_3 z} & (z > a/2) \end{cases} \tag{2.2}$$

where $k_1 = k_3$ and k_2 are the wave-vectors of the particle in the three areas of the potential shown in Figure 2.1.

Solving equation 2.1 and matching Ψ and $\partial\Psi/\partial z$ at $z{=}\pm\frac{a}{2}$ allows the coefficients A, B, C, D and F, and hence the *transmission probability*, i.e. the probability the that the particle will *quantum tunnel* through the barrier, to be obtained, i.e.

$$T(\epsilon) = \left[1 + \frac{V^2}{4\epsilon(\epsilon - V)} sin^2 k_2 a\right]^{-1}. \tag{2.3}$$

Equation 2.3 shows the solution for the regime where $\epsilon{>}V$. The solution for $\epsilon{<}V$ is given by

$$T(\epsilon) = \left[1 + \frac{V^2}{4\epsilon(V - \epsilon)} sinh^2 \kappa_2 a\right]^{-1}, \tag{2.4}$$

where

$$k_2 = \left[\frac{2m^*(\epsilon - V)}{\hbar^2}\right]^{\frac{1}{2}} \tag{2.5}$$

and

$$\kappa_2 = \left[\frac{2m^*(V - \epsilon)}{\hbar^2}\right]^{\frac{1}{2}}. \tag{2.6}$$

Figure 2.2 shows a plot of the transmission probability versus ϵ for $a = 10$nm and $V = 300$meV. For $\epsilon{<}V$, *T(ϵ)* decays rapidly to zero with decreasing energy. For $\epsilon{>}V$, the *T(ϵ)* curve exhibits resonances whenever $k_2 a$ is a multiple of π.

At these values of k_2, $T(\epsilon)$=1, as expected for the transmission in classical mechanics.

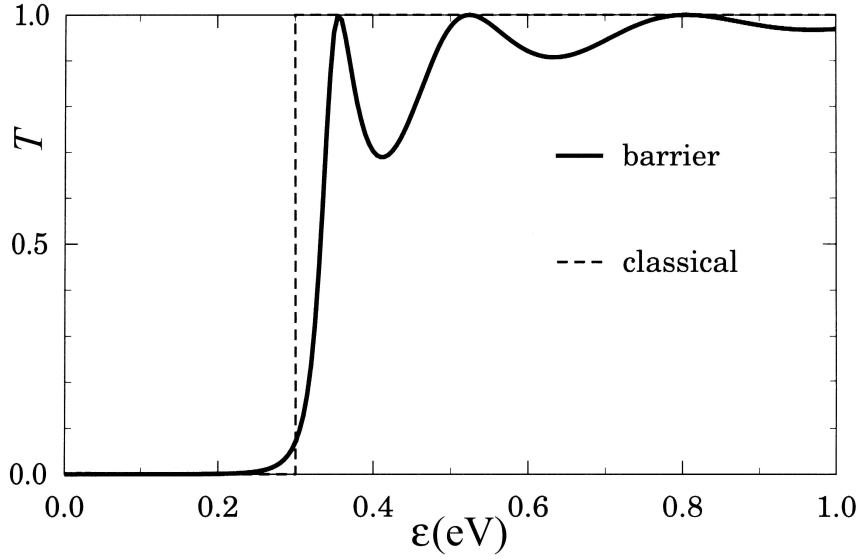

Figure 2.2: Transmission probability T as a function of incident particle energy ϵ for a single barrier of height V=300meV and width a=10nm. The dashed line shows the classical transmission probability. Figure taken from Davies 1998 [16].

The situation described above is for an ideal square barrier. However, in real semiconductor systems the potential is more likely to vary in space due, for example, to an applied voltage or a built-in potential. This case is discussed in section 2.1.2.

2.1.2 WKB Theory

The Wentzel–Kramers–Brillouin (WKB) theory is a useful method to solve the Schrödinger equation of systems with a potential that varies along a given direction, e.g. z. It considers the case in which the change in the wave-number k per unit wavelength is smaller than k itself. Using the WKB method, T can be expressed as [16]

$$T \approx exp\left[-2\int \kappa(z)dz\right], \tag{2.7}$$

where

$$\kappa(z) = \frac{\sqrt{2m^*(V(z)-\epsilon)}}{\hbar}. \tag{2.8}$$

We now apply equation 2.7 to the problem of tunneling through a triangular barrier, such as that generated by the in-built potential of a p-i-n diode, where i refers to the undoped, or intrinsic, central region of the diode. Figure 2.3 illustrates the case in which electrons are injected from the n-contact layer into a given energy state of a QD.

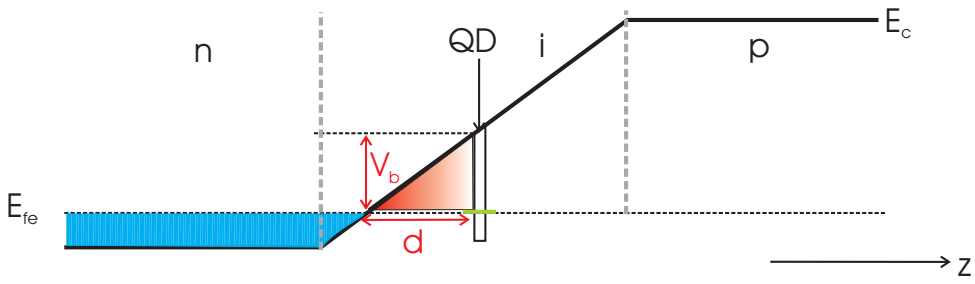

Figure 2.3: Schematic diagram showing the conduction band for an electron tunneling through a triangular barrier (shaded red) of width d and height V_b into a QD state. E_{fe} denotes the electron Fermi energy in the n-type contact layer of the p-i-n diode.

The barrier potential for an electron at the Fermi energy E_{fe} in Figure 2.3 is given by

$$V(z) = V_b\frac{z}{d}. \tag{2.9}$$

Substituting 2.8 and 2.9 into 2.7 with ϵ=0 gives the transmission probability of an electron tunneling through a triangular potential barrier of width d and height V_b, i.e.

$$T \approx exp\left[-\left(\frac{2m^*V_b}{\hbar^2}\right)^{\frac{1}{2}} d\right]. \tag{2.10}$$

The situation is analogous for the case of holes tunneling from the p-layer.

This discussion of electron tunneling through a single barrier provides a reasonably good description but neglects some important points, which are listed below.

i The tunneling interface is assumed to be abrupt and planar as indicated in Figure 2.3. It is obvious that this is not the case as any electrons not exactly at the Fermi edge will have a greater tunneling distance to the one assumed in the calculation of T (equation 2.10).

ii The barrier is assumed to have a triangular shape with sharp edges. However, in a p-i-n diode the potential profile varies more smoothly throughout the structure.

iii The WKB method can be used only for slowly varying potentials. In a lattice with a high level of strain, such as that caused by the mismatch between InAs and GaAs, this may not be the case.

iv The effective mass is taken as a constant value along z. However, an electron or hole tunneling from one material to another will have a mass-dependent energy relative to the band-edge, which will vary across the structure.

v In the structures studied in this thesis the barrier energy is large compared to the Fermi energy and thermal distribution of carriers in the emitter. This allows us to approximate all carriers as having the same transmission probability, i.e. all carriers tunnel from a single, well defined energy state.

vi Coulomb interaction effects have been neglected and only independent tunneling of electrons and holes in the p-i-n diode has been considered.

vii The barrier is assumed to be uniform in the x-y plane. Thus, only the energy resulting from motion in the z direction is important for the calculation of the transmission probability.

2.1.3 Double barrier resonant tunneling

In section 2.1.1 the case of tunneling through a single, thin barrier system was considered. Introducing a second, similar barrier a distance w from the first to form a QW can lead to the formation of *quasi-bound* states between the barriers. The states are referred to as quasi-bound as the wave-functions of carriers in these states penetrate through the barriers, so the carriers will only be bound for a finite time, characteristic of the individual QW. The confinement of carriers in this way is analogous to that of photons in the Fabry-Pérot etalon in optics. Figure 2.4 shows a schematic diagram of a double barrier resonant tunneling system, such as that created by sandwiching a layer of GaAs between two AlAs barriers. This type of system is known as a resonant tunneling diode (RTD).

When the energy of the impinging carrier, E, is not close to the energy of either of the quasi-bound states then the total transmission probability, T, is

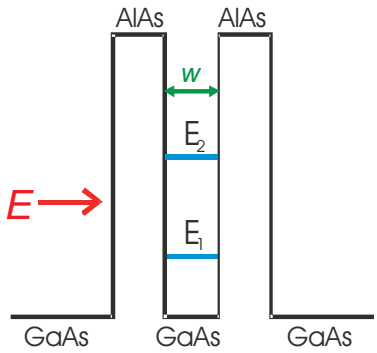

Figure 2.4: Schematic diagram showing an AlAs/GaAs RTD. The system is shown in 1D and at zero applied bias. The QW is of width w and has two quasi-bound energy states, E_1 and E_2. The arrow indicates the energy of an electron impinging on the left barrier.

given by the product of the two single barrier transmission probabilities, T_L and T_R, and depends exponentially on the energy of the impinging carrier and the thickness of the barriers. However, when E becomes close to the energy of a quasi-bound state T increases dramatically, rising well above the product of T_L and T_R. In the resonant regime T is given by

$$T(E) \approx T(E_n)\left[1+\left(\frac{E-E_n}{\frac{1}{2}\Gamma}\right)^2\right]^{-1}, \tag{2.11}$$

where E_n denotes a particular quasi-bound state and Γ is the width of the resonance for an electron of velocity v, and is given by

$$\Gamma = \frac{\hbar v}{2w}(T_L + T_R). \tag{2.12}$$

$T(E_n)$ is the peak transmission probability, given by

$$T(E_n) \sim \frac{4T_L T_R}{(T_L+T_R)^2}. \tag{2.13}$$

It can be seen from equations 2.11 and 2.13 that when the barriers are identical, such that T_L=T_R, then the peak transmission probability will be equal to unity, i.e. identical barriers give perfect transmission at the centre of the resonant peak. Although on resonance the peak transmission probability depends only on the ratio of T_L to T_R and not their absolute values, equation 2.12 shows that the width of the resonant peak does depend on the individual barrier transmissions and as such the barriers have a significant effect on the resonant behaviour of the system. Figure 2.5 shows the transmission probability for an RTD of width, w=10nm, sandwiched between two 0.3eV high, 5nm wide barriers.

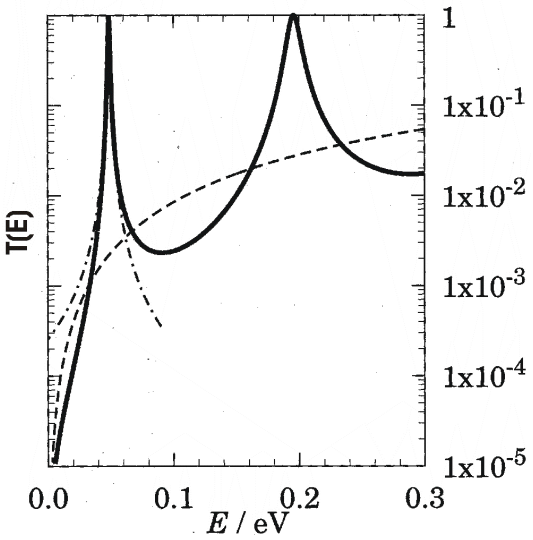

Figure 2.5: Transmission probability for a 10nm wide QW sandwiched by two identical, 5nm wide, 0.3eV high barriers. The solid curve shows $T(E)$ for the whole structure, the dashed curve shows the square of $T(E)$ for a single barrier and the dash-dot curve shows a Lorentzian approximation to the lowest resonance. Figure taken from Davies 1998 [16]. The y-axis is scaled logarthmically.

It can be seen in Figure 2.5 that there are two peaks in *T(*E*)*, corresponding to a resonance for each of the two quasi-bound states. The second resonance is broadened due to the higher transmission probabilities of the individual

barriers caused by the higher carrier energy. The transmission probability shown in Figure 2.5 is for a theoretical case. In a real system there are a number of effects that can cause the actual transmission probability to deviate from this ideal behaviour.

i The energy states in the QW and emitter are broadened due to temperature, impurities and structural fluctuations. In most cases thermal broadening is negligible compared to scattering effects from diffused dopants or barrier material [16].

ii The off-resonance transmission probability of a real device is usually larger than predicted due to carriers tunneling off-resonance. The main contribution to this is from inelastic tunneling via LO phonon emission.

iii The transmission probability does not actually reach unity as the electric field created by an applied bias modifies the second barrier and breaks the symmetry of the system.

iv The electrons remain in the QW for a finite time causing a build-up of charge. This affects the potential barriers, again reducing the symmetry of the system and lessening the resonant transmission probability [56].

v When a bias is applied to the system, the bias drop across the accumulation and depletion regions decreases the effective barrier height, which causes a rapid increase in the transmission probability at higher biases [57].

2.1.4 Coherent versus sequential tunneling

There are two prevalent models used to describe the phenomena of resonant tunneling. In the coherent approach the transmission through the RTD is considered as a single, global variable. The electron wave-function is coherent throughout the structure and phase is conserved. In the sequential approach the process is treated as two successive tunneling events: from the emitter to the QW states and then from the QW state into the collector. Phase is not conserved due to scattering from phonons and impurities in the QW and the process is incoherent.

It has been shown that when the energy distribution of electrons in the emitter exceeds that in the QW, then both approaches give the same value for the current flow through the structure [58]. Indeed it is most probable that in any real device a mixture of the two mechanisms is present. Clearly there must be a coherent component as for the quasi-bound state to exist in the QW an electron must travel at least the length of the QW and back before scattering [59]. Equally the importance of scattering process in RTDs leading to incoherent, sequential tunneling has been shown experimentally [60] and theoretically [61].

Chapter 3

Samples and experimental set-ups

3.1 Introduction

This chapter describes the experimental apparatus and techniques used to conduct the research presented in this thesis as well as providing information about the samples used. Section 3.2 describes all the samples studied in this thesis and is intended as a reference for subsequent chapters.

3.2 Samples

The samples are presented here, indexed with the assignments they will be referred to by in subsequent chapters. All samples are GaAs based p-i-n diodes patterned into circular mesas of between 50 and 400μm in size and contacted

such to allow optical access to the mesa. The wafers are mounted on T05 headers. Sample group A was grown at the Central Facility for III–V Semiconductors in Sheffield by Prof. Mark Hopkinson, all other samples were grown at the University of Nottingham by Prof. Mohamed Henini.

Sample group A

Sample group A consists of a series of symmetrical RTD structures that are identical except for the composition of the intrinsic region. This series of samples was designed to allow a systematic study of the effect of adding quantum dots to a p-i-n RTD structure. The basic growth scheme for these samples is shown in Table 3.1, while the composition of the intrinsic region for the three different samples is shown in Table 3.2. For sample A3 the expected QD density is $\sim 10^{10}\text{cm}^{-2}$, with a diameter of ∼40nm and a height of ∼2nm.

Layer	Thickness(nm)	Material	Growth Temp.	Doping (cm^{-3})
1 (top)	500	GaAs	580°C	p, $1\text{x}10^{18}$
2	5	GaAs	510°C	
3	3	AlAs	510°C	
4	0.6	GaAs	510°C	
i	6	intrinsic region	510°C	
5	0.6	GaAs	510°C	
6	3	AlAs	510°C	
7	5	GaAs	510°C	
8 (buffer)	500	GaAs	580°C	n, $2\text{x}10^{18}$

Table 3.1: Growth layer structure for samples in group A. All samples grown on n^+ GaAs substrate oriented along the (100) axis.

Structure	Content
A1	GaAs
A2	$In_{0.38}Ga_{0.62}As$
A3	2.2ML InAs

Table 3.2: Content of the intrinsic region for the samples in group A

Sample group B

The structures comprising sample group B are all variants on a basic design of QDs situated in a p-i-n diode, see Tables 3.3, 3.4, 3.5 and 3.6. They were designed with the aim of achieving bipolar resonant injection, i.e. injection of both electrons and holes, into the QD states.

Layer	Thickness(nm)	Material	Growth Temp.	Doping (cm^{-3})
1 (buffer)	700	GaAs	600°C	n^+, 4x10^{18}
2	100	GaAs	600°C	n, 4x10^{16}
3	100	GaAs	600°C	
4	2ML	InAs	450°C	
5	60	GaAs	500°C	
6 (top)	500	GaAs	500°C	p^+, 2x10^{18}

Table 3.3: Sample B1, grown on n^+ GaAs substrate oriented along the (311B) axis.

Sample B2

Layer	Thickness(nm)	Material	Growth Temp.	Doping (cm^{-3})
1 (buffer)	120	GaAs	550°C	p^+, 2x10^{18}
2	30	GaAs	550°C	p, 5x10^{17}
3	2.9	AlAs	550°C	
4	2	GaAs	550°C	
5	1.8ML	InAs	500°C	
6	10	GaAs	500°C	
7	2.9	AlAs	500°C	
8	20	GaAs	500°C	
9	50	GaAs	500°C	n, 2x10^{16}
10	80	GaAs	500°C	n, 2e10^{17}
11 (top)	100	GaAs	500°C	n^+, 4x10^{18}

Table 3.4: Sample B2, grown on semi-insulating GaAs substrate oriented along the (100) axis.

Sample B3

Layer	Thickness(nm)	Material	Growth Temp.	Doping (cm^{-3})
1 (buffer)	200	GaAs	550°C	p, $4x10^{18}$
2	50	GaAs	550°C	p, $5x10^{17}$
3	6	GaAs	550°C	
4	1.8ML	InAs	500°C	
5	16	GaAs	500°C	
6	50	GaAs	550°C	n, $2x10^{16}$
7 (top)	500	GaAs	550°C	n, $4x10^{18}$

Table 3.5: Sample B3, grown on p^+ GaAs substrate oriented along the (100) axis. QDs annealed for 85s at 540°C before overgrowth.

Sample B4

Layer	Thickness(nm)	Material	Growth Temp.	Doping (cm^{-3})
1 (buffer)	200	GaAs	550°C	p, $4x10^{18}$
2	50	GaAs	550°C	p, $6x10^{16}$
3	16	GaAs	550°C	
4	1.8ML	InAs	500°C	
5	6	GaAs	500°C	
6	50	GaAs	550°C	n, $1x10^{17}$
7 (top)	500	GaAs	550°C	n, $4x10^{18}$

Table 3.6: Sample B4, grown on p^+ GaAs substrate oriented along the (100) axis. QDs annealed for 85s at 540°C before overgrowth.

Although all group B samples are based upon the same idea of achieving bipolar resonant injection of carriers into QDs, there are some significant differences between them. To enable a quick comparison, a summary of the different structures is shown below. For sample B1 the expected lateral QD size is ∼20nm with a height of ∼2nm. For samples B2-B4, which have a lower QD density, the lateral size and height of the dots is expected to be larger.

Sample	Composition of Active region	QD Density
B1	Undoped GaAs with InAs QDs	10^{11}cm^{-2}
B2	Undoped GaAs, InAs QDs, AlAs tunnel barriers	10^{10}cm^{-2}
B3	Undoped GaAs, InAs QDs, QDs closer to p-side	10^{10}cm^{-2}
B4	Undoped GaAs, InAs QDs, QDs closer to n-side	10^{10}cm^{-2}

Table 3.7: Summary of samples in group B, showing the composition of the active region of the p-i-n diode and QD density.

3.3 Experimental apparatus

3.3.1 Cryogenics

Optical cryostats

For the optical experiments performed in this thesis, two cryogenic systems were used. The first is an Oxford Instruments continuous gas flow cryostat. This consists of an outer vacuum shield acting as a thermal insulator surrounding a sample space. To achieve good thermal isolation from the external environment, the vacuum shield is evacuated using a turbo pump to a pressure of 10^{-6}mbar or lower. The liquid helium coolant is supplied via an external vessel connected directly to the sample space via a transfer line plugged into the cryostat inlet valve. Cooling is achieved by a gas flow pump connected to the sample space. This creates a low level vacuum in the sample space allowing the flow of helium gas from the vessel due to the pressure gradient. Using this method a stable temperature of 3.6K can be maintained. For temperature-dependent experiments a proportional-integral-derivative (PID) temperature control system is used to operate a heater situated in the sample space. This allows a controllable temperature range from 3.6$\pm$0.05K up to 320K.

The second system is an Advanced Research Systems open cycle cryostat. In this system the sample is placed into the main bath of the cryostat, which is then evacuated to $\sim 10^{-6}$mbar. The sample is inserted on a specially designed probe so that it is situated in the homogeneous region of the 1T electromagnet that surrounds the cryostat. The probe is designed to provide cooling by the "cold finger" approach. The mounting block of the probe is copper, providing a good thermal connection between the liquid helium inlet valve and the sample. Final stage heat exchange is achieved through the legs of the T05 sample header. To increase the efficiency of heat exchange a copper holding plate is placed on top of the sample (with a circular hole cut to allow optical access to the sample). To prevent radiative heating of the sample, a copper radiation shield is placed around the lower portion of the probe and then wrapped with aluminium foil, these also have holes inserted to allow optical access to the sample. Helium is supplied from an external vessel via a transfer line. Pressure applied to the vessel from a cylinder of helium gas drives the flow of liquid. The liquid enters the top of the cryostat and cools the sample via the cold finger probe. The flow of liquid is regulated by controlling the pressures at the inlet of the transfer line and exhaust valve of the cryostat. Using this approach a stable temperature of 10 ± 0.2K is achieved, measured via a thermometer attached to the mounting block.

Magneto-cryostat

Magnetic field experiments were undertaken using a Cryogenic gas flow system. The cryostat contains its own liquid helium bath isolated from the external environment by an outer vacuum shield. An inner vacuum shield separates the

sample space from the helium bath. The cryostat contains a superconducting magnet located in the helium bath, surrounding a portion of the sample space. The magnet is capable of generating fields up to 14T within a $1cm^3$ volume enclosing the inserted sample. Situated inside the bore of the magnet is a continuous flow *variable temperature insert (VTI)*. The VTI works by using a vacuum created by an external rotary pump to generate a pressure gradient between the sample space and the helium bath. The flow of liquid helium over this gradient is controlled using a needle value. Correct regulation of this flow across the sample space allows stable temperatures down 1.8±0.02K to be maintained and the temperature can be varied between 1.8K and 300K using a resistive heater located in the heat exchanger adjacent to the sample space. Samples are inserted into the cryostat using specially designed probes to ensure that the sample sits in the central region of the superconducting solenoid, where the magnetic field is homogeneous. Two probe variants were used; the first holds the sample perpendicular to the magnetic field and the second holds the sample parallel to the field and also allows optical access to the sample via an optical fibre link contained within the probe. This can be coupled via a second optical fibre to the optical set-ups.

The use of the optical fibre allows EL measurements inside the magneto-cryostat. Using this technique it has been possible to measure the Zeeman spin splitting of an EL QD peak for sample B1, as shown in Figure 3.1.

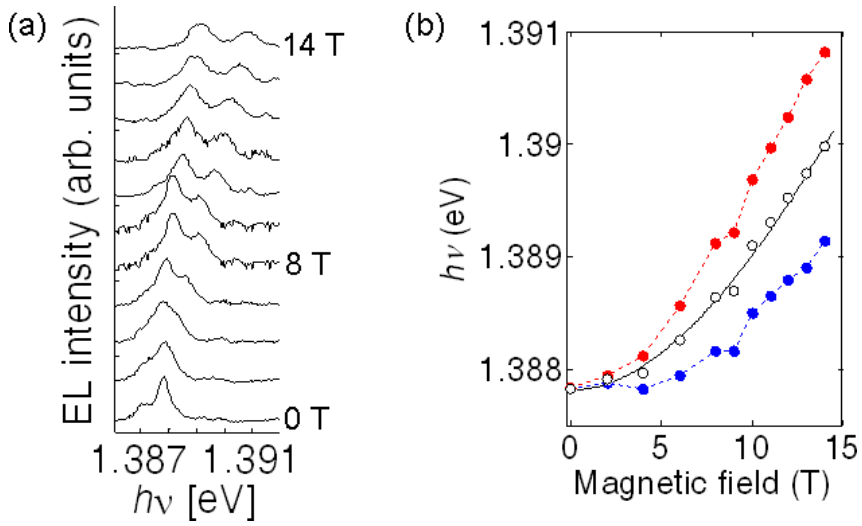

Figure 3.1: (a) EL spectra at different magnetic fields for sample B1 at T=1.8K and V=1.41V showing Zeeman spin splitting. (b) The red and blue lines show the variation in energy of the split peaks with magnetic field and the black line shows the average of the two peak positions.

3.3.2 Electroluminescence measurements

Optics

For the EL spectroscopy measurements two optical set-ups, equipped with different light detectors, were used. Collection of light from the sample is done in similar ways for both systems. As shown in Figure 3.2 a lens is placed close to the optical window of the cryostat. This lens collects light from the sample and turns it into a collimated beam. A second lens (typically with a f-number f/4) is then positioned in the beam path to focus it into the entrance slit of a spectrometer. Correct alignment of the sample, or optical fibre, and lenses with the spectrometer entrance slit is of paramount importance to ensure good signal pickup.

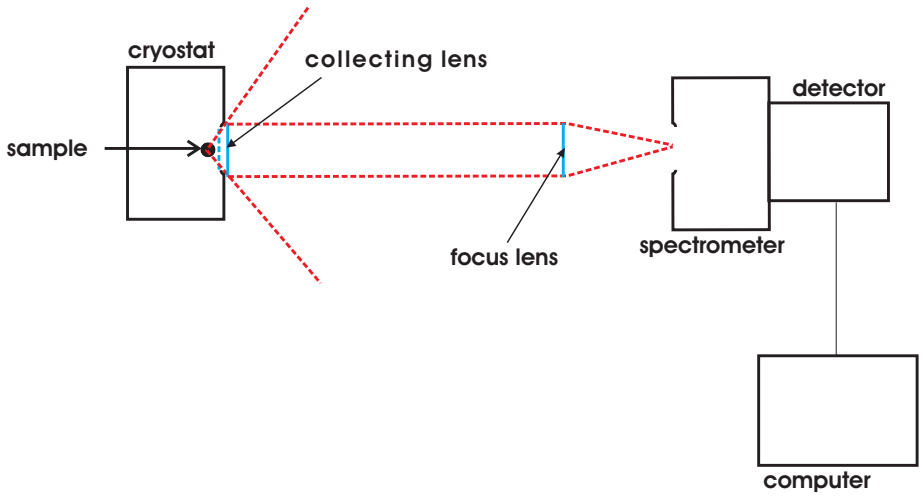

Figure 3.2: Schematic diagram of optical experimental set-up. The dashed red lines indicated light rays. When an optical fibre is used this is positioned in place of the sample.

Electroluminescence experiments using the first cryostat discussed in section 3.3.1 and the magnetocryostat are both processed using a Triax 550 series spectrometer (system 1). This is a double pass system with a focal length of 0.55 meters. The light entering the spectrometer shines onto a collimating mirror and is sent to a grating with 1200 grooves/mm. This separates the incoming signal into its constituent wavelengths and reflects the dispersed beam onto a focussing mirror. Finally, light is reflected towards a silicon CCD detector or by an optional swing mirror to an InGaAs photodiode. The limiting factor for spectral resolution is the beam dispersion by the grating. The dispersion is 1.55 nm/mm, giving a spectral resolution of 3.8meV with a slit width of 2mm and a wavelength of 1μm.

Control of, and signal output from, the spectrometer/detector system is fully automated and controlled via computer. It is possible to display the measured signal onto the computer display in real time to aid with the alignment of the optics. Optimum alignment is achieved when the incoming beam is focussed

on the optical axis defined by the center of the entrance slit and the center of the collimating mirror.

Electroluminescence experiments using the second cryostat discussed in section 3.3.1 are processed using a SPEX 1702 spectrometer (system 2), which has a focal length of 0.75m and a dispersion grating with 600 grooves/mm. This gives the system a typical dispersion of 18.6$\mathring{A}$/mm so that with a standard 2mm slit width, the energy resolution is 3.4meV at a wavelength of 1μm.

During the measurements, the balance between the signal intensity and resolution was always considered. Closing the slit width to 0.5mm gives a resolution of ∼1meV, but at the cost of reducing the signal intensity by 75% compared to a 2mm slit width. Where the need for high resolution was paramount, the slit width was chosen appropriately, at all other times a width of 2mm was used as a balance between resolution and intensity.

Detectors

After passing through a spectrometer and being dispersed into its constituent wavelengths, the signal passes out of the exit slit and into an attached detector, where its strength at each wavelength is measured and the data processed by a computer. The detector associated with system 1 is a liquid nitrogen cooled, Si Charge Coupled Device (CCD). The CCD is a detector array with a two-dimensional matrix of pixels to detect an incoming signal. When a photon enters the CCD it will usually (typical quantum efficiency is 70%-80%) excite an electron across the intrinsic band gap of the semiconductor material the CCD is based on. The detector is capable of integration times of between 1μs and hours, though for integration times in excess of 30 seconds the in-built

cosmic ray removal function must be used to obtain clear data. In order to obtain a good signal to noise ratio, the integration time was chosen so that the signal strength was close to the detector saturation threshold. The Si CCD is effective at detecting photons with wavelengths between 400nm and 1100nm. The efficiency profile for this device varies continuously across its range, increasing in a stepped fashion from 0.3 at 400nm to 1 at 950nm. For λ>950nm, the detector efficiency drops off so that it is 0.2 at 1100nm.

Although the Si-CCD is the most efficient detector for many measurements, it has the disadvantage that its efficiency profile has a sharp gradient for λ>950nm. For some of the experiments presented in this thesis, this can have a noticeable effect on the measured spectra. In order to take into consideration this effect, an efficiency correction algorithm was developed. The accuracy of this algorithm is demonstrated in Figure 3.3, which shows two spectra taken using the different detectors connected to system 1. The red curves are from the Si CCD and the blue from an InGaAs diode. Figure 3.3(a) shows the spectra before the correction algorithm was applied, and it can clearly be seen that there are significant differences between the spectra. In Figure 3.3(b), after the correction algorithms have been applied, the agreement between the spectra is significantly improved with the remaining differences explainable by the fact that there are some inherent differences between the two detectors. The EL data presented on sample A2 in Chapter 4 uses this correction method. In all other cases it was not deemed necessary to alter the original data.

System 2 uses a liquid nitrogen cooled InGaAs array detector. The pixel array is a single line containing 512 pixels. The detector is capable of integration times from 1μs to 10 minutes. The InGaAs detector has as essentially flat

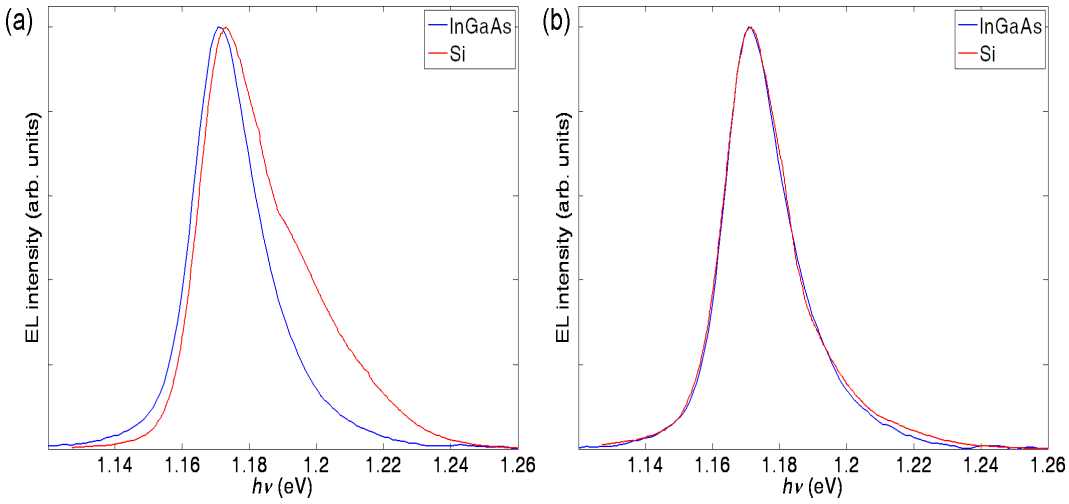

Figure 3.3: EL spectra of a p-i-n diode incorporating an InGaAs QW taken with two different detectors. (a) shows the spectra before the correction algorithm is applied and (b) shows the corrected spectra. The Si CCD data is shown in red and the InGaAs diode in blue. The data have been normalised to a maximum height of 1.

efficiency profile across the QD band between 950nm and 1600nm, but at either end there is a sharp tail-off in its efficiency.

3.3.3 Micro-electroluminescence measurements

Some of the measurements performed for this thesis were in collaboration with Erik Stock at the Institute of Solid State Physics of the Technical University Berlin. The equipment there enabled micro-EL measurements to be carried out. In these experiments the light from a specific point on the sample mesa can be measured.

The cryostat is a cold-finger system with cooling achieved by pumping liquid helium from an external vessel. The whole system, excluding the vessel, is installed on a vibration isolation table. The temperature reading at the sample suggests that a temperature of 15K is achieved, though measurement of the

GaAs emission line indicates that the carriers are actually at a temperature of 30K. The sample is positioned very close to the optical window of the cryostat, so that radiative heating is probably responsible for the relatively high temperature of the liquid helium system. The closeness of the sample to the window allows for the efficient extraction of the signal needed for the experiments performed in this set-up. A beam line is set up between the cryostat and a series of 3 spectrometers. The beam line allows for mirrors and lenses to be readily interchange on mounts fixed at pre-installed positions. An additional feature of this set-up is that it allows for a Silicon CCD webcam to be fixed into the mount close to the optical window in order to take an optimal image of the mesa.

For the micro-EL measurements a moveable mirror is placed in the beam line. A specially developed *Labview* program is used to run the experiments. This enables the mirror position to be changed to extract light from specific positions on the mesa. Correlation of the sample and mirror position allows the program to accurately calculate where on the sample the measured signal is coming from. In standard micro-EL experiments, a bias is applied and a pre-determined frequency range is selected to be measured. At every interval in this range the mirror is scanned across the sample, or an area of the sample, in a grid pattern to build up an image of how the light emission at that specific frequency varies across the sample. The resolution of this technique is $\sim$0.15meV.

3.4 Current-voltage measurements

Measurement of the current-voltage ($I(V)$) characteristics of the samples forms an important part of the research presented in this thesis. The basic measurement circuit used to perform $I(V)$ measurements consisted of a Keithley 2400 digital multi-meter performing as both a voltage source and current measurement device, with a 0.1Ω grounding cap used to complete the circuit. The typical low-temperature resistance of the sample was of the order of 10kΩ so the resistance of the cables used in the measurement circuit, typically 10Ω, has been neglected. The $I(V)$ experiments performed in this thesis were automated using a *Labview* program written specifically for the task. This allowed automated control of the output voltage signal and the reading in, and storing of, the returned current data. The automation extends to control of the magnetic field so that $I(V)$ measurements over a range of magnetic fields could be taken efficiently.

3.4.1 High sensitivity measurements

The current sensitivity of a Keithley 2400 is ∼100pA. For some of the experiments performed in this thesis a higher degree of sensitivity was needed in order to be able to measure the lower currents produced by the samples. For this purpose a custom current-to-voltage converter was made which could be used in conjunction with an Aglilent 34420A digital volt meter to enable measurements with sub-pA accuracy. A schematic circuit diagram of the current-to-voltage converter is shown in Figure 3.4.

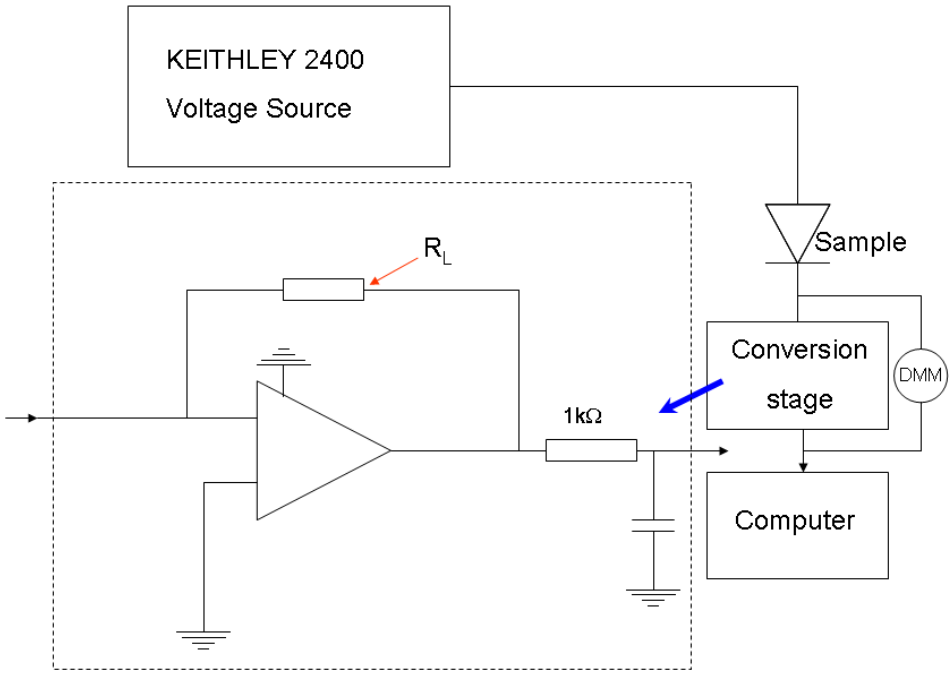

Figure 3.4: Schematic diagram of the current-to-voltage converter, and its associated circuit, used for high sensitivity experiments. *DMM* is the digital multi-meter used to measure the output voltage from the converter.

The current-to-voltage converter is based on the "ideal" design reported in ref [62] and uses an operational amplifier (op-amp) in series with a load resistor to convert the output signal from the sample from Amps to Volts. The sample output is fed into the negative input of the op-amp. The positive terminal is grounded, meaning that the negative terminal must also be at ground potential, making it a *virtual ground*. The output from the op-amp is in series with a load resistor, R_L, see Figure 3.4. The current coming from this resistor must balance the current passing into the negative input terminal of the op-amp so the output voltage of the op-amp must be $V_{out} = I_{in}R_L$. This allows R_L to be chosen such that it will boost the output signal of the sample to the level required for the measurement. The 1kΩ resistor also connected in series with the output voltage is included to prevent a short-circuit damaging the op-amp.

This has a negligible effect on the circuit operation as R_L is 4-6 orders of magnitude larger in the current-to-voltage converter used for the experiments in this thesis.

3.4.2 Noise reduction

In order the perform the low current ($\sim$pA) measurements, precautions have to be taken to ensure that noise generated by the measurement circuit does not generate anomalous data spikes or mask the real signal . In our experiments the main sources of noise were the digital electronics and power sources inside the voltage source, measurement device and current-to-voltage converter. The walls of the cryostat act to screen the sample from this noise, but it is still possible for it to be picked-up through the cables. To minimise this effect screened co-axial cables with bnc connectors were used and the equipment was laid out to ensure that there was as much clearance as possible between the cables and equipment. Movement of the cables due to vibrations, or where they are exposed to magnetic fields, can generate noise in a number of ways, with spikes due to capacitive and resistive changes, piezo-electric noise generated by changes in stress of the cable insulation [63], and movement at the electrical contacts changing the coupling efficiency being the biggest sources. Securing the cables to a rigid surface was found to reduce these effects to an acceptable level and had the additional advantage that the cables could be secured in such a way as to minimise their exposure to the magnetic field. The measurement circuit was designed to have only one earth connection in order to prevent a ground loop. For measurements performed at 4.2K, in free standing He storage vessels of liquid helium, the vessel was placed away from external sources of

vibration and wedged in place to stop any movement of the wheels on the vessel.

All magnetic measurements were performed in the magnetocryostat discussed in section 3.3.1. In this system care had to be taken to reduce vibrations from external sources, such as the pump used in the cooling of the cryostat, as much as possible. Additionally, when performing $I(V)$ measurements, the power to the thermometer in the sample space had to be disconnected as this proved to be a significant source of noise. When this was the case, the temperature was monitored via the pressure of the helium flow through the sample space and by using the thermometer to check the temperature between measurements.

For all measurements a time delay of 60 seconds from applying the initial voltage to beginning the current measurement was introduced by the controlling software. This was in order to give the capacitances present in the system time to fully charge. After this, a delay of no less than 300 ms, between applying a new voltage and beginning the measurement, was used to give the circuit time to settle after each change. At least 4 measurements of each current were taken and then averaged to generate the stored value. For more sensitive measurements, up to 10 values were taken and used to generate the average.

Chapter 4

P-I-N diodes incorporating quantum dots and quantum wells

4.1 Introduction

In order to investigate the injection of carriers into an ensemble of QDs, a series of samples were grown (see Sample group A in section 3.2). Samples A1, A2 and A3 are all based on the same RTD structure, but contain in their intrinsic region a GaAs QW, an $In_{0.38}Ga_{0.62}As$ QW and a single layer of InAs QDs, respectively. The central regions of the conduction and valence band energy profiles at T=300K for samples A1, A2 and A3 are shown in Figures 4.1, 4.2 and 4.3, respectively. The band diagrams are calculated using the software package BandEng by M. Grundmann [64].

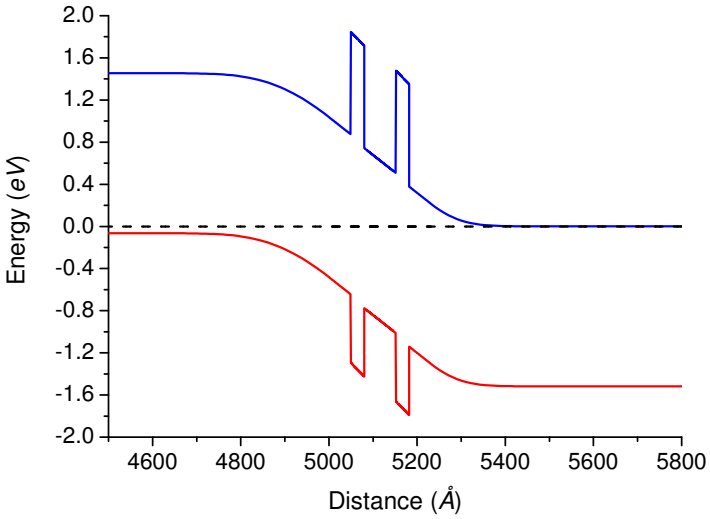

Figure 4.1: Band diagram at 300K with no applied bias for sample A1. The Fermi level is indicated by the dashed, black line.

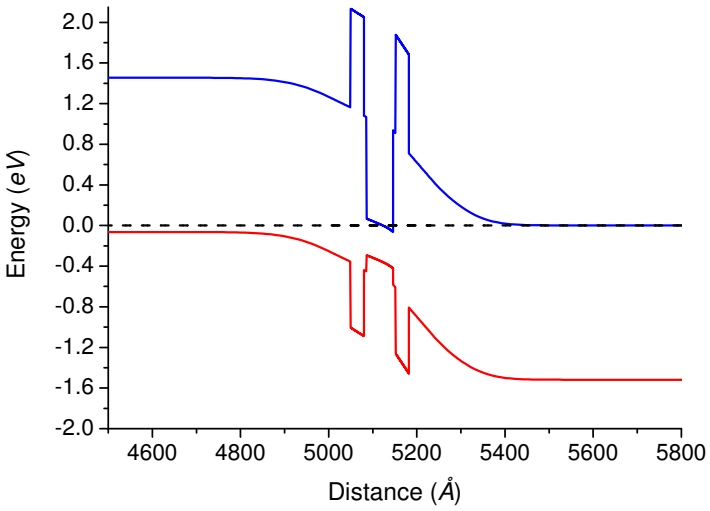

Figure 4.2: Band diagram at 300K with no applied bias for sample A2. The Fermi level is indicated by the dashed, black line.

As can be seen in Figures 4.2 and 4.3, the QW and QDs in samples A2 and A3, respectively, can create lower-dimensional energy states below (above) the GaAs conduction (valence) band edge.

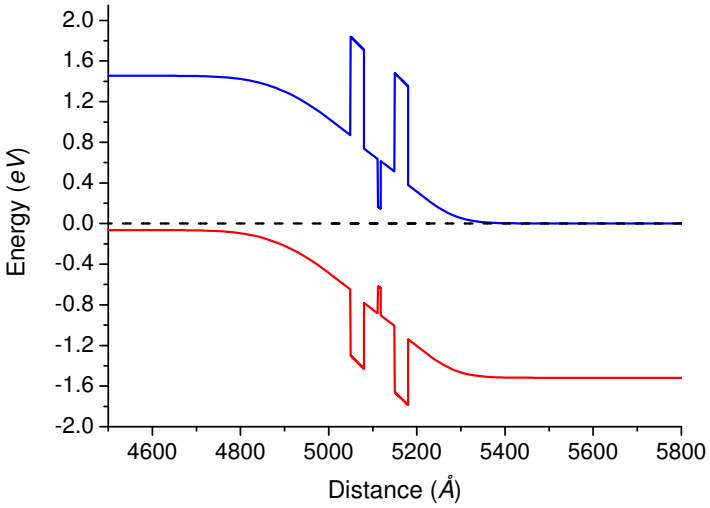

Figure 4.3: Band diagram at 300K with no applied bias for sample A3. The Fermi level is indicated by the dashed, black line.

In order to begin to understand sample A2 a program based on a simple, numerically solved model for a 1D square well of finite depth [16] has been developed to estimate the energies of the confined states in the InGaAs QW. The material parameters used in this model are given in Appendix B. Although the model is a textbook case, including the modification to take into account the different effective masses across the structure, there are still some points that merit discussion.

i The model has only been constructed to look at the QW in the intrinsic region of the structure. The QW formed by the AlAs barriers has not been modeled. This does not affect the model too adversely as the energy states of interest lie well below those created by the AlAs barrier so should not be significantly modified by them.

ii An idealised case of a square well is used. This means that all carriers are assumed to have k=0. Whilst this does compromise the accuracy of the model, this approach is still valid for the approximate energy levels it is intended to produce.

iii The effects of strain on the InGaAs crystal lattice are included. The strain acts to increase the InGaAs band-gap and to break the degeneracy of the valence band at the Γ-point.

iv Light and heavy holes are accounted for, but the split-off band is ignored as it does not feature prominently in the carrier dynamics, due to the relatively large spin-orbit splitting of the valence band.

v The exciton binding energy has been ignored as this is typically much smaller than the single carrier confinement energy.

vi Although the InGaAs QW in sample A2 was grown with a nominal indium concentration of 38%, a concentration of 24% was used in the model in order to accurately describe the transport data. This is a reasonable alteration to make as it has been shown that indium segregates greatly in semiconductor QW structures [65], so the concentration in the centre of the QW will almost certainly be lower than 38%.

Table 4.1 shows the calculated energy levels generated by this model for the InGaAs QW. The energies are given relative to the bottom (top) of the InGaAs QW for the electrons (holes). The model indicates that there are a number of confined energy levels present in the QW, with each offering a state that is available to carriers for resonant tunneling. Calculations indicate that there

are two electron, two light hole and three heavy hole levels bound inside the well.

Energy (eV)	Level
-0.1322	lh1
-0.1014	hh3
-0.0471	hh2
-0.0173	hh1
0.0745	e1
0.2584	e2

Table 4.1: Calculated energy levels at zero bias for the InGaAs QW. Energies are given relative to the bottom (top) of the conduction (valence) band QW. *e, lh* and *hh* denote electron, light hole and heavy holes states, respectively.

4.2 Current-voltage characteristics

Figure 4.4 shows $I(V)$ plots of samples A1, A2 and A3. The curves are taken using a measurement device which is not sensitive enough to accurately detect currents lower than 100pA. However, this does mean that in the presented data all three structures have a common background current level, which is useful for an initial comparison of the broad scale differences between them.

It can clearly be seen that there are significant differences in the $I(V)$ characteristics of the three structures. Sample A1 does not show any current below V=1.41V. A small shoulder appears in the $I(V)$ before the larger, exponential increase at V=1.51V, corresponding to the GaAs flat-band condition (V_{fb}). Given that sample A1 is a GaAs p-i-n diode, the presence of a noticeable current at $V<V_{fb}$ is probably due to transitions through impurity states associated with donors and acceptors in GaAs. In structure A2 a measurable current begins to flow at a much lower voltage, $V\sim$1.00V, which fits well with

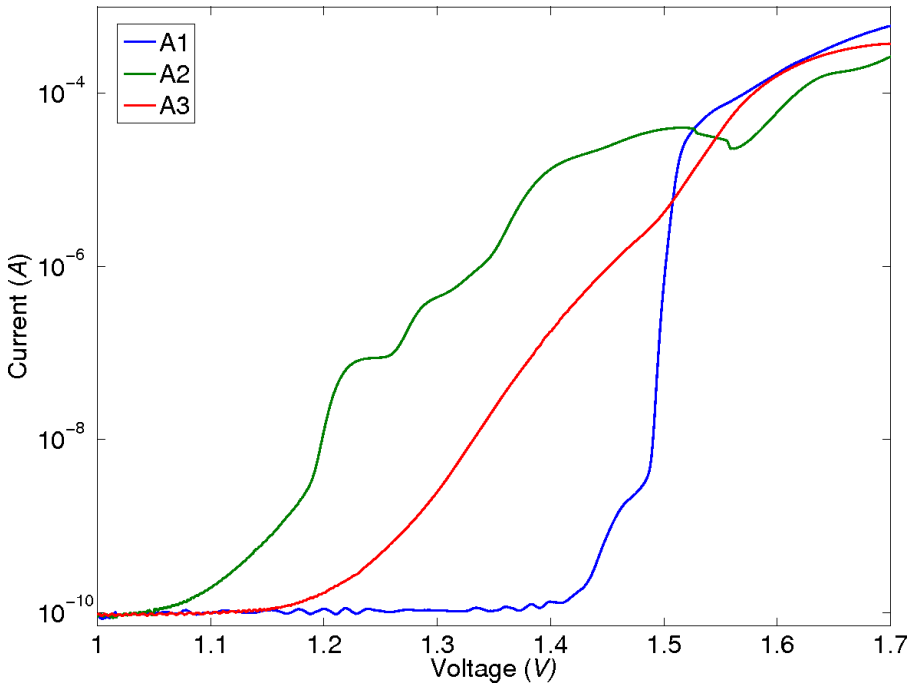

Figure 4.4: $I(V)$ curves at 4.2K for sample A1 (blue), A2 (green) and A3 (red). The noise level in the experiment was ∼100pA.

the presence of low energy QW states as discussed in section 4.1. After an initial increase a number of well resolved current peaks are observed at voltages below V_{fb}, which are associated with electrons and holes tunneling into the bound QW states. The point at which sample A3 passes a measurable current lies in between that of A1 and A2. The current initially begins to flow at V∼1.18V and there is a noticeable shoulder in the $I(V)$ between V∼1.30V and V∼1.49V. The resonant features of the $I(V)$ above V_{fb} are different from those in samples A1 and A2 but, given the presence of InAs as opposed to GaAs or InGaAs in the structure, this is to be expected.

The data presented in Figure 4.4 are useful for comparing the three different structures and for revealing major differences between them. However, given the limited sensitivity of the measurement device used in the comparative

study, additional, high sensitivity measurements were made on each sample. These will be discussed later.

In order to understand the $I(V)$ curve for sample A2, the energy levels presented in Table 4.1 need to be recalculated in terms of the applied bias required to bring the relevant Fermi energy in the GaAs emitter layers into resonance with a given bound state of the InGaAs QW. The recalculation also takes into account the leverage factor. The leverage factor is defined as the ratio of the voltage drop across the whole device to the voltage taken to raise the relevant carrier Fermi level into resonance with the QW level. In a symmetrical structure with a uniform electric field, such as that shown in Figure 4.5, the leverage factor is determined by $f=\frac{L}{D}$.

In the sketch of Figure 4.5 L and D are the relevant distances for calculating the leverage factor, E_{Fe} and E_{Fh} are the electron and hole Fermi energies, respectively, e_n and h_n denote bound electron and hole QW states, respectively and eV is the energy supplied by the applied bias. Additionally Eg_{GaAs} and Eg_{InGaAs} denote the GaAs and InGaAs band-gaps, and E_{QWe} and E_{QWh} are the energies to the bottom of the conduction and valence band QWs, respectively. The values of e_n and h_n are given in Table 4.1.

Equations 4.1 and 4.2 give the relations used for the electron and hole calculations, respectively. The resonant energy is determined by the bias, V_n, required to bring the electron or hole energy level, e_n or h_n, respectively, into resonance with the relevant Fermi energy.

$$eV_n = E_{Fe} + E_{Fh} + Eg_{GaAs} - \frac{L}{D}E_{QWe} + \frac{L}{D}e_n \tag{4.1}$$

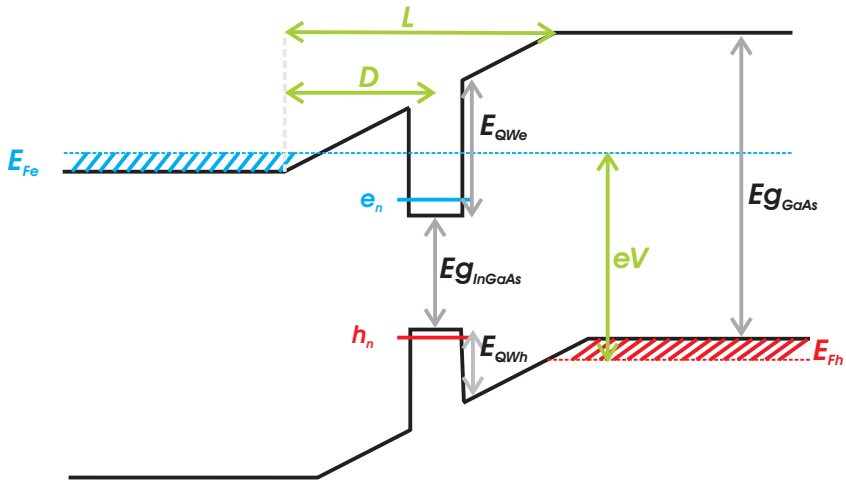

Figure 4.5: Schematic diagram illustrating the model for the resonant energy estimates presented in table 4.2 and the leverage factor.

$$eV_n = Eg_{GaAs} + E_{Fe} - \frac{D}{L-D}E_{Fh} - \frac{E_{QWh} - h_n}{1 - \frac{D}{L}} \tag{4.2}$$

Table 4.2 shows the theoretically calculated resonant energies, as determined by equations 4.1 and 4.2, alongside the experimental values and carrier designation.

Experiment (eV)	Theory (eV)	Level
1.21	1.160	e1
1.28	1.290	hh1
1.38	1.350	hh2
1.45	1.467	hh3
1.53	1.528	e2
1.53	1.529	lh1

Table 4.2: Resonant energy levels of QW levels in sample A2. *e*, *lh* and *hh* denote electron, light hole and heavy holes states respectively.

In general, the calculated resonances in table 4.2 show good agreement with the experimental values, especially considering the limits of the model used. The experimental values for the energy levels in table 4.2 are taken at the

inflection points of the $I(V)$ curve. The inflection points appear as peaks in the scaled derivative of the $I(V)$ curve shown in the inset of Figure 4.6.

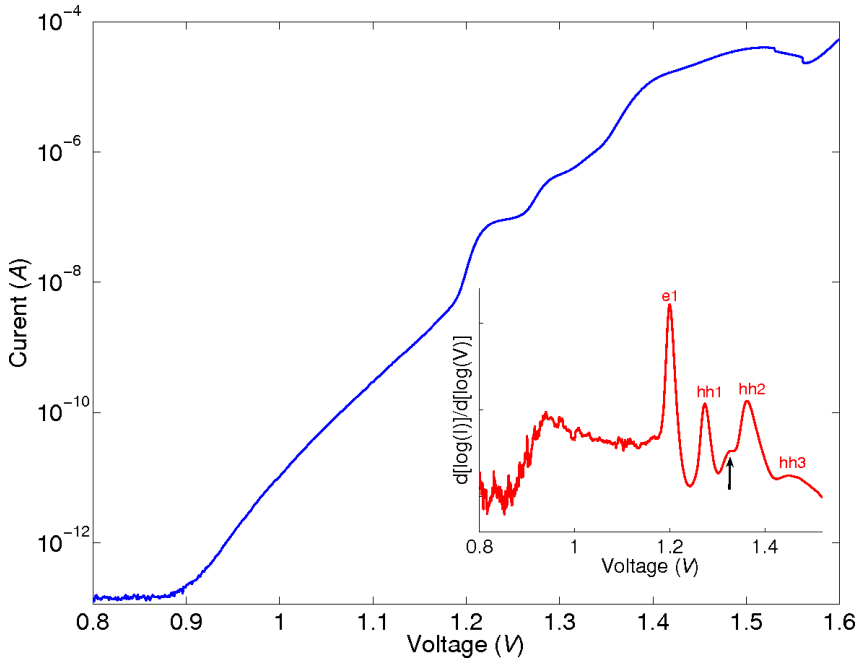

Figure 4.6: High sensitivity $I(V)$ curve at T=4.2K for sample A2. The inset shows the logarithmic derivative, $\frac{d[log(I)]}{d[log(V)]}$. The peak indicated by the black arrow is discussed in the text.

The initial, broad shoulder which produces a local, but indistinct, maxima at V=0.95V does not match well with any of the theoretical energy levels in Table 4.2. However, given that it does not show the usual characteristic features of a QW resonance, it seems reasonable to attribute this initial current increase to states below the QW, possibly caused by segregated indium. The energy levels shown in table 4.2 all produce strong, clear peaks in both the $I(V)$ and logarithmic derivative of the $I(V)$ in Figure 4.6, and can all be matched well with the theoretically calculated energy values. However, there is an additional, smaller and less well defined peak at V=1.33V, indicated by the black arrow in the inset of the figure. This does not correspond to any of the theoretical predictions and at present no explanation is offered for its presence.

The level at V=1.53V is attributed to both the *e2* and *lh1* states in table 4.2. This is because the theoretical energy values for both of these levels fall close to the experimentally measured peak in the $I(V)$ and, given the basic nature of the model, it could well be that these states fall close enough in energy that they overlap. This energy level also does not produce a resonance in the same way as the other levels, instead being marked by a sharp drop in the current. Considering the theoretical prediction of its energy, this is probably because, by the time the applied bias is sufficient to bring it into resonance, the contributions from the bulk GaAs and possibly even the AlAs/GaAs QW serve to mask and alter the resonance it would cause in the $I(V)$.

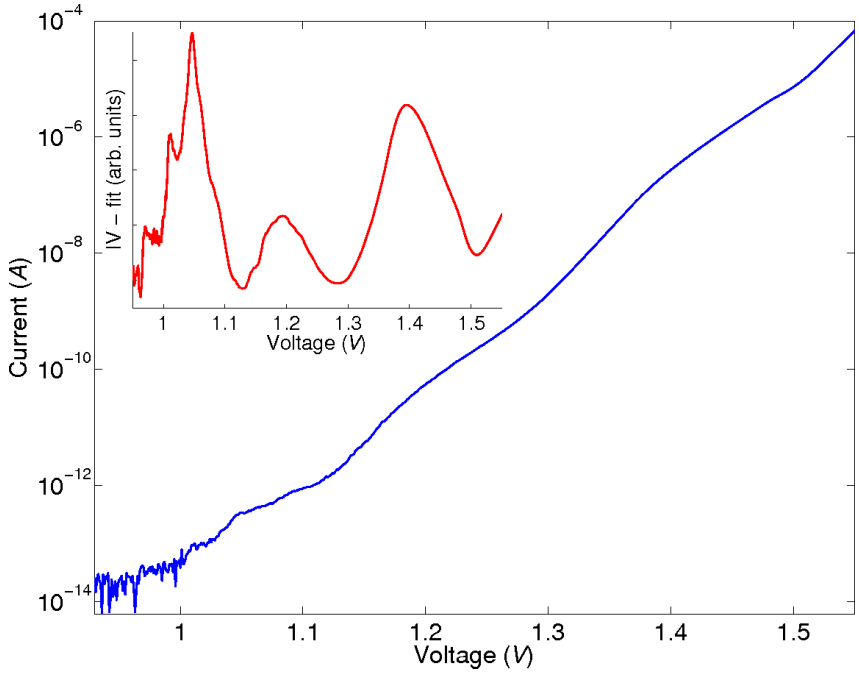

Figure 4.7: 1.8K high sensitivity $I(V)$ curve for sample A3. The inset shows the same $I(V)$ data with an fitted exponential, I_f=$Ae^{\beta V}$, subtracted. The data is then scaled by the current of the fitted $I(V)$.

The sub pico-Amp measurements on sample A3, shown in Figure 4.7, reveal interesting features. It can clearly be seen that current starts to flow at V∼1.00V

and that there are two additional shoulders to the one revealed in Figure 4.4. The inset in Figure 4.7 shows the same $I(V)$ curve, but with an exponential approximation to the $I(V)$ subtracted. Three regions of increased current flow below V_{fb}, centered at $V \sim$1.05V, 1.19V and 1.39V, are clearly visible. The fact that these regions of increased current flow are present in sample A3 and not sample A1 indicate that there are additional available states for the carriers to tunnel into in sample A3. AFM images on samples similar to A3 have shown that the InAs forms QDs in the GaAs matrix and as such it is reasonable to conclude that it is the QDs that provide the additional available states for electronic conduction. However, whilst the $I(V)$ characteristic provides a clear indication of the presence of QDs in sample A3, it does not provide information on the nature of the three shoulders, nor does it indicate whether or not the carriers are injected resonantly into the dots.

4.3 Electroluminescence measurements

Figures 4.8 and 4.9 show the EL and colour-scale data for sample A1 at T=3.6K, respectively.

It can be seen in Figure 4.9 that at higher biases, V>1.60V, a strong emission band emerges at $h\nu$=1.55eV due to the AlAs/GaAs QW present in the structure. Below this bias the main emission line is due to electron-hole recombination from the GaAs layers surrounding the AlAs/GaAs QW. This is due to recombination of electrons and holes at neutral electron-acceptors (eA^0). A weak contribution from the GaAs free-exciton (FE) can be seen at the highest applied biases (V>1.6V). The EL from sample A1 dies very quickly for

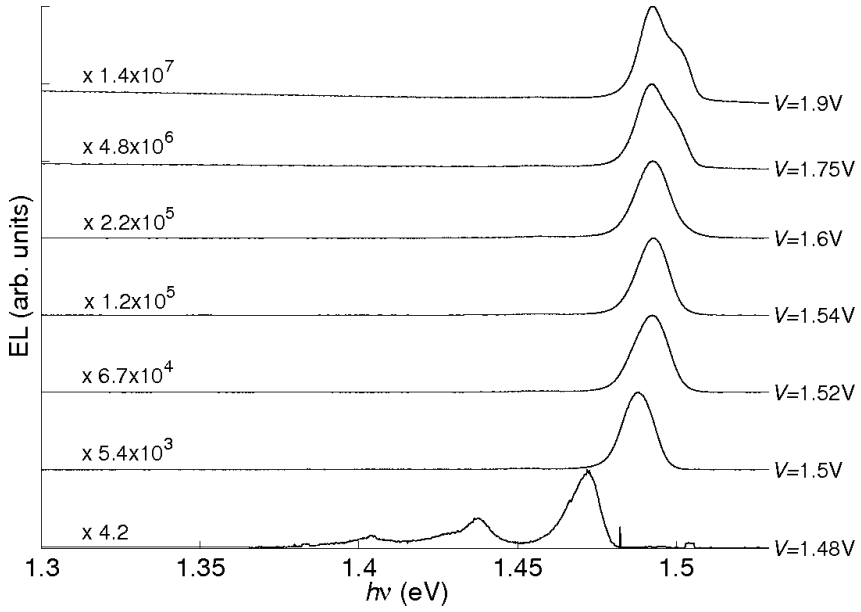

Figure 4.8: EL spectra of sample A1 at T=3.6K. The curves have been normalized to the maximum peak height and offset for clarity. The normalization factors, e.g. x5.4x10^3, are included on the left.

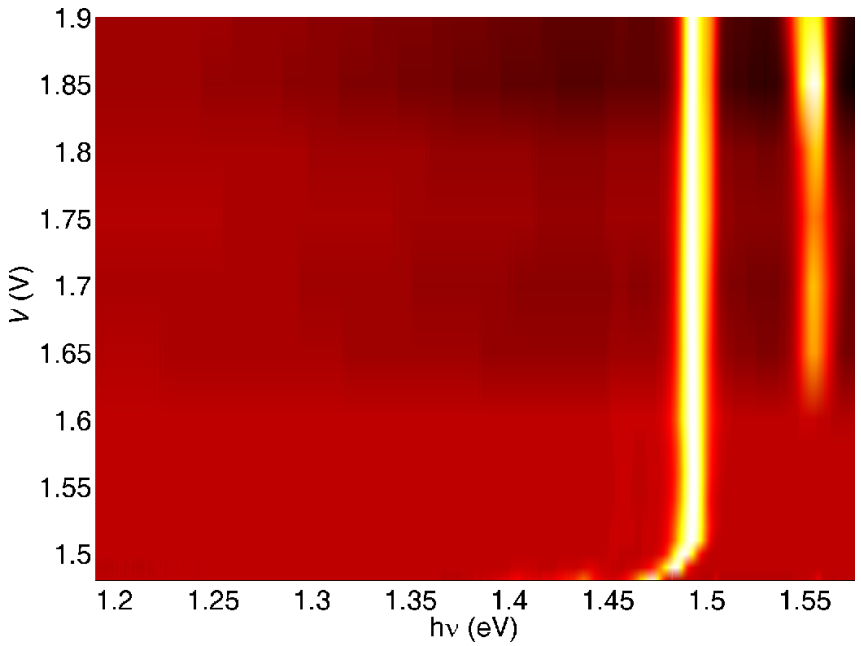

Figure 4.9: Colour-scale plot of the EL intensity vs V and emitted photon energy ($h\nu$) for sample A1 at T=3.6K.

V<1.52V. Note that the current flowing through the device also decreased rapidly for V<1.52V. However, before the emission dies out, a slight energy shift of the GaAs emission line can be seen. This is due to carrier recombination from deeper acceptor states becoming the dominant process as, for V<1.5V, carriers no long have enough energy to form GaAs excitons [66]. In Figure 4.8, at V=1.48V, two low energy peaks appear in the EL due to phonon replicas of the primary emission peak. These replicas are present at higher biases too; however, they can only been seen by using logarithmic scaling on the y-axis as their intensity is much lower than the main emission peak.

Figures 4.10 and 4.11 show the EL spectra and colour-scale image, respectively, for sample A2. At high bias the EL of sample A2 is dominated by the emission peak at V∼1.174V due to electron-hole recombination from the InGaAs/GaAs QW. An additional emission is observed at $h\nu$=1.49eV and is attributed to the GaAs eA^0 recombination. Weaker emission peaks can be seen in Figure 4.10 at $h\nu$∼1.19eV and 1.20eV.

Table 4.3 shows the theoretical energies for electron-hole recombination from the energy levels in the InGaAs/GaAs QW. Only those types of recombination that have energies in the range of the observed emission are shown.

Energy (eV)	Recombination
1.175	e1-hh1
1.205	e1-hh2
1.290	e1-lh1
1.386	e2-hh2

Table 4.3: Recombination energies for sample A2. Energies given are a summation of the electron and hole confinement energies given in Table 4.1 plus the InGaAs band-gap. *e, lh* and *hh* denote electron, light hole and heavy holes states, respectively.

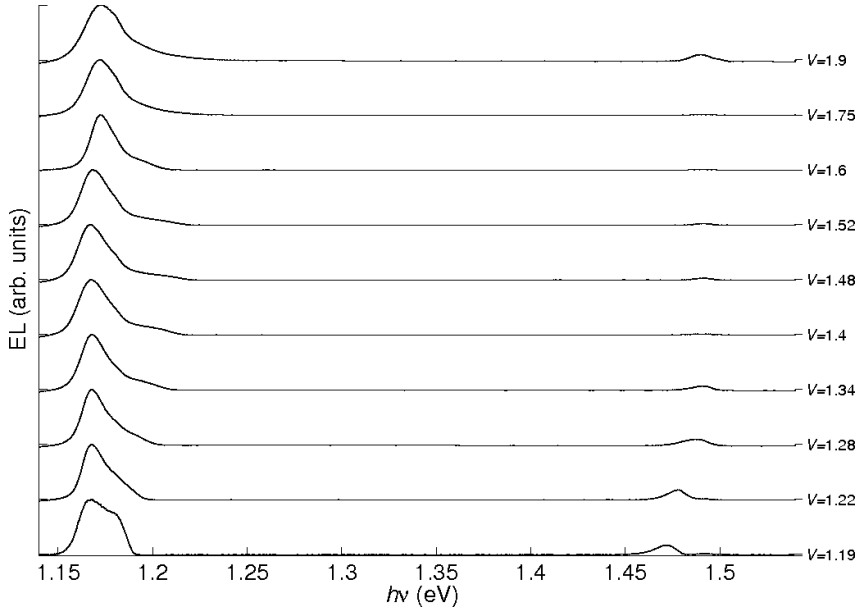

Figure 4.10: EL spectra of sample A2 at T=3.6K. The curves have been normalized to the maximum peak height and offset for clarity.

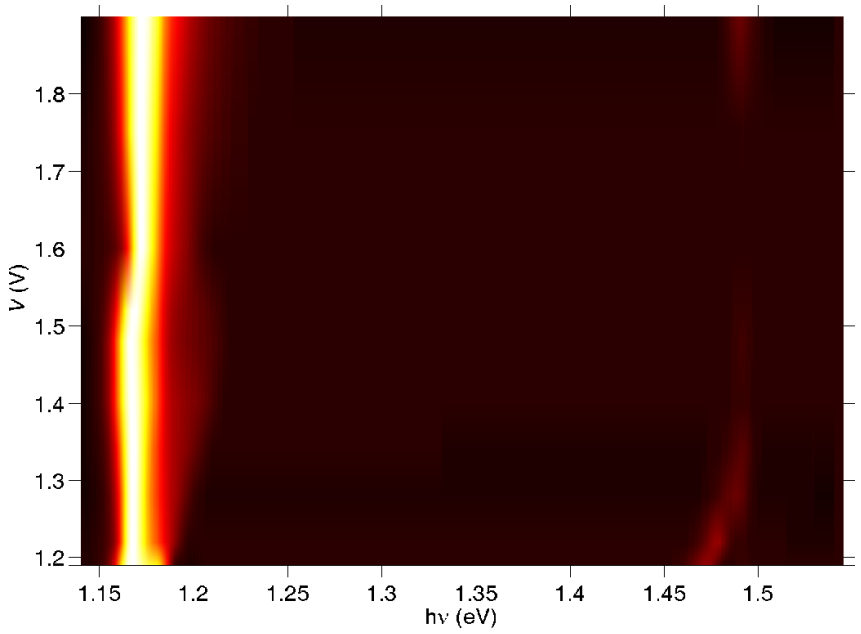

Figure 4.11: Colour-scale plot of the EL intensity vs V and emitted photon energy ($h\nu$) for sample A2 at T=3.6K.

Looking at the calculated energy levels for the QW in sample A2, given in Table 4.3, it seems likely that the strongest emission peak corresponds to recombi-

nation of carriers from the *e1* and *hh1* levels, which is the lowest calculated energy transition. The separation between the *hh1* and *lh1* is significant due to the strained nature of the lattice. This means that any transition between *e1* and *lh1* would be distinct and observable. As this is not present, even at higher biases, it indicates that the holes are able to relax into the lowest available energy state before recombining. The additional emission peak at V=1.19eV does not correspond to any calculated transition, and while the peak at V=1.20eV does fit well with the *e1-hh2* transition, this is a forbidden transition so unlikely to be the cause. Considering this evidence, these emission peaks are attributed to recombination of carriers in localised areas of lower than average indium concentration. This means that these carriers would experience a larger band gap, which would be a much more significant effect than the change to their effective masses, and they would thus emit a higher energy photon upon recombination.

The much larger relative intensity of the QW emission, compared to that of the GaAs, is due to the relaxation time for carriers to go from the GaAs states into the QW being much smaller than the exciton recombination time in GaAs [67]. Reducing the applied bias causes a reduction in the relative intensity of the GaAs emission line and also leads to a narrowing of the QW emission. As the bias is reduced below $V\sim$1.60V, the main QW emission line shifts from $h\nu\sim$1.174eV to $\sim$1.168eV. A possible explanation for this is that if there are fluctuations in the potential profile of the QW, for example due to locally high and/or low concentrations of indium, this will create areas of higher confinement energy, but lower potential, for the carriers. At high biases these fluctuation will be filled and the majority of the carriers will recombine from the recognised QW level. However, at lower biases this will

not be the case and an increasingly significant proportion of recombinations will involve carriers in these fluctuations, which will influence the observed EL. At the lowest applied bias the emission peak at $V \sim 1.20$V becomes relatively more intense, suggesting the possibility of resonant injection. Unfortunately, the emission intensity was not sufficient to investigate this by going to lower applied bias.

Figures 4.12 and 4.13 show the EL spectra and colour-scale image, respectively, for sample A3. Note that the bias dependance of these spectra differ significantly from that of samples A1 and A2. Above $V = 1.58$V, the emission from sample A3 is dominated by the GaAs line (not shown), though there is also a weaker, broad emission characteristic of a QD ensemble [68].

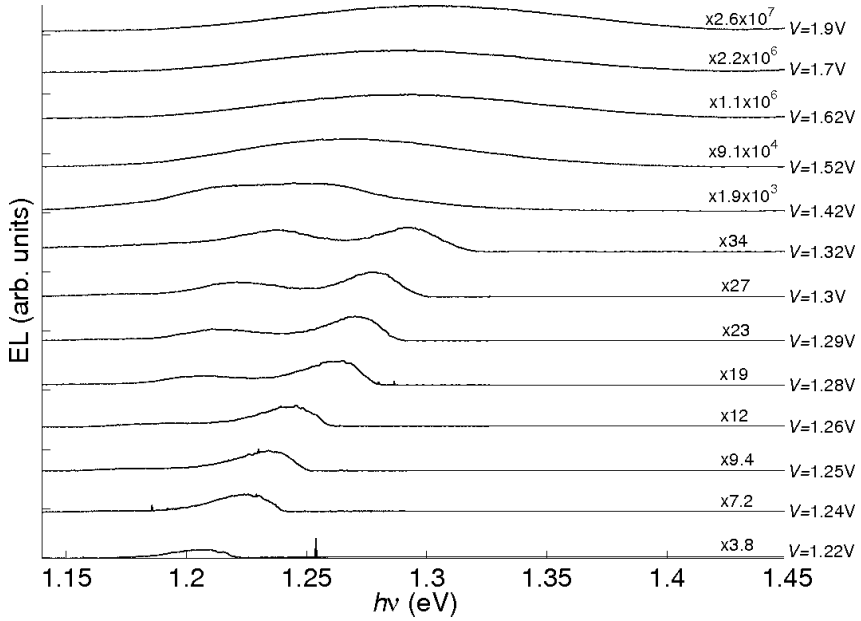

Figure 4.12: EL spectra of sample A3 at $T = 3.6$K . The curves have been normalized to the maximum peak height and offset for clarity.

It has been shown that the time for carriers to relax from GaAs into InAs QDs is much shorter than the GaAs exciton lifetime [69, 67]. Hence the fact that the dominant emissive feature is due to the GaAs, suggests that the QD

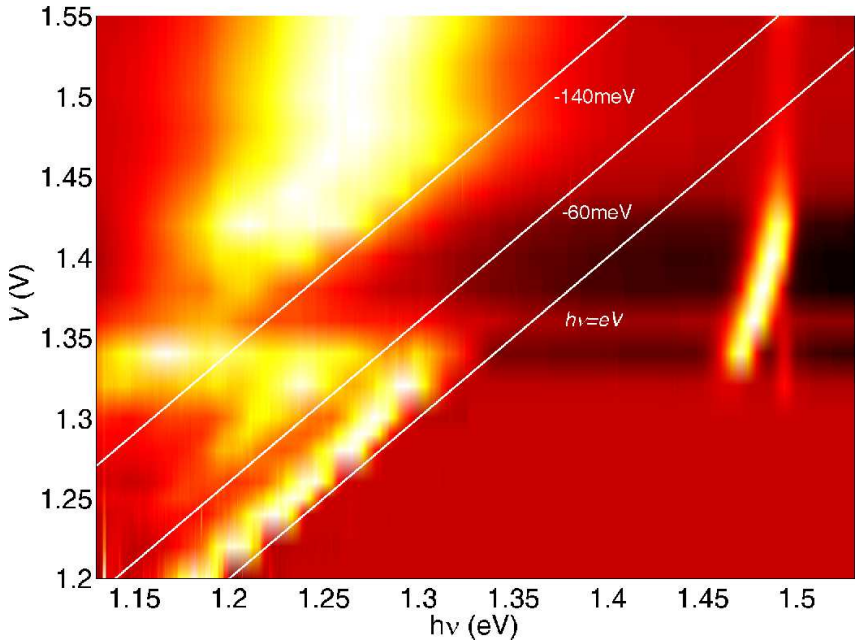

Figure 4.13: Colour-scale plot of the EL intensity vs V and emitted photon energy ($h\nu$) for sample A3 (T=3.6K). The three white lines denote $h\nu$=eV, eV-60meV and eV-140meV.

states are saturated and the carriers in the GaAs are unable to relax due to a lack of available states. Below V=1.58V, the QD emission becomes the dominant feature, indicating a switching point where the QD states are no longer saturated by the available carriers. It can be seen in Figure 4.13 that further reduction of the bias causes the maximum of the QD emission band to shift to lower energy as a result of reduced state filling effects until, when V∼1.48V, both the high energy emission edge and central maximum of the QD band begin to shift with the voltage at a value of $h\nu$=eV-140meV and eV-170meV, respectively. This behaviour continues down to V=1.36V and is accompanied by an increase in the relative intensity of the GaAs emission. The apparent reduction in the QD emission in this region is an artifact of the normalization algorithm used and reflects a reduction of the QD intensity relative to the GaAs, not a reduction of the absolute QD intensity. At this

point the GaAs emission is occurring at a higher energy than that at which the carriers are being injected and is thus up-conversion luminescence (UCL). This phenomenon is explored in more detail in Chapter 6. Below V=1.36V, the entire QD ensemble once again becomes the dominant feature, though instead of the single, broad emission band observed at higher biases there are now distinct, separate emission peaks, as can be seen in Figure 4.12. Reducing the bias still further brings the sample into an interesting regime of resonant behaviour. Two bands are observed with their high-energy edges at $h\nu$=eV and $h\nu$=eV-60meV, as indicated in Figure 4.13. The $h\nu$=eV band continues to the lowest measured bias, V=1.20V. Below this point the amount of light being emitted by the sample became too weak to measure. Figure 4.14 shows the EL spectra for sample A3 in the range V=1.32V - 1.46V.

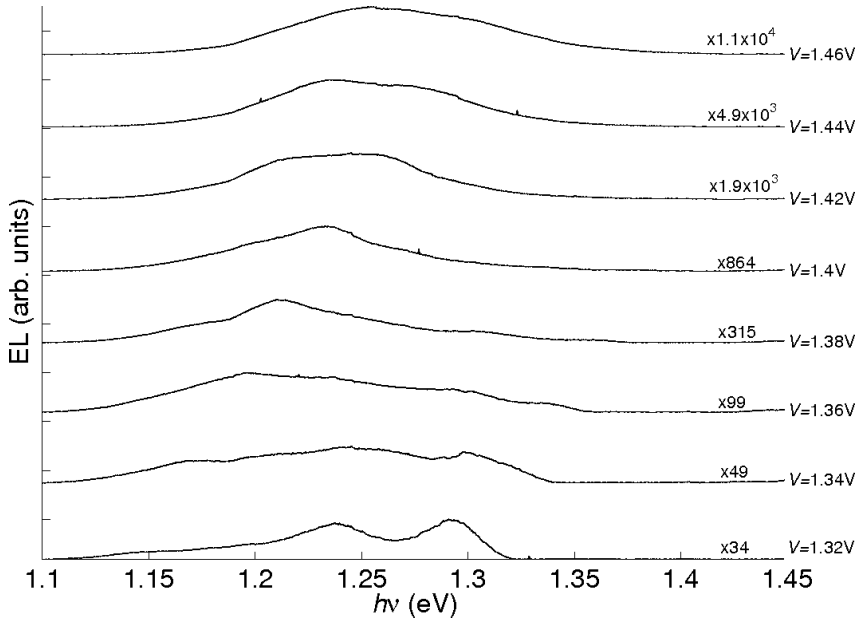

Figure 4.14: EL spectra of sample A3 at T=3.6K. The curves have been normalized to the maximum peak height and offset for clarity.

As the applied bias is lowered below V=1.46V, the structure of the EL changes gradually but markedly. The broad, bell-shaped emission that occurs at higher

biases (see Figure 4.12) begins to fragment and develop additional structure. The amount of structure increases with decreasing bias until the regime described above occurs, where resonant features dominate the spectra.

Figures 4.15 and 4.16 show the EL spectra as a function of bias and temperature, respectively. It can clearly be seen in Figure 4.15 that the high energy edge of the QD band is resonant with the applied bias.

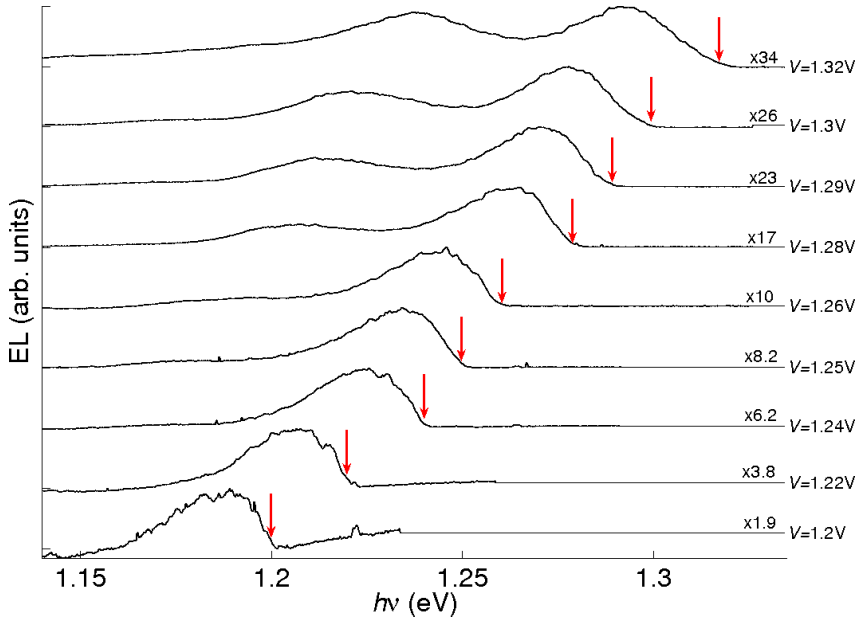

Figure 4.15: EL spectra of sample A3 at T=3.6K. The red arrows indicate the energy given to the carriers by the applied bias. The curves have been normalized to the maximum peak height and offset for clarity.

The temperature series shown in Figure 4.16 is taken at V=1.26V, which is well within this resonant regime. The intensity of the emission is not strongly affected by the temperature in the range over which data was taken, though at 30K a noticeable reduction in the intensity of the high-energy emission peak is observed. The increasing temperature does however lead to a 40% increase in the current between T=3.6K and 30K and this causes an increase in the intensity of the emission peak at $h\nu$∼1.18V due to state filling effects. It can

also be seen that the high energy edge of the QD band moves to higher energy with increasing temperature. The increase occurs faster than the rise in $k_B T$ indicating that some processes, other than purely thermal excitation of the carriers also play a role in the dynamics.

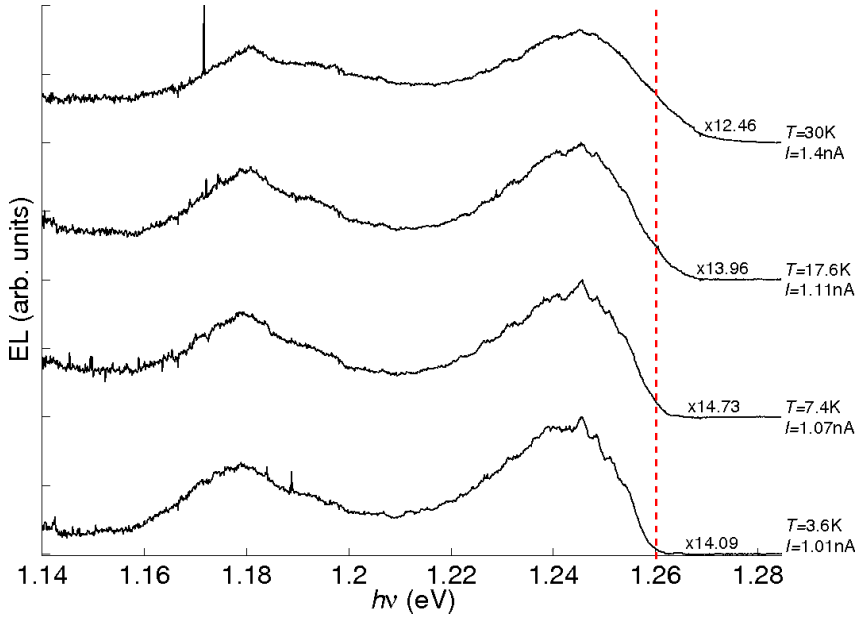

Figure 4.16: EL spectra of sample A3 at V=1.26V, as indicated by the dashed red line. The temperature and current are indicated to the right of the plot. The curves have been normalized to the maximum peak height and offset for clarity.

4.4 Discussion

The presence of resonant features in the $I(V)$ of sample A2, see Figure 4.6, provide clear evidence that both electrons and holes are able to be resonantly injected into the InGaAs QW via tunneling through the intrinsic region of a p-i-n diode. Having confirmed that bipolar resonant injection of carriers, i.e. resonant injection of both electrons and holes, in these structures is possible, then comparing the markedly different $I(V)$ characteristics of samples A1 and

A3 leads to the conclusion that the shoulders in the $I(V)$ of sample A3 are caused by the injection of carriers into confined states within the structure. The behaviour of sample A3 can be better understood by considering the following theory. Figure 4.17 shows a schematic diagram of a p-i-n junction, containing a layer of QDs situated in the intrinsic region, with zero applied bias.

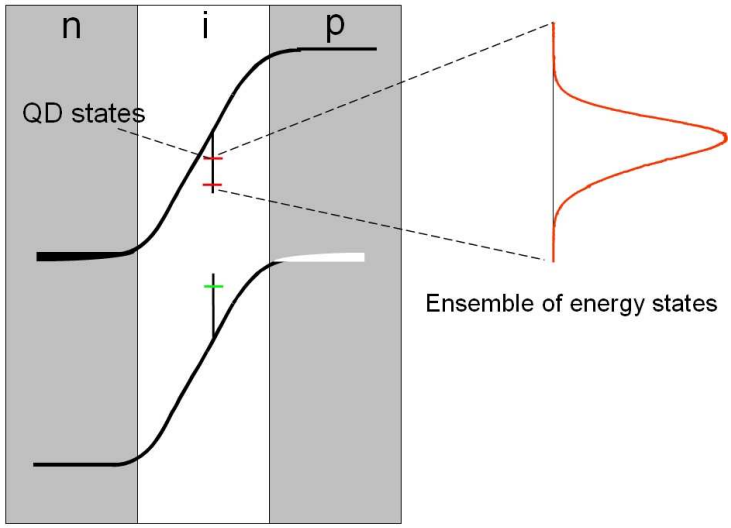

Figure 4.17: p-i-n diode containing QDs with zero applied bias. Electron and hole QD states are indicated by the red and green lines respectively. The inset shows the energy distribution of the QDs

As explained in section 1.2.1, the ensemble of QDs will give a range of energy states with a roughly Gaussian distribution, as indicated in Figure 4.17. By applying sufficient forward bias to take the junction above flat-band the situation becomes that shown in Figure 4.18.

Clearly it is now possible for the majority carriers, the electrons and holes, to flow freely across the junction. Most of these carriers will be captured by the QDs and, through a process of thermalization, are able to access the entire

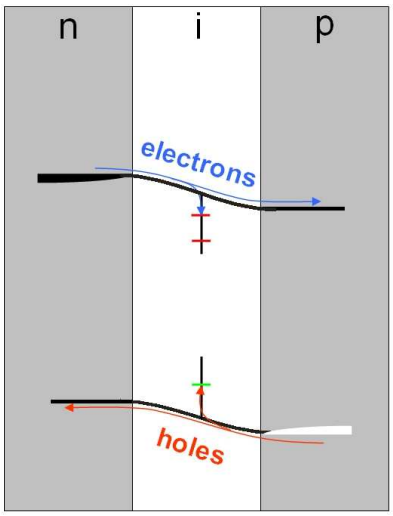

Figure 4.18: p-i-n diode containing QDs, biased above flat-band condition

dot distribution. When both the electron and hole states on a single quantum dot (SQD) are filled then recombination will occur. Due to the fact that the confined states in the QDs have a range of energies, carrier recombination from the ensemble will result in EL with a broad energy distribution and thus above flat-band the emission spectrum of this system will show a broad emission band. By reducing the applied bias so that the system is now below the flat-band condition, but still in forward bias, the situation becomes that shown in Figure 4.19.

In this configuration the electrons and holes are no longer able to flow through the junction as free carriers. However, correct alignment of the occupied states in the n and p-layers with the QD states makes it possible for electrons and/or holes to resonantly tunnel onto a QD. Once an electron or hole has been captured onto a QD the potential of the dot is altered in such a way as to make is easier for the oppositely charged carrier to also tunnel onto the dot. For example, when a hole tunnels onto a dot the negative charge on the dot

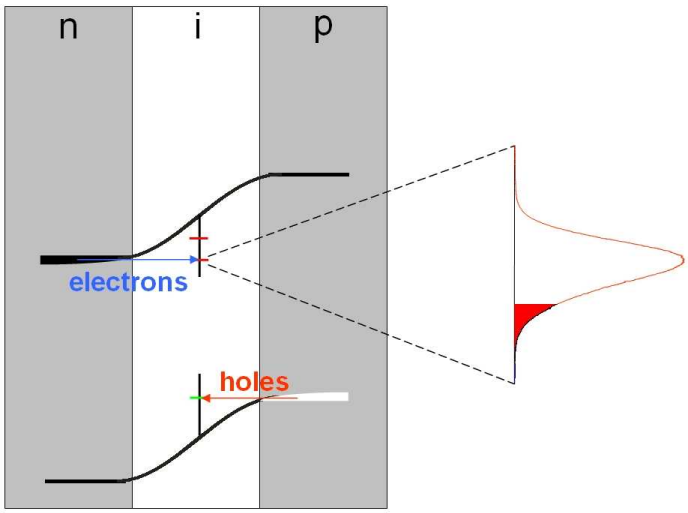

Figure 4.19: p-i-n diode containing QDs with positive bias but below flat-band condition. The inset shows how the number of QDs available to the carriers is reduced in this configuration.

is temporarily reduced. The resulting change in electric field brings the dot closer into resonance with the electron states in the n-layer. This causes a rise in the tunnel current, making it more likely for an electron to be captured onto the dot, restoring the system to equilibrium [70]. Given that there is an ensemble of QDs present then this process is likely to be affected by the remote charge due to carriers tunneling onto neighbouring QDs. When the dot has both an electron and a hole on it they are able to recombine and in this way it is possible to obtain EL from the dots with the system biased below the flat band condition.

An important point is that at zero applied bias the QD electron (hole) states are all above (below) the Fermi energy. Correctly tuning the applied bias thus allows for access to the entire QD distribution, unlike the case for the n-i-n diode, where at zero applied bias the ground states of the QDs are occupied [71]. As the carriers are being injected into the system with an applied bias

below that required for flat-band, then they do not have enough energy to access the whole distribution of dots. By decreasing the applied bias further the number of tunneling carriers, as well as the number of states available to those carriers, will also decrease. At low enough biases only a small number of states in the tail of the distribution will be available for the carriers to tunnel into, as indicated in Figure 4.19. In this low bias regime it should be possible to tune the voltage so that only a SQD is luminescing.

Returning to consider the experimental data for sample A3, three main bands below V_{fb} are identified in the inset of Figure 4.7. The band at $V \sim 1.05$V (B_1) does not have the characteristic bell-shape associated with a QD ensemble and does not contribute to any observable EL emission. The lack of EL emission could be due to the current in this region being too low for a sufficient level of carrier recombination to create an observable emission. However, given the shape of B_1 in $I(V)$, it seems more likely that these states are provided by defects within the structure that do not allow pathways for radiative recombination. The band at $V \sim 1.19$V (B_2) has a strong correlation with the observed EL emission for sample A3. The slight difference between the energy of B_2 in $I(V)$ and EL can be attributed to the fact that in $I(V)$ it only takes one of the carrier species to tunnel into a state to cause an increase in the current, whereas in order to observe EL emission from QD states, both electrons and holes must be present. If the second carrier species becomes resonant at a higher energy than the first then there will be an offset between the $I(V)$ and EL. The full-width at half maximum (FWHM) of B_2 in $I(V)$ is $\sim$88meV, which is in good agreement with the FWHM of the PL peak for a QD ground state reported in the literature [72]. The EL emission has the expected bell-shape of a QD distribution, though here the FWHM is $\sim$125meV for $V > V_{fb}$. The

final band (B_3) at V=1.39V has a FWHM of ∼125meV in $I(V)$, which is the same as the FWHM of the observed EL emission. However, this is too broad to be attributed to the QD ground state distribution and there is also no EL emission at the corresponding energy. This implies that any carriers entering B_3 relax quickly and recombine from the lower energy states. Considering this evidence, it is fair to attribute B_3 to the InAs WL and B_2 to the ground states of a QD band. The distinction is certainly blurred at the edges with excited QD levels present in the high energy edge of B_2 and the low energy edge in B_3, as reflected by the broad EL emission.

Carriers injected above the WL energy are able to enter the WL and thus have access to the whole QD ensemble, allowing them to relax into the lowest energy state available [35]. Looking at the data in Figure 4.13, it seems likely that the WL energy range is ∼1.42-1.46eV, which is in good agreement with the $I(V)$ data presented, allowing for the previously discussed offset between $I(V)$ and EL bands. At the point where the applied bias begins to drop below the high-energy edge of the WL, a marked change can be seen in the emission from the QD band. As the bias is reduced, the high-energy emission from the QDs dies out in direct correlation with the reducing bias. This indicates that as the carriers begin to lose access to the whole WL due to the reduced bias, relaxation pathways to certain QDs are cut off. This can be understood as the WL will not be of uniform thickness in the same way the QDs will not be of uniform size. If, as seems likely, there is a correlation between QD size and WL thickness, then it is possible that as the bias is reduced, the relaxation channels into the smaller, higher energy, QDs become closed off first, resulting in the observed cut-off of the QD emission band. Below the WL energy the carriers are no longer able to freely redistribute themselves amongst the QDs

and so will be significantly more likely to recombine in the QDs which they are injected into. Figure 4.20 shows the EL spectra for sample A3 with an applied bias of V=1.34V.

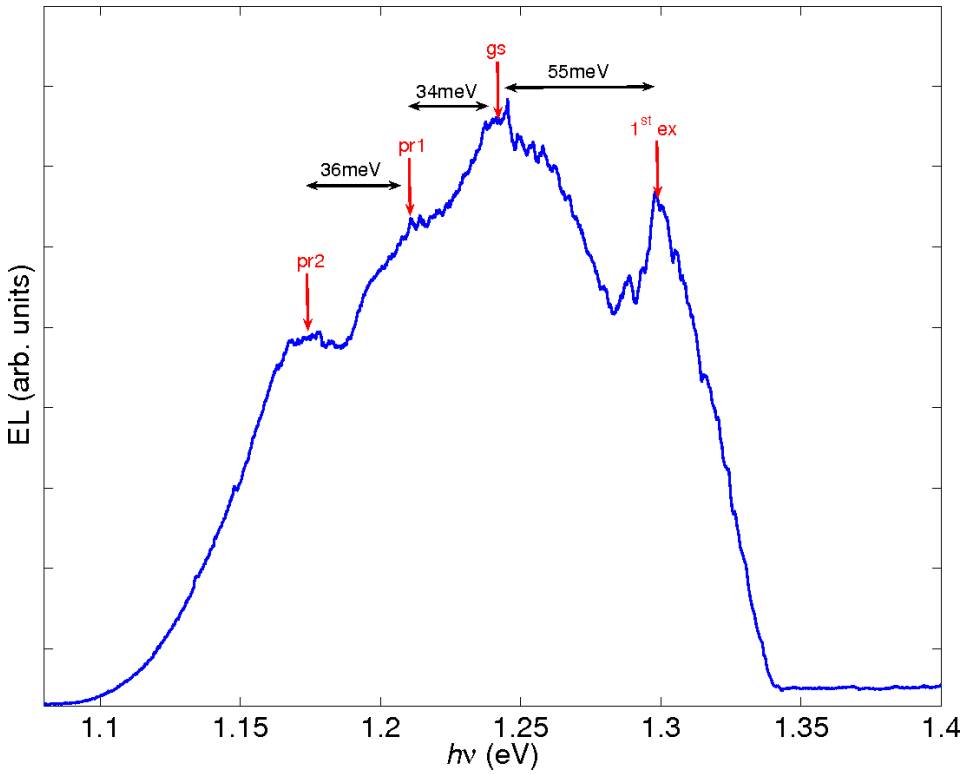

Figure 4.20: EL spectra at T=3.6K for sample A3 with an applied bias of V=1.34V. The red arrows and associated labels indicates the 1^{st} excited (1^{st} ex) and ground (gs) QD states and the first two phonon replicas (pr1, pr2). The energy separations between these features is also shown in the figure.

Four peaks in the EL spectra are identified in Figure 4.20. The two highest peaks in energy are attributed to the first excited (1^{st} ex) and ground (gs) state emissions of the QDs and have an energy separation of ∼55meV, which is in good agreement with the literature [73]. The other two emission peaks are identified as phonon replicas of the gs emission, having an energy separation of 34meV and a subsequent 36meV from the gs emission peak, which is in very good agreement with the GaAs LO phonon energy of 36meV [16, 74].

The structure of this emission indicates that the carriers are "locked in" to a particular range of QDs and find ways to recombine within this range rather than redistributing themselves throughout the ensemble. This, combined with the fact that the high-energy edge of the QD emission occurs at the energy supplied by the applied bias, provides strong evidence that below the WL a regime of resonant injection occurs. At lower biases a reduction in the phonon replica intensity is observed due to the reduced number of carriers tunneling, but the gs and resonant 1^{st} ex emission bands persist down to V=1.26V. At this point the lower energy emission band dies out so that only the resonant band remains (see Figure 4.13). This is attributed to crossing over from resonantly injecting into the 1^{st} ex state to injecting directly into the QD gs. At the biases immediately below V=1.26V, this distinction will be blurred as there will be overlap between ground and excited state emission energies; however, as the applied bias is reduced still further, the resonant emission energy can be seen to coincide with the energy of the gs emission peak observed at higher biases. This regime of resonant injection into the QD ground states persists down to the lowest biases for which the EL emission was intense enough to measure.

As can be seen in Figure 4.12, even at the lowest measured bias the EL emission is broader than that associated with a SQD. However, the rest of the observed behaviour of sample A3 fits very well with the above theory discussed at the start of this section and serves as a proof of concept. A properly designed structure should allow this idea to be extended such that an individual QD can be selected from the ensemble via the correct tuning of the applied bias.

4.5 Conclusion

A series of structures were grown in order to test the principle of bipolar resonant injection into QD states situated within the intrinsic region of a p-i-n diode. Comparison of $I(V)$ and EL data has shown that the entire ensemble is electrically accessible and that direct resonant injection into the ground and excited states of the QDs is possible. These findings open up the potential that with a well designed structure, correct tuning of the applied bias could allow the selection of a single quantum dot from within the ensemble without using advanced processing techniques. In order to produce a sample in which this single quantum dot selection is realised the device will need to be constructed so that both the electron and hole Fermi energies can be aligned with the low energy tail of the QD ensemble at the same bias. There are a number of device parameters which can be varied in order to achieve this. The size and density of the QDs can be altered by depositing different amounts of InAs and by varying the MBE growth conditions. This means that the energy that the ground state of the QDs falls at can be controlled to an extent. The primary mechanism for controlling the bias that the Fermi energies align at is positioning the QDs nearer, or further away from, the doped GaAs layers. This also allows the lever arm effect to be used to negate the fact that electrons and holes normally tunnel at different energies. As the tunnel current of the carriers depends exponentially on the tunnel distance then it may also be necessary to add a tunnel barrier to the structure to ensure that there is not a large excess of one carrier species in the dots, which can lead to bi-excitonic and Auger effects.

Chapter 5

Single Quantum Dot Emission

5.1 Introduction

In Chapter 4 it was shown that, via bipolar resonant injection of carriers into the QDs situated in a p-i-n diode, it is possible to achieve resonant EL emission. In order to investigate whether this effect could be used to achieve EL emission from a SQD situated within a large ensemble, without using advanced lithographic techniques, a series of p-i-n diodes containing QDs was grown. The samples used in this chapter are summarised in Table 3.7. Computer simulations indicated that there were a range of possible structures that could allow the realisation of SQD emission and as such a series of samples were grown. All these samples are variants of a basic p-i-n QD diode, and were all designed to achieve the goal of SQD emission.

5.2 Current-voltage characteristics

The device investigated in detail in this chapter was based on sample B1. A typical $I(V)$ curve for this device is shown in Figure 5.1.

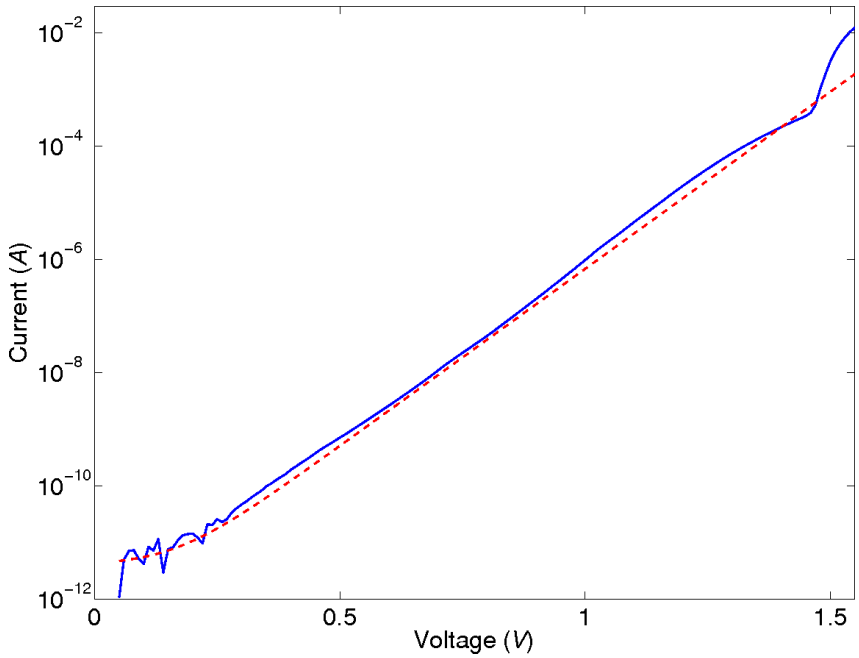

Figure 5.1: The blue curve shows the $I(V)$ plot for sample B1 at T=4.2K. The red curve shows the fit I_f=$Ae^{\beta V}$, where A and β are constants.

The current flowing through the system increases by around 10 orders of magnitude as the applied bias is increased from V=0 to 1.55V. A sharp increase in the current is observed at V∼1.5V, which corresponds to the bias V_{fb} for flat-band condition in GaAs p-i-n diodes. This large current above V_{fb} means that in this regime the device has a very bright EL. Comparing the experimental $I(V)$ to the I_f=$Ae^{\beta V}$ plot, also shown in Figure 5.1, it can be seen that there is increased current flow through the device in the region $1 \leq V \leq 1.5$, which is indicative of extra carrier states due to the presence of QDs. Note that the

features in the $I(V)$ curve around V=0.2V are due to background noise in the measurement device and not to Coulomb charging effects [75].

5.3 Electroluminescence spectra

A series of EL spectra for sample B1 is shown in Figure 5.2. The data were taken using the optical set-up (system 2), as described in Chapter 3. Data was taken for a large series of excitation biases, ranging from above V_{fb} to the lowest voltage at which it was possible to observe an emission. The maximum detector integration time used was 8 minutes and was limited to this value by the dark count of the detector. For comparison purposes, the EL spectra in Figure 5.2 have been normalised to their maximum intensity.

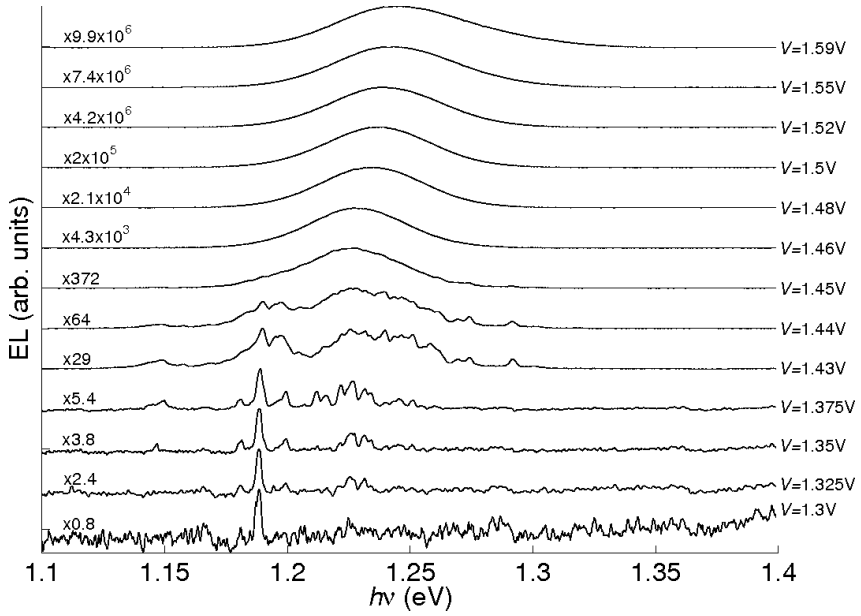

Figure 5.2: Series of EL spectra for sample B1 at T=10K. The excitation bias for each curve is given on the right hand side. The curves have been normalised to the maximum peak height and offset for clarity.

The spectra clearly show a marked change in the EL of the device as the excitation bias is lowered. At high bias there is an intense, bell-shaped emission band generated by the whole ensemble of QDs. It can be seen that there is a red-shift of the bell-shaped curve as the excitation bias is lowered. This red-shift continues with deceasing bias until $V \sim 1.45$V. After this point not only does the red-shift of the EL come to a halt, but the onset of structure on top of the bell-shaped background can also be seen. As the bias is decreased further, a series of distinct peaks starts to emerge above the background until, at $V \sim 1.35$V, the background ceases to be present and the spectrum evolves into a series of individual peaks. It is easier to track the evolution of the EL spectrum with varying V by using the colour-scale plot of Figure 5.3.

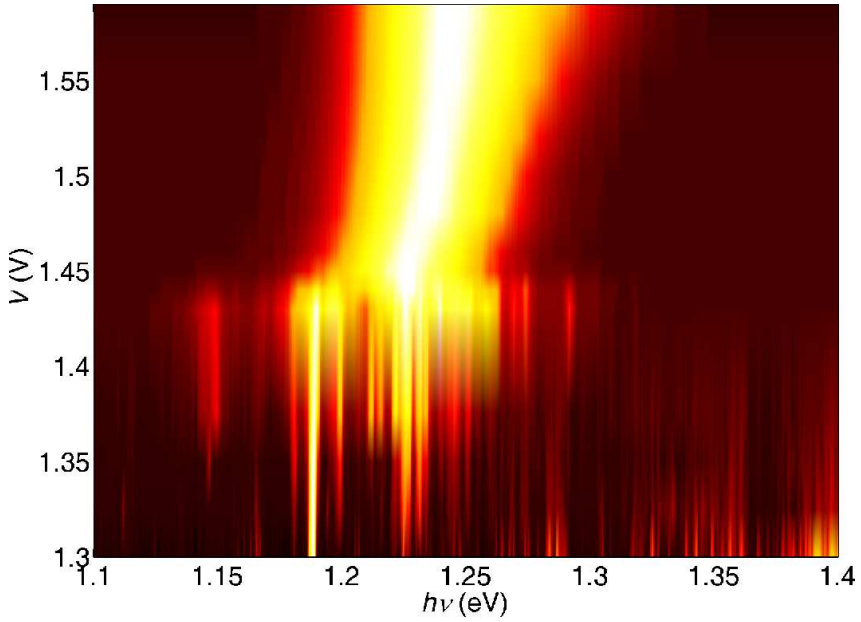

Figure 5.3: Colour-scale plot of the EL intensity vs V and $h\nu$ for sample B1 at T=10K.

Figure 5.3 shows clearly the red-shift of the broad QD emission band as the voltage is decreased below $V \sim 1.6$V, followed by the fragmentation of the spec-

trum into sharp lines for $V \leq V^*$=1.45V. As the bias is decreased, the number of visible peaks reduces until, at V=1.30V, which was the lowest voltage at which the EL was still visible, just a single, bright peak remains. The emission spectrum for V=1.30V is shown in Figure 5.4. The peak at $h\nu$=1.18eV is the only feature distinguishable above the background noise. Referring back to Figures 5.2 and 5.3, it can be seen that this peak can be distinguished in all spectra for $V \leq$1.44V. The energy at which this peak occurs is thus independent of V, but its intensity decreases with decreasing V.

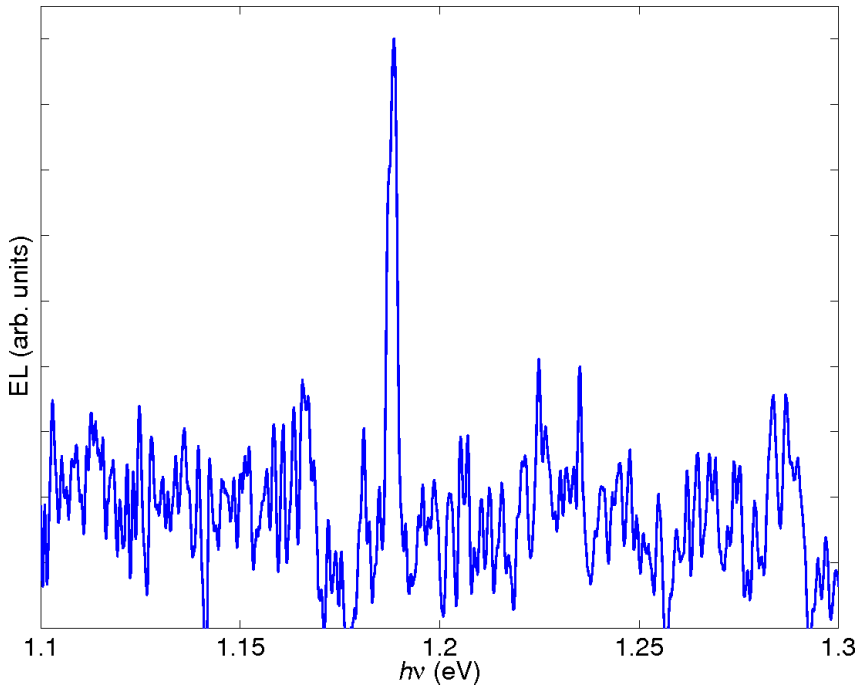

Figure 5.4: EL spectrum for sample B1 at V=1.30V and T=10K.

5.4 EL spectra of high and low density QDs

The EL of several devices was studied. When analyzing this data some clear differences in the EL of devices based on different QD samples was observed.

Further analysis indicated that the factor responsible for these differences was the QD-density.

The results for the high and low QD-density devices are provided by samples B1 and B2, respectively. Figure 5.5 shows an example of EL spectra for the low QD-density sample (sample B2).

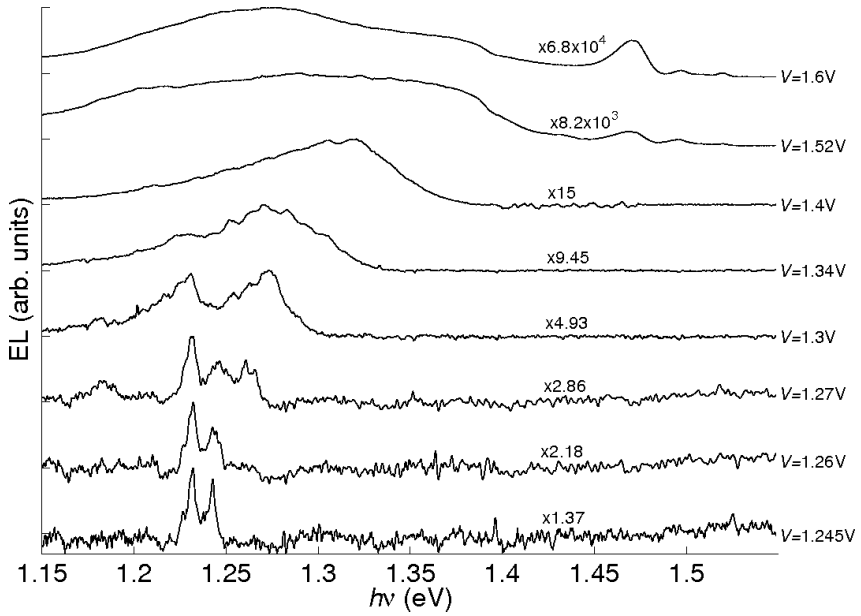

Figure 5.5: Series of EL spectra for the low QD-density device (sample B2) at T=10K. The excitation bias for each curve is given on the right hand side. The curves have been normalised to the maximum peak height and offset for clarity.

The spectra follow the same general trend as those of the high-density sample shown in Figure 5.2, with a broad emission spectrum at high bias followed by a fragmentation into a series of individual peaks as the excitation bias is lowered. However, closer examination reveals some differences in the two sets of spectra, which are better revealed in the colour-scale images of the samples shown in Figures 5.6 and 5.7.

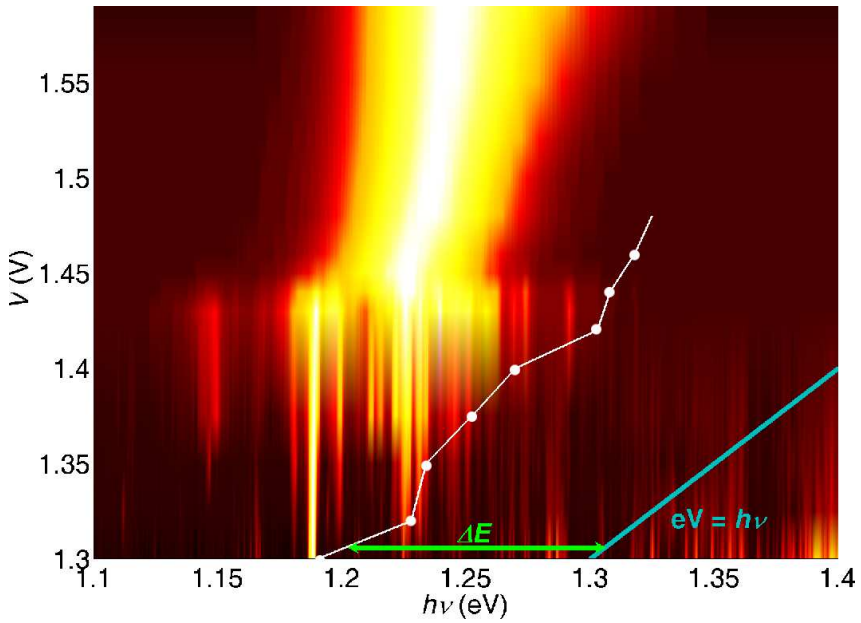

Figure 5.6: Colour-scale plot of the EL data for the high QD-density device (sample B1). The blue line shows where the excitation bias equals the emission energy; the conjoined white circles mark the high-energy edge of the emission spectrum at the given voltage; the green arrow indicates the energy difference between injection and emission.

The main feature of interest is the energy difference, ΔE, between the excitation energy, eV, provided by the applied bias and the high-energy edge, $h\nu_t$, of the EL emission (indicated by the white circles on the colour-scale plots). In the device with a high QD-density, ΔE is consistently large. We find that $\Delta E = eV - h\nu_t = 150$meV at $V = 1.45$V and $\Delta E \sim 100$meV at $V = 1.3$V. This indicates that the electrically injected electron-hole pairs always relax a considerable amount of energy ($\sim$100meV) prior to radiative recombination in the ground states of the QDs. By contrast, in the device with a low QD-density, the energy relaxation is much smaller: $\Delta E \sim 20$meV at $V = 1.45$V and $\Delta E < 1$meV at $V = 1.3$V. This small value of ΔE at 1.3V indicates that the electron and hole recombination is taking place from the QD states onto which the carriers are injected.

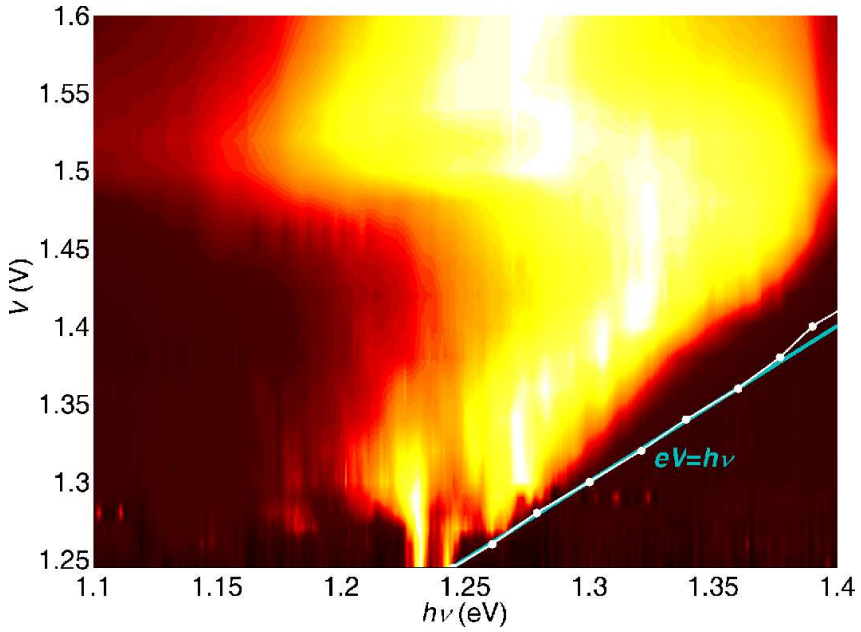

Figure 5.7: Colour-scale plot of the EL data for the low QD-density device (sample B2). The blue line shows where the excitation bias equals the emission energy, the conjoined white circles mark the high-energy edge of the emission spectrum at the given voltage

In the low QD-density device, the data also show a blue-shift of the broad EL emission band as the excitation bias is decreased from V=1.6V down to $V\sim$1.5V. This energy shift is consistent with the dominant carrier recombination changing from taking place in the ground states to the excited states of the QDs.

5.4.1 Micro-electroluminescence

In order to better understand the origin of the emission from the large area mesas studied in the previous sections, μEL measurements were performed on sample B3. The results from an EL experiment in which a webcam was used to image the sample at various biases are shown in Figure 5.8

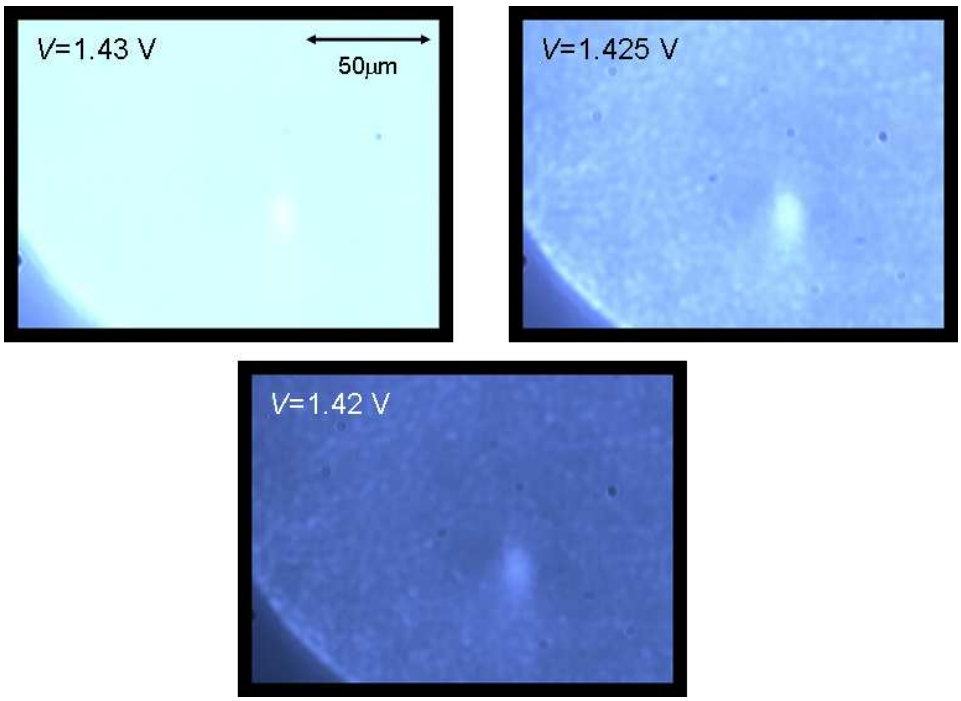

Figure 5.8: Webcam images of EL emission from sample B3 at T∼15K. The applied bias for each image is given in the top left corner. The bright, light blue areas indicate high-intensity emission.

The images shown in Figure 5.8 are for a 200μm diameter mesa, though only a portion of this area is shown. The biases shown are chosen so that the sample is imaged at a bias just below V_{fb}. It can clearly be seen that at V=1.43V the whole mesa is emitting brightly, but that there is already a region of enhanced emission, just below and to the right of centre of the image. As the bias is reduced to V=1.425V, the inhomogeneity of the emission becomes apparent, with a mottled effect indicating that some areas of the mesa are more optically active than others. There is no clear pattern to this mottling, with the areas of higher intensity distributed seemingly at random across the mesa. The larger, bright "hot-spot" that was evident at V=1.43V is still present. At V=1.42V the same mottled pattern can still be observed, though there is an obvious reduction in the emission intensity from the entire area of the diode.

Figure 5.9 (see overleaf) shows a series of images constructed from the μEL data taken on sample B3. Each pixel in the left hand image represents a single μEL data point, which is 10μm in length and contains ∼8000 QDs. The overall image is constructed by bringing together individual data points from across the sample area. The right hand images show the individual μEL spectra from the pixel indicated by the arrow in the left hand image. In the image of Figure 5.9 with V=1.42V, the sample is already in the regime where the emission across the mesa shows the inhomogeneous, mottled effect. This is reflected in the individual μEL spectra, which show a broad background emission that has some structure on top of it, such as the peak highlighted by the blue arrow at $h\nu$=1.276eV, see Figure 5.9(b). In the second image, taken at V=1.37V, the amount of emission from the sample is greatly reduced, with just a single, bright "hot-spot" and a few scattered, low-level emission points. This is consistent with the webcam data shown in Figure 5.8. In the individual spectra it can be seen that the background emission in the energy range shown is virtually non-existent and that there are only two emission peaks. For V=1.32V the emission intensity is a factor of 10 lower than at V=1.42V. This low intensity means that background light levels have a greater effect on the experiments and this is reflected in the apparent increase in the level of mottling in the left hand image. At this bias the size and intensity of the "hot-spot" emission is reduced from that at V=1.37V. In the individual spectra only the emission peak at $h\nu$=1.276eV remains distinct above the background noise. This peak has a FWHM of ∼0.2meV, which is consistent with that reported in the literature for a single QD at T=10K [76, 77].

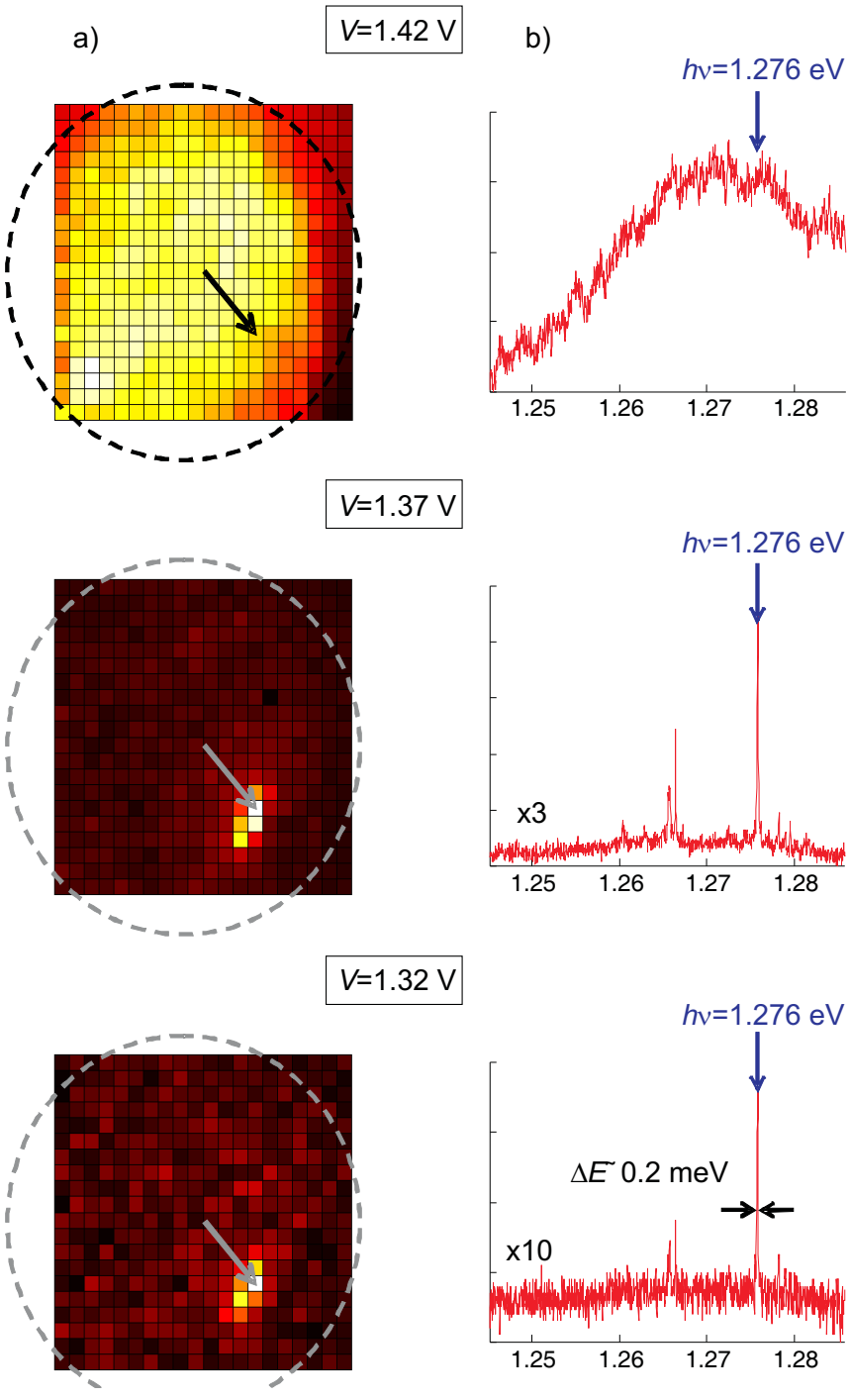

Figure 5.9: a) μEL images for sample B3 at $T\sim$15K. Each pixel has length l=10μm and the dashed circular line illustrates the mesa boundary. b) EL spectra from the pixel indicated by the arrow. The applied bias is shown for each figure.

5.5 Analysis

5.5.1 Fragmentation of EL spectra

The data presented in section 5.3 shows the fragmentation of a bell-shaped EL spectrum into a series of individual peaks as the excitation bias is lowered. A similar, but less pronounced, effect is seen in sample A3 discussed in Chapter 4. In sample A3, structure emerges as the applied bias is reduced below V_{fb}, but there is a more persistent level of emission at the energies between the emerging peaks. The way that the EL of the samples changes during this progression from broad-band to single peak emission can be used to understand some aspects of carrier dynamics in the system.

Whilst achieving single peak emission requires careful selection of the device, the splitting of the bell-shaped emission curve into a series of discrete peaks has been seen in a number of devices based on all samples in group B. The voltage, V^*, at which this splitting occurs is $\sim$1.45V in all devices. This characteristic voltage corresponds to the bias required for injection of carriers into the energy states of the InAs WL, whose low-temperature absorption is typically observed at $h\nu\sim$1.4eV [78].

As discussed in Chapter 4, the WL makes a spatial connection between the QDs in the ensemble. This means that the electrons and holes can move from QD to QD if they have sufficient energy to be excited into the quasi-2D sub-band of the WL. However, below V^*, the WL is no longer accessible to the carriers, meaning that carriers tunneling into the sample have fewer relaxation channels open to them and are much more localized. This leads to emission

taking place from the QDs onto which the carriers are injected, instead of from across the whole distribution.

There has already been work looking into the role that the WL plays in SAQD systems. The effect of the WL has been modeled using computer simulations and it was found that the WL and QDs must be treated as a single, unique system, as opposed to two separate ones, in order to correctly model the density of states. The combined system approach is especially important when the density of QDs is high, where it is shown that strong QD/WL coupling leads to enhanced splitting and mini-band effects on QD states [35].

The limited access of carriers to the WL can be used to explain the reduced ability of carriers to redistribute themselves throughout the QD ensemble, but it does not explain why certain peaks remain in the spectra, nor does it explain the different behaviour of samples of type A and B. One possible explanation is if there are "fingers" in the potential profile of the emitter [79]. These fingers are a characteristic of some disorder in the potential energy profile, possibly caused by the diffusion of dopants. In general, sample group B devices show higher background current levels, greater variability of devices based on the same sample and less reproducibility of data between cool-downs, all of which are indications of a higher degree of disorder as compared to group A samples. With this being the case, it would be expected that there would be more variation in the potential profile of group B devices. This is especially the case for sample B1, where the doped contact layers are separated from the QDs by a much thicker GaAs spacer layer than in sample A3, allowing greater scope for the diffusion of dopants. This is shown schematically in Figure 5.10.

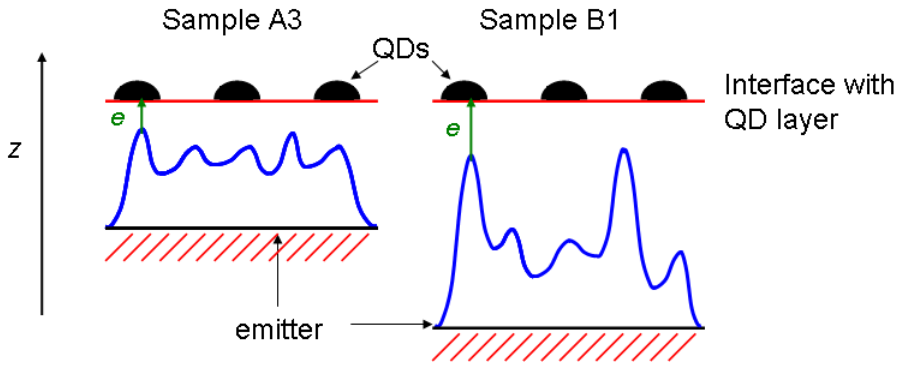

Figure 5.10: Schematic showing potential fluctuations in samples A3 and B1. The black line indicates the nominal emitter interface given by the growth sheets, with the potential fluctuations shown in blue.

Both samples will have a certain background level of potential fluctuation. However, in sample B1 it seems likely that the greater disorder results in fingers with a much greater variation in size. As the tunnel current depends exponentially on the tunnel distance, this greater variation will mean that the fingers have an even more pronounced effect in sample B1 than in A3. In sample B1, the preferential current flow from the largest fingers will effectively isolate certain areas within the QD ensemble, causing these to emit with a much greater intensity, while the emission from the rest of the ensemble is effectively masked. On the other hand, in sample A3 the variation in the potential is not great enough for this to occur, and instead manifests itself as an enhancement of the emission above the background at certain energies. This finger model is supported by the μEL data shown in section 5.4.1. The spatially inhomogeneous EL arising from the device is a clear indication that some areas of the diode, and hence some QDs, receive more current and thus emit more light than other areas. This can be explained if the current flowing from the emitter to the QDs is not constant across the whole area of the diode.

5.5.2 Evidence for single QD emission

To interpret the data shown in section 5.3 the integrated area, A, of the QD EL spectrum was considered. At a given bias, A is equal to the radiative component, I_r, of the electrical current I. This is given by

$$I_r(V) = \hat{N} e \tau^{-1}, \tag{5.1}$$

where τ=10^{-9}s is the radiative lifetime of an exciton in a QD [80],

$$\hat{N} = \sum_{i=1}^{N} f_i(V) \tag{5.2}$$

is the number of excited QDs, f_i defines the occupancy of an electron-hole pair on a particular dot, i, within the ensemble and N is the total number of dots in the device. By assuming that for $V \geq \mathrm{V}_{fb}$ the quantum efficiency is close to unity, i.e. $I_r = I = A$, we can determine the value of $\hat{N}$ at all biases. This is given by

$$\hat{N} = \frac{A\tau}{e}. \tag{5.3}$$

Figure 5.11 shows the voltage dependance of I and $\hat{N}$.

Using equation 5.3 and the recombination current data for V>1.5V, we find that for V>1.5V, $\hat{N} = 10^8$, which corresponds to the number of QDs there are in a 400μm mesa with a dot-density of 10^{11}cm^{-2}. This means that above V_{fb} every dot in the device is emitting at a rate of τ^{-1}. Below flat-band condition I_r becomes much less than I. In particular, for V=1.30V we find that $\hat{N} \cong 3$.

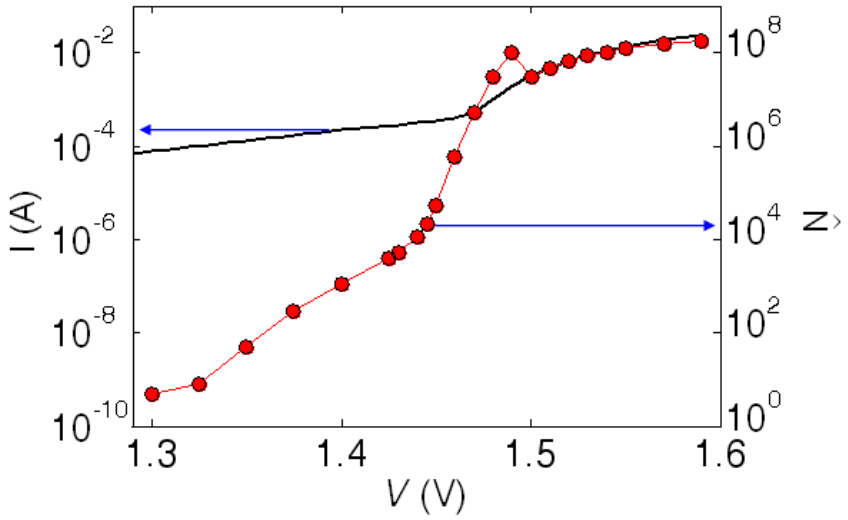

Figure 5.11: The black curve shows the current flowing through the device as a function of the applied bias. The red curve shows the recombination current obtained by integrating the EL spectrum at the voltage indicated by the red circles. The right hand axis shows the number of excitons contributing to the EL signal. Both data sets are for T=10K

This result suggests that at V=1.30V, the EL spectrum is due to exciton recombination from only 3 QDs.

The FWHM of the single peak shown in Figure 5.4 is $\simeq$3.6meV and is limited by the dispersion of the spectrometer as a 2mm slit width was used to optimise the collection of light. The estimate of the number of dots contributing to the EL spectrum suggests that this emission arises from a SQD, or a few QDs, emitting in a narrow energy range. Although the μEL data shown in section 5.4.1 is from a different sample, the observed single peak, with a FWHM characteristic of SQD emission, is further evidence that SQD emission can be achieved from large area p-i-n diodes.

5.5.3 Carrier Relaxation Mechanisms

It can be seen from the data presented in section 5.4 that in samples with large QD-density, carriers relax energy before recombining. This relaxation of energy is attributed to Auger processes.

Auger recombination is an important non-radiative process in semiconductors. One example of an Auger process is an electron-hole pair recombination followed by a transfer of energy from the electron-hole pair to a free carrier, which is then excited to a higher energy within the band [81]. In QD systems a limiting factor in Auger recombination is the availability of states at the correct energy to allow the second electron to take on the energy from the electron-hole recombination, though this restriction is eased by the continuum of states present in the WL. When there are energy states available, it has been shown that Auger recombination is an efficient process with capture times of the order of picoseconds [82], making this an important factor in the carrier dynamics of QDs [68, 80, 83].

The difference in the sizes of the high and low-density QDs mean that the excited states of the high and low-density QDs occur at different energy levels. The smaller size of the high-density QDs means that there is a larger energy gap between the ground and first excited state, and that the first excited state is closer in energy to the WL than in the low-density QDs. Consider two electrons occupying excited states of the same QD. In order for one of the electrons in the excited state to be able to relax to the ground state it must lose energy. It can do this by transferring the excess energy to the second electron, for example via the Coulomb interaction. In order for this process to be facilitated the second electron must have an energy state available to

it at the required energy. Studies on dots of a similar size to those in the high-density device found that the energy gap between the electron ground and excited state of the dots was larger than the gap between the excited state and WL continuum [84]. This means that for this type of dot, the Auger mechanism will be enhanced as there will almost certainly be an energy level at the correct energy in the WL continuum for the second electron to occupy [85], allowing the first electron to relax to the QD ground state.

Although the evidence presented here does indicate that Auger processes are an important mechanism in these samples, it has not yet been proved that they are the *dominant* mechanism, as is asserted here. The evidence that has led to the attribution of Auger processes being the dominant mechanism will become more clear in Chapter 6.

5.6 Conclusion

It has been shown in different samples and using different experimental set-ups that bipolar resonant injection of carriers into a large ensemble of InAs QDs can be used to achieve emission from a single, or few, QDs within a large ensemble. The process of achieving SQD emission did not work exactly as expected on the basis of the experiments performed in Chapter 4. Instead of the emission occurring from a QD situated in the low energy tail of the distribution, the emission occurred from a random energy within the QD ground states and was different for each device. To explain this result, a finger-like emitter model was suggested. The spatial variations in the emission across the sample that are evident in the μEL experiments show that potential fluctuations in the

emitter profile create variations in the efficiency of carriers tunneling between the emitter and the QDs. This means that certain QDs, not necessarily in the low energy tail of the distribution, will be preferentially selected. In the low bias regime, where only a few carriers are being injected into the sample, this preferential selection channel is the key factor in determining which QD is the last to remain emitting. Also the energy of the QD emission varies between different devices as the potential fluctuations tend to be different in each device.

It has also been shown that the WL is extremely important in the behaviour of the samples measured. The ability of carriers to enter the WL is, to a large extent, able to smooth out the variations caused by the fingers in the potential profile. The WL also plays an important role in Auger processes.

Part of this work has been published in *Applied Physics Letters* [86]

Chapter 6

Up-Conversion Electroluminescence

6.1 Introduction

Up-conversion luminescence (UCL), i.e. emission of photons at energies larger than that supplied by the external voltage source, has been observed in PL experiments, in rare earth ions [87], bulk semiconductors [88] and has also been observed in self-assembled InAs/GaAs QDs [89].

To date UCL in QDs has been reported only in PL experiments, where it is difficult to distinguish the mechanism responsible for the up-conversion (UC) process. In this chapter a study of UCEL in QDs is presented, where the electrical injection of carriers makes it possible to probe the carrier dynamics of UC in a novel way.

In this chapter the device investigated in detail is based on sample B1. The data presented in this chapter was taken using the magneto-cryostat and the optical set-up (system 1) discussed in Chapter 3.

6.2 Current-voltage characteristics

The low-temperature (1.8K) $I(V)$ characteristic for the sample B1 device is shown in Figure 6.1

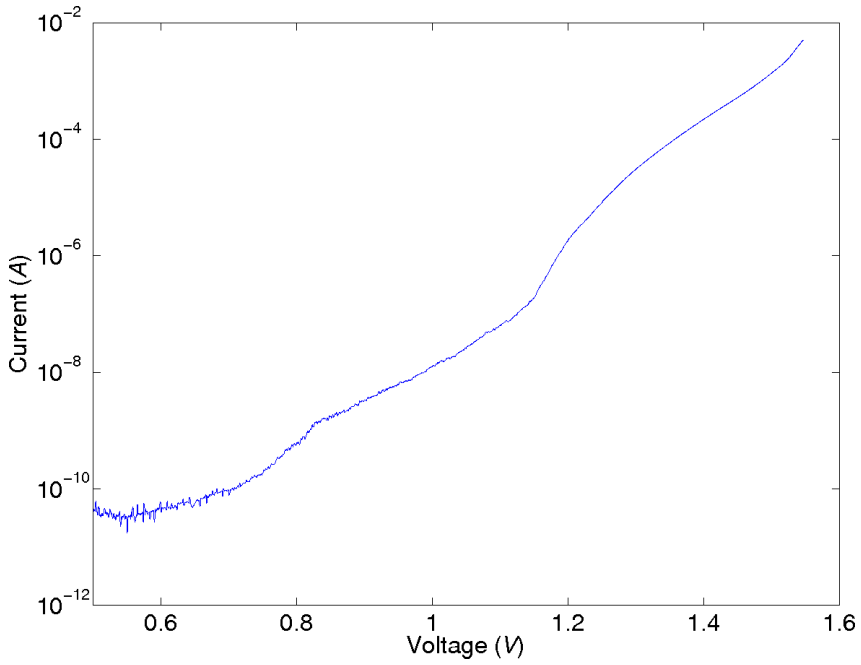

Figure 6.1: $I(V)$ plot for sample B1 device at T=1.8K.

As can be seen, the current flowing through the system increases by around 8 orders of magnitude as the applied bias is increased from V=0.5V to 1.55V. There is an increase in the current observed at V=1.52V, corresponding to V_{fb} for GaAs p-i-n diodes. It can also be seen that there is a current of a few μA flowing through the device in the region 1.2V$\leq V \leq$1.4V, which corresponds

to the characteristic energies of the QDs in this device. Indeed, there is a clear shoulder visible in this region, which is suggestive of electrons and holes tunneling through dot states. Figure 6.2 shows the logarithmic derivative of the $I(V)$, $G_L = \frac{d[log(I)]}{d[log(V)]}$. This can be thought of as a way of probing the effective density of states and reveals the resonant features of the $I(V)$ more clearly. The peak at $V \approx 1.18$V is in good agreement with the expected QD energies. There is also a small increase in current at $V \sim 0.8$V, which indicates the presence of deep levels in the band gap in the intrinsic region of this structure, for example due to the donor defect EL2 [90].

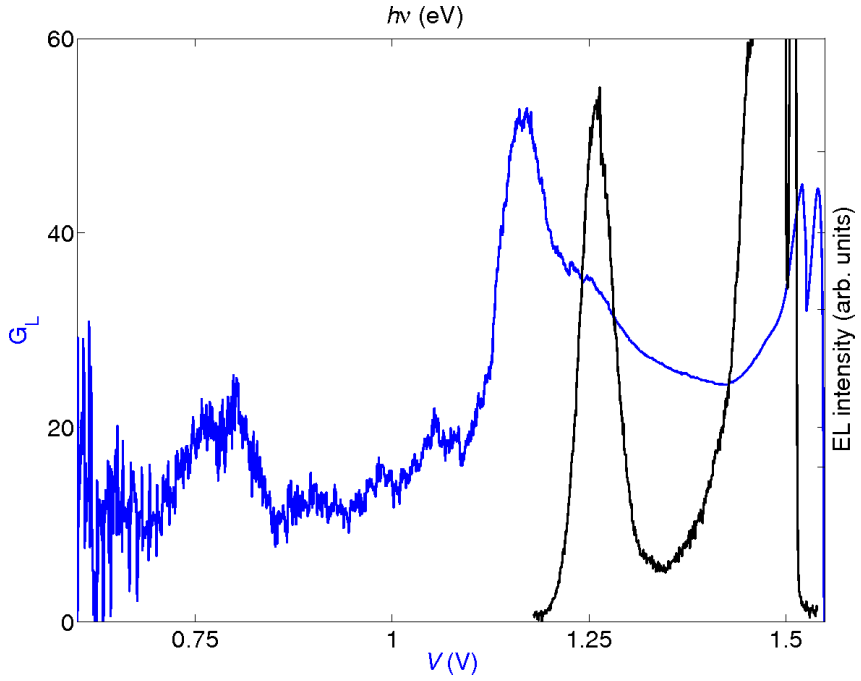

Figure 6.2: Logarithmic derivative of the $I(V)$ curve shown in Figure 6.1 (blue curve) and EL spectrum of sample B1 at V=1.54V and T=3.6K (black curve). The axes corresponding to each curve are indicated by the appropriately coloured axis labels.

Band structure calculations similar to those reported in Ref. [91] indicate that the current onset at ∼1.17V is consistent with the resonant tunneling of holes into the QD ground states, followed by electron tunneling at ∼1.25V.

EL emission from the dots is observed when both types of carriers are injected into the dots, which explains why the EL band has its peak at higher energy than the current onset at ∼1.17V. The feature at ∼0.8V is not observed in all samples.

6.3 EL Spectra and UCEL

Figure 6.3 shows EL spectra at different excitation biases. There are three distinct regions of emission that can be observed.

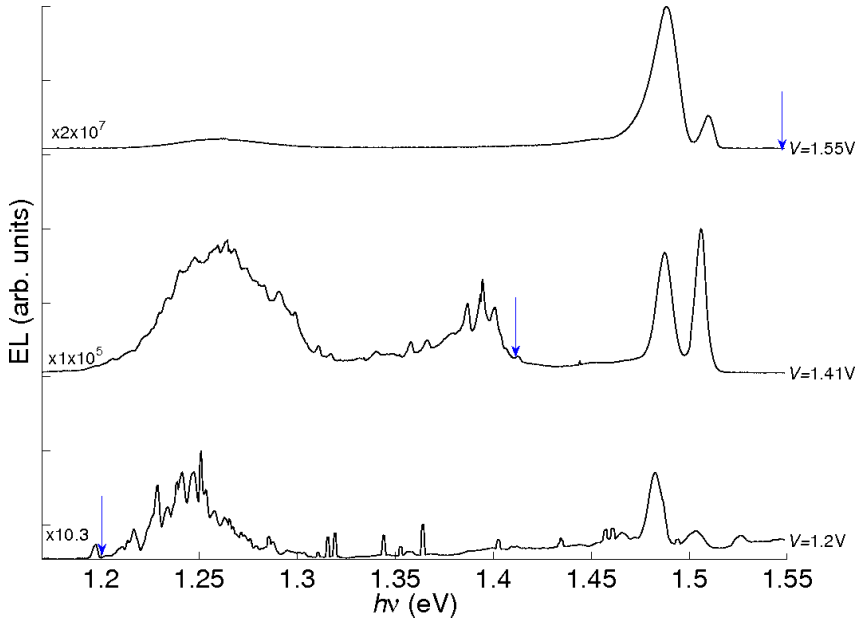

Figure 6.3: EL spectra at V=1.55V (top), 1.41V (middle) and 1.20V (bottom), as indicated by the arrows, for sample B1 (T=3.6K). The curves have been normalised to the maximum peak height and offset for clarity.

At high energy there are two emission lines at $h\nu$=1.51eV and $h\nu$=1.49eV. These are due to the near band-edge recombination of electrons and holes as FEs and in eA^0 states in the GaAs layers. There are also distinct, broad emission bands at $h\nu$∼1.44eV and $h\nu$∼1.25eV due to electron-hole recombination

from the InAs WL and from the QDs, respectively. Additional insight into the emission data is gained by considering the colour-scale representation of the data in Figure 6.4.

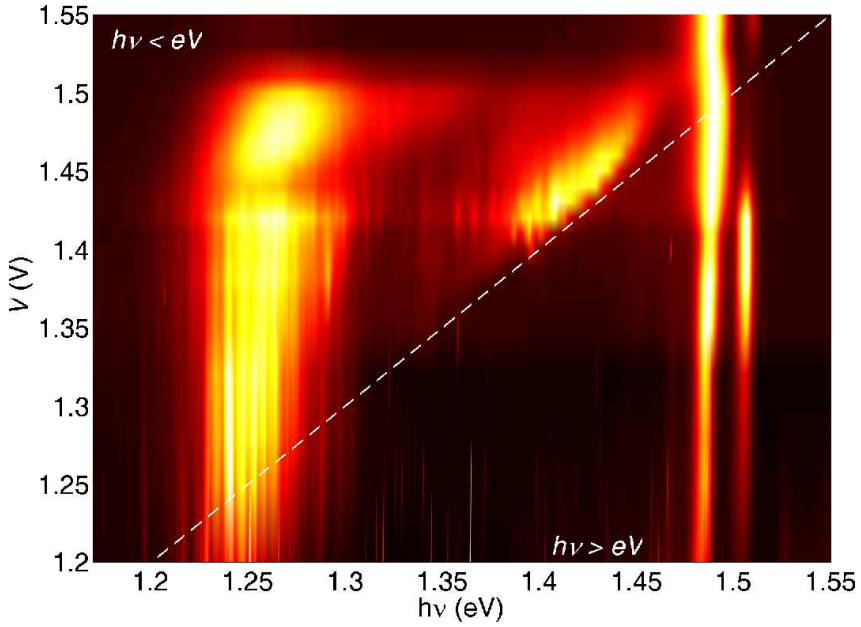

Figure 6.4: Colour-scale plot of the EL intensity vs V and emitted photon energy ($h\nu$) for sample B1 at T=3.6K. The dashed white line represents where condition $h\nu = eV$.

The three distinct areas of emission corresponding to the GaAs, WL and QDs are immediately clear in Figure 6.4. It can also be seen, by looking below and to the right of the dashed line in this figure, that a significant amount of the light being emitted by the device as the excitation bias is decreased is UCEL.

At excitation voltages above V_{fb}, the EL spectrum is dominated by the eA^0 and FE peaks. As the excitation bias is decreased from V=1.55V to V=1.51V, the eA^0 peak experiences a slight blue shift of ~2meV whilst the intensity of the FE emission decreases relative to the eA^0 emission. This blue shift is attributed to hot carriers entering the eA^0 states as the excitation bias drops below the level of the FE states.

As the excitation bias is decreased below the energy of the GaAs band edge, the relative intensity of the WL increases and its emission band starts to become visible in the spectra. When the excitation bias becomes resonant with the WL energies ($h\nu$∼1.43-1.47eV), the intensity of the GaAs emission decreases much more rapidly than that from the QDs and WL. This indicates that the carriers are being resonantly injected into, and recombine from, the WL states. At the same time, the FE emission peak increases in intensity relative to the eA^0 peak. At this point the emission associated with the GaAs is UCEL. Below V∼1.41V, the emission from the WL dies away and the QD emission band begins to fragment into a series of individual peaks [86].

In the regime where the excitation bias starts to come into resonance with the QD levels, it can be seen quite clearly in Figure 6.4 that the emission peaks within the QD band that are now at higher energy than the excitation bias begin to decrease in intensity relative to those which are still at a lower energy than that provided by the excitation bias. This trend continues with decreasing bias and it can be seen that as the lowest biases are reached, a previously faint peak at $h\nu$=1.18eV begins to become more prominent in the emission spectra. In the EL spectra shown in Figure 6.5, this peak can be seen clearly and is in fact the only visible emission that is not due to UCEL.

There are clearly two distinct regimes of UCEL; firstly, at low excitation voltages, there is UC involving the QD energy band (UC_{QD}) and secondly there is UC involving the GaAs states (UC_{GaAs}). The UC_{GaAs} involves UC energies up to ∼340meV, which are much larger than $k_B T$≈0.31meV at T=3.6K. While PL experiments on CdSe/ZnS colloidal QDs have yielded UC of ∼413meV [92],

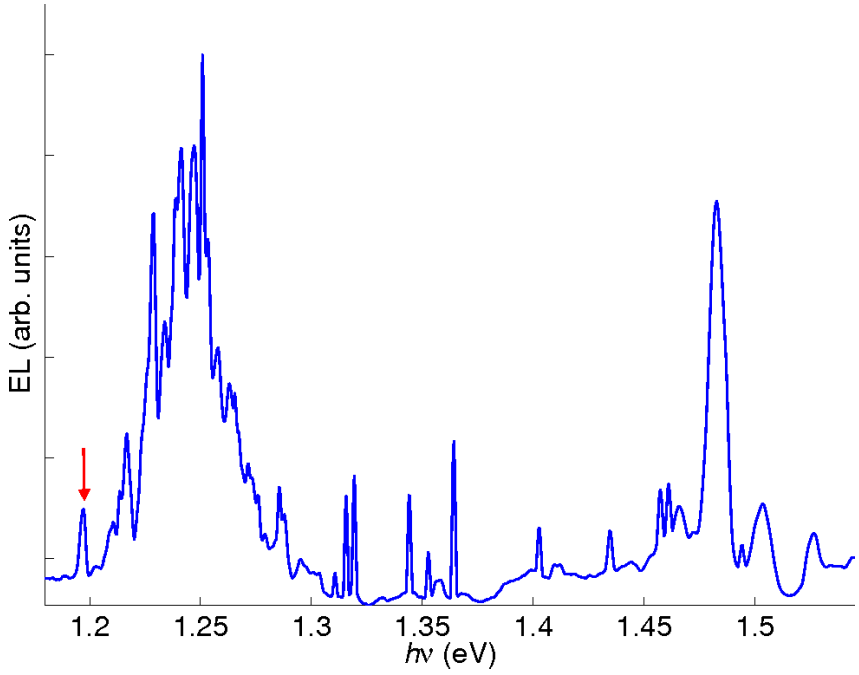

Figure 6.5: EL spectra for V=1.20V and T=3.6K for sample B1. The red arrow highlights the peak at $h\nu$=1.18eV, which is discussed in the text.

to the best of our knowledge this is the largest UC reported on QDs inside a semiconductor device.

In an ideal p-i-n diode, the total integrated EL intensity should roughly scale with the electrical current, I. In Figure 6.6 the integrated EL intensities of the QDs (1.18eV-1.30eV), the WL and excited states (1.30eV-1.45eV) and the states near the GaAs band edge (1.45eV-1.54eV) are plotted normalized to I (as shown in Figure 6.1) on a logarithmic scale. For the spectra with the two lowest voltages, a correction for the background was applied before integration.

Above V_{fb} all intensities scale with I. However, when the excitation bias is lowered below V_{fb}, the GaAs intensity drops sharply, but then follows the WL and the QD intensities. Tuning the bias below $V \approx$1.4V, the normalized WL emission drops exponentially, while the luminescence from the GaAs and the

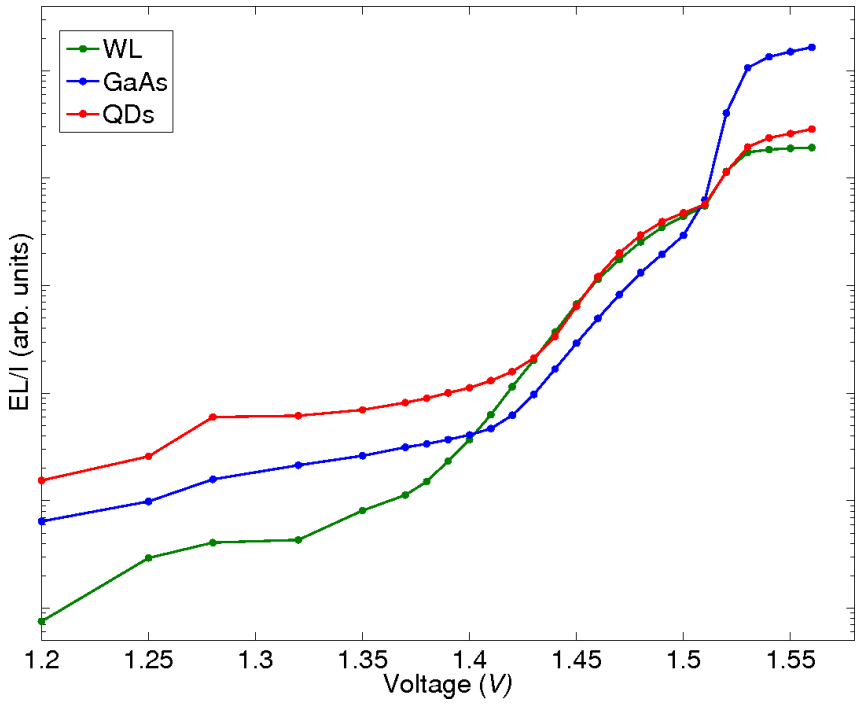

Figure 6.6: Integrated EL intensities at T=3.6K of the QDs (1.18eV-1.30eV), the WL and excited states (1.30eV-1.45eV) the GaAs (1.45eV-1.54eV) for sample B1. The data is normalised to the electrical current, I.

QDs approximately scales with I. For $V \leq$1.18V the EL intensity becomes too weak to be measured.

Whatever process is responsible for the UC, it is clear that some interactions must be taking place in order to increase the energy of the carriers. Through analysis of the EL data, it is possible to investigate the nature of these interactions. Consider the integrated area, A, of the QD EL spectrum. At a given bias, A is equal to the radiative component I_r of the electrical current I. This is given by

$$I_r(V) = e\tau^{-1} \sum_{i=1}^{N} f_i(V), \tag{6.1}$$

where, $\tau \simeq 10^{-9}$s is the radiative lifetime of an exciton in a QD [80], f_i defines the occupancy of an electron-hole pair on a particular dot, i, within the ensemble and N is the total number of dots in the device. For $V > V_{fb}$ the quantum efficiency is close to unity, which means that the recombination current is equal to the current, i.e. $I_r = I$. Using this relation the EL and $I(V)$ data can be calibrated by matching the curves at high bias [86].

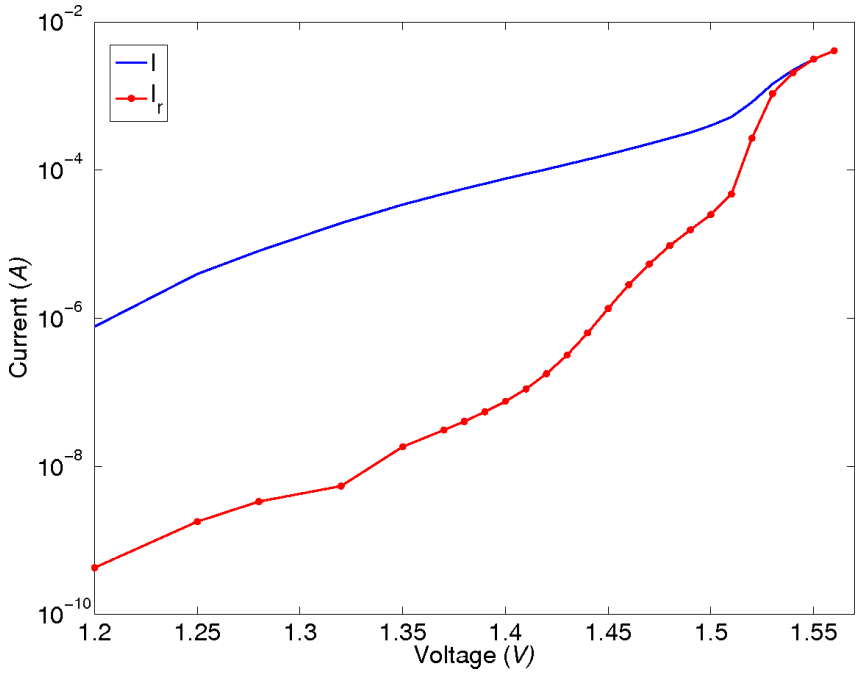

Figure 6.7: Electrical current (blue line) and recombination current (red line) plotted against the applied voltage for sample B1 at T=3.6K.

Figure 6.7 shows how I_r and I vary with V. It can clearly be seen that I_r decreases exponentially faster than I and that this decrease begins immediately as the excitation voltage drops below V_{fb}. For V=1.20V, I is 3 orders of magnitude larger than I_r, indicating the presence of strong non-radiative recombination channels at these lower biases. As discussed later these may play an important role in the UCEL.

Whilst the UCEL data presented thus far has been based on a single device from sample B1, the phenomenon has also been observed in other devices based on the same sample. The colour-scale plots for two such devices, are shown in Figures 6.8 and 6.9.

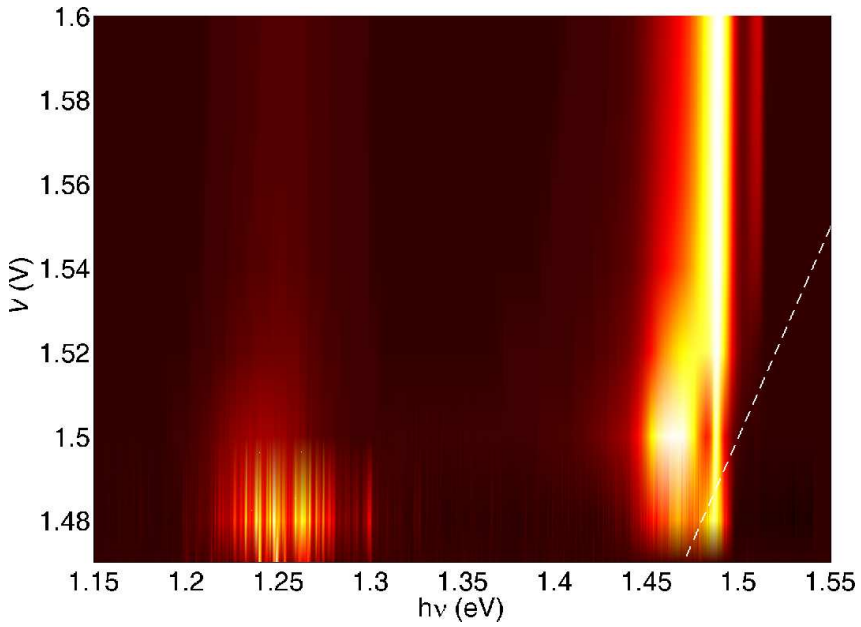

Figure 6.8: Colour-scale plot of the EL intensity vs V and $h\nu$ for a device based on sample B1 at T=3.6K. The dashed white line represents the condition $h\nu = eV$.

For these devices it was found that the currents below V_{fb} were much smaller than in that of the main device studied in this chapter and so it was not possible to measure the EL spectra down to very low voltages. It was still possible, however, to observe UCEL from these devices, as can be seen in Figures 6.8 and 6.9. While the behaviour of the devices shown is different from that of the main device studied in this chapter, the fact that they do exhibit UCEL indicates the UC is related to the fundamental physics of the sample and not a particular characteristic of an individual device.

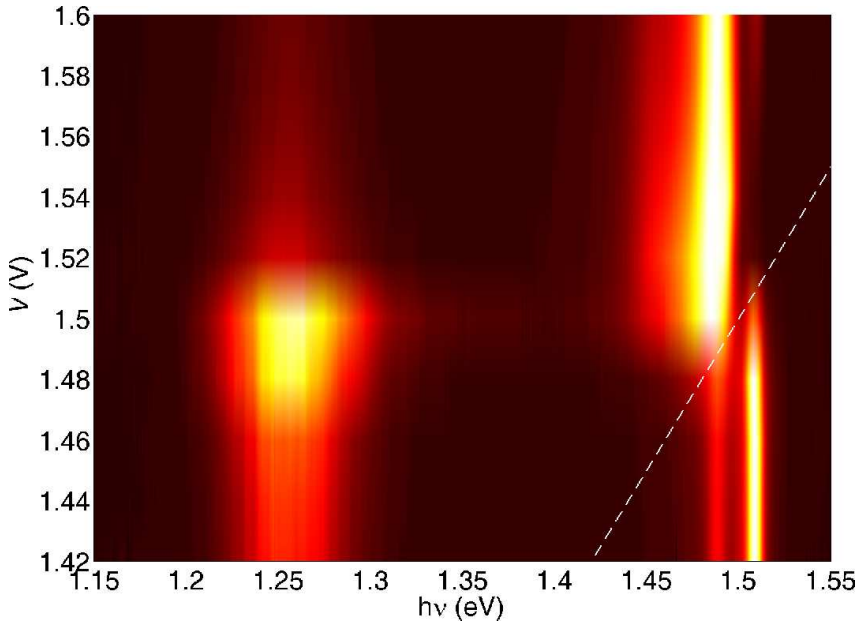

Figure 6.9: Colour-scale plot of the EL intensity vs V and $h\nu$ for a device based on sample B1 at T=3.6K. The dashed white line represents the condition $h\nu = eV$.

6.4 Dependence of UCEL on the QD density

Figure 6.10 shows EL spectra from devices based on samples A3, B3 and B4. The EL spectrum from sample B1 is included for comparison.

Although there is clearly UCEL visible in all the EL spectra shown in Figure 6.10, the intensity of the UCEL is much smaller in the B3 and B4 devices than that measured in the B1 and A3 devices. For B3 and B4, the UCEL can only be viewed when the y-axis is scaled logarthmically. Although more comparable in scale, the intensity of the UCEL in sample A3 is also markedly smaller than that of sample B1. The key difference between samples B3, B4 and A3, and sample B1, is that the QD density of sample B1 is a factor of 10 higher (n_{QD}=10^{11}cm^{-2} in sample B1 and n_{QD}=10^{10}cm^{-2} in samples B3, B4 and A3). This difference is discussed further in section 6.6.2.

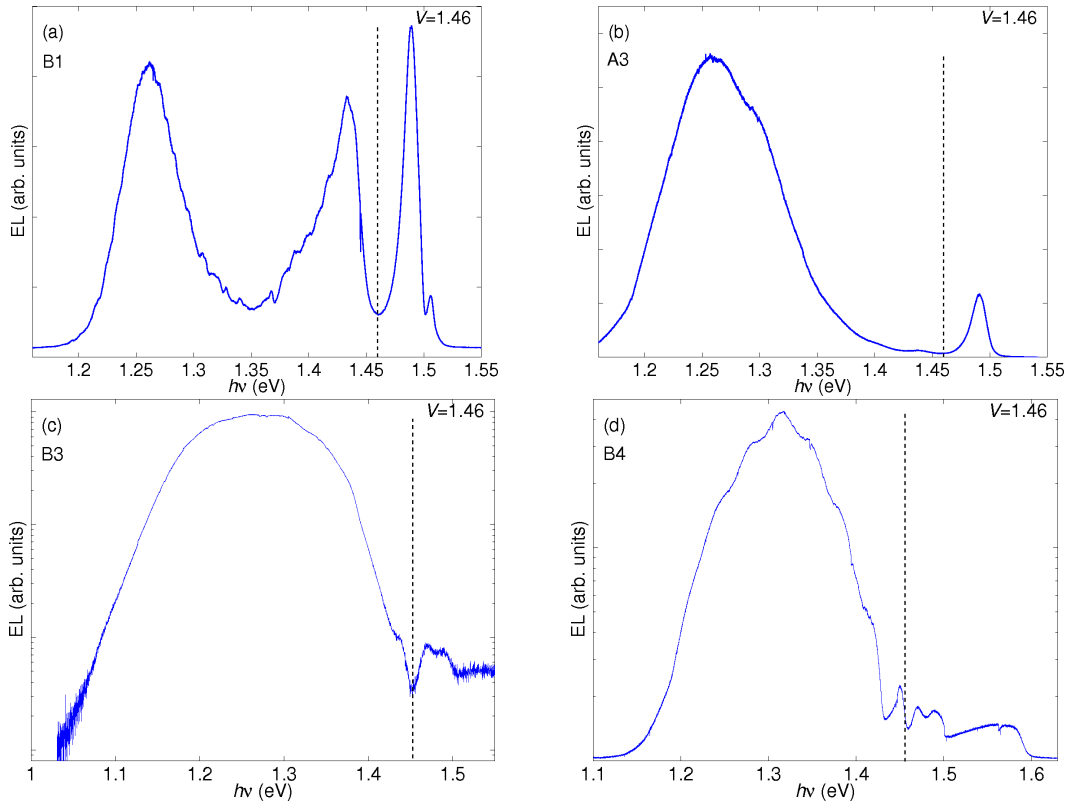

Figure 6.10: EL spectra at T=3.6K showing UCEL in devices based on samples B1 (a), A3 (b), B3 (c) and B4 (d). The y-axis is scaled linearly in (a) and (b) and logarthmically in (c) and (d). The dashed line indicates the applied bias, which is V=1.46V in all cases.

6.5 UCEL in a magnetic field

This section describes the effect of a magnetic field B, applied perpendicular to the QD plane, on the UCEL. Figure 6.11 shows a series of EL spectra at V=1.41V and different magnetic fields.

The GaAs UCEL is strongly reduced at relatively low fields, but persists up to 14 T. The B-dependence of the QD EL is much weaker. The integrated intensity of the QD and GaAs EL as a function of B at constant bias are shown in Figures 6.12 and 6.13, respectively.

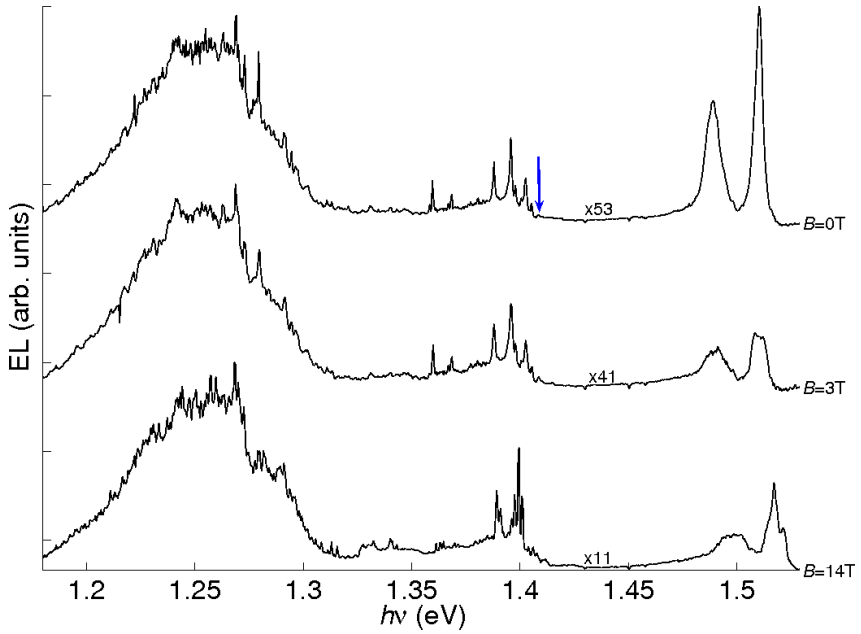

Figure 6.11: EL spectra for B=0T, 3T and 14T at V=1.41V (arrow) and T=1.8K for sample B1.

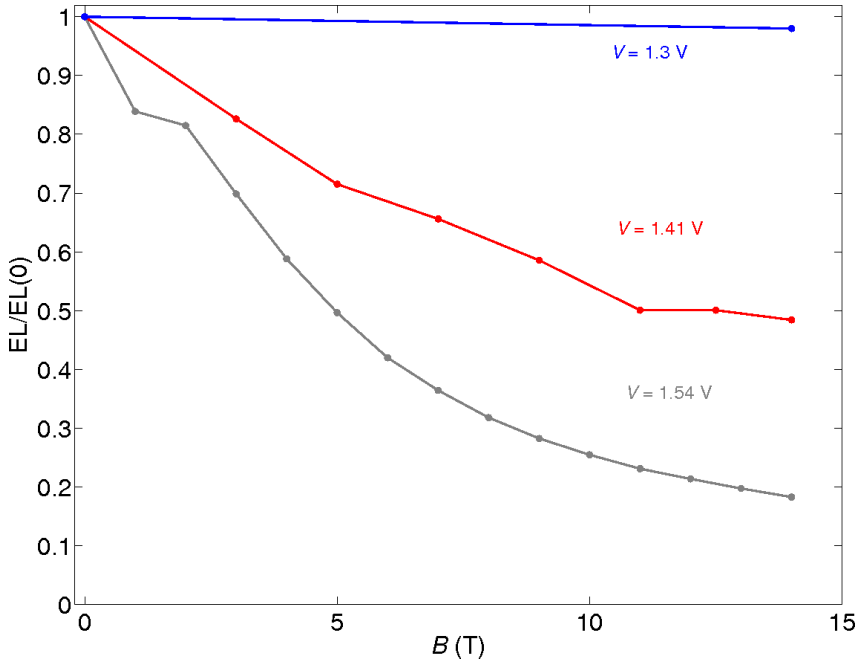

Figure 6.12: QD EL at T=1.8K as a function of B for V=1.30, 1.41 and 1.54V. Data are normalised to the value at B=0T.

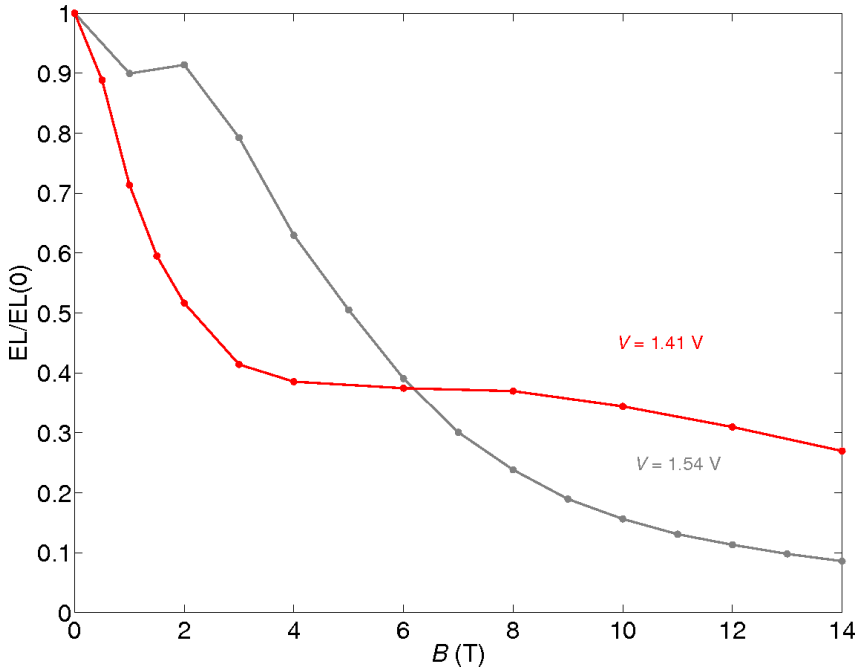

Figure 6.13: GaAs EL at T=1.8K as a function of B for V=1.41V and 1.54V. Data ares normalised to the value at B=0T. The measured GaAs intensity includes the contributions from both FE and eA^0.

For all voltages, the QD EL tends to decrease with increasing field. This dependence becomes weaker at lower bias, and at V=1.3 V the QD EL spectrum is essentially independent of B. The GaAs UCEL decreases more strongly with B than the QD emission at the same voltage and does not follow the trend of the reduced sensitivity to B with decreasing bias, which is observed for the QD EL.

6.6 Discussion

UCL is clearly a common phenomenon, having been observed in the examples cited in the introduction of this chapter as well as colloidal QDs [93] and now as UCEL in p-i-n QD diodes. Given the ubiquity of UCL and UCEL in such

a wide range of materials, devices and structures, the mechanism responsible for UC is of fundamental importance.

Three possible sources of UCL can be found in the literature: carriers can gain additional energy by phonon-assisted processes, multi-photon absorption, or Auger processes [89, 80, 94], in which an electron in a meta-stable state relaxes to lower energies by transferring the excess energy to a second electron. This process is important in technology because it opens non-radiative recombination pathways in light emitting and laser diodes and it allows fast relaxation to the ground states in QDs [95]. In particular, Auger and multi-photon processes are difficult to distinguish in PL experiments because two interacting excitons can produce the same power dependence as multi-photon absorption. The possible mechanisms for UC are discussed more in sections 6.6.1 and 6.6.2.

6.6.1 Multi-photon and phonon-assisted processes

Multi-photon and phonon-assisted processes have been shown to play an important role in the carrier dynamics of semiconductor molecules and devices [89, 96], and as such could be the cause of the observed UC. Additionally, electron-phonon interactions (polarons), can also be responsible for UC [97]. These mechanisms must be considered in terms of their ability to excite carriers from the discrete states into which they are injected to higher energy levels, within both the QD and GaAs states

The fact that the data presented here is a result of *UCEL* as opposed to UCL can immediately be used to rule out multi-photon absorption, as the device is not excited by light. Whilst the experiments were isolated from external light

sources as much as possible, there is the possibility that photons incident on the optical window of the cryostat from the background light in the laboratory could generate carriers at high energy and cause UCL. However, spectra taken with no applied bias show no emission from the sample, proving that this effect is negligible.

Phonon-assisted UC processes involve a carrier relaxation by the emission of a phonon, which then interacts with a second carrier to increase the energy of that carrier. Phonon relaxation, and consequently UC by phonon-assisted processes, suffers from the well known problem of the phonon bottleneck [98]. It has been shown that the low temperature relaxation time for an excited exciton state via LO phonon emission is ∼7.7ns, which is long compared to the radiative recombination time of 1ns for InAs QDs [80]. This means phonon assisted processed are unlikely to be the primary mechanism for UC_{QD}.

The bottleneck effect does not rule out phonon-assisted process as the mechanism behind UC_{GaAs} however. As well as the fact that UC into the continuum of GaAs states relaxes the condition on energy matching, the maximum observed UC_{GaAs} of ∼340meV is comparable to the energy of 10 LO phonons. The lifetime of a GaAs LO phonon is ∼10ps [99], meaning that multi-phonon decay processes are efficient compared to radiative recombination. Indeed, a 3 LO phonon relaxation has previously been observed in PL studies on InAs QDs [100].

If the UC_{GaAs} process is phonon driven then it would be expected, given the relatively large number of phonons required to up-convert a single carrier up to 340meV in energy, that the efficiency of the process would increase with

temperature, when more phonons would be available to facilitate the UC. Figure 6.14 shows the temperature of the EL for sample B1.

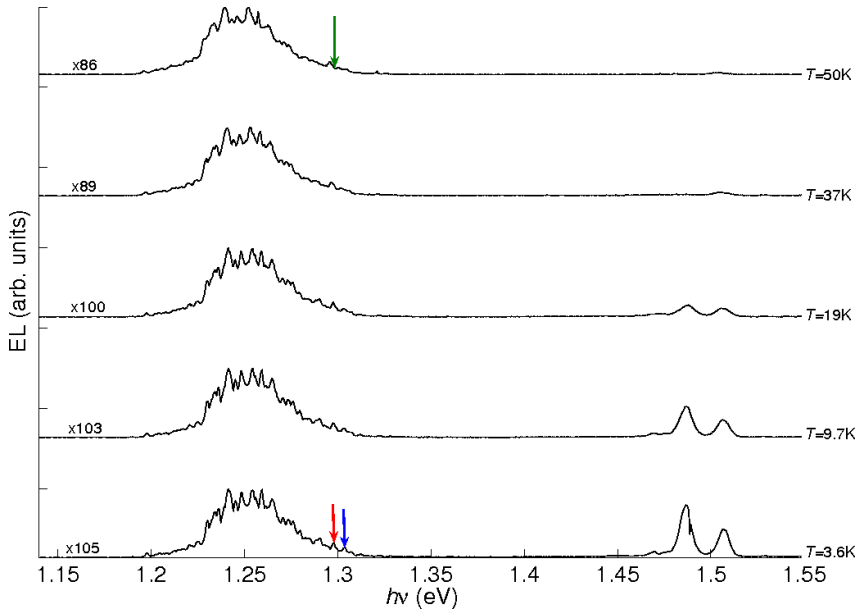

Figure 6.14: EL spectra of sample B1 at different temperatures. The applied bias is V=1.30V, as indicated by the green arrow. The blue and red arrows highlight two specific peaks that are discussed in the text.

It is immediately apparent that the intensity of the peaks associated with UC_{GaAs} decreases with increasing temperature, contrary to what is expected if the UC process is facilitated by phonons. The intensity of the QD emission band quenches only very slowly with temperature in good agreement with previous studies on InAs QDs [101]. Additionally, the emission peak at $h\nu$=1.304eV in Figure 6.14 (blue arrow), which results from UC_{QD}, can be seen to decrease in intensity much faster than the peak at $h\nu$=1.298eV (red arrow), which is from standard EL emission.

Analysis of the change in intensity shows that the GaAs peak decreases by 94% between T=3.6 and 50K, whilst the eA^0 is almost completely quenched. The QD peaks at $h\nu$=1.304eV and $h\nu$=1.298eV lose 73% and 26% of their intensity,

respectively. However, the background QD emission quenches by 16% with the increased temperature and this must be taken into account, meaning that the $h\nu$=1.304eV peak decreases by 57% above the background decrease, and that the $h\nu$=1.298eV peak decreases by 10%.

The decrease in UC_{GaAs} is a clear indication that the UC process is not facilitated by phonon-assisted relaxation. Furthermore, the way the UC_{QD} is also quenched with temperature is an indication that it is fueled by the same process as the UC_{GaAs} and, as has already been stated, phonons are not a feasible mechanism for relaxation within the QD band. It follows from this discussion that phonon-assisted relaxation can probably be discounted as the principle mechanism behind UC.

Similarly, whilst it has been shown that polaron decay can circumvent the phonon bottleneck [102], this cannot be responsible for the UC as it does not explain the strong temperature-induced quenching of the UCEL shown in Figure 6.14.

6.6.2 Up-conversion carrier dynamics

Having ruled out multi-photon and phonon-assisted processes, Auger processes remain as a possible mechanism for UC. The observed scaling of the UCEL with the QD EL (Figure 6.6) indicates that the mechanism responsible for the UC is non-radiative Auger recombination. In this process, an electron and a hole in their respective QD ground states recombine and the released energy excites a second electron (or hole) on the same, or an adjacent, QD into the conduction (or valence) band of the GaAs, with the energy being transferred

via the Coulomb interaction [34], see Figure 6.15. Subsequent recombination, on a time scale shorter than that required to sweep carriers out of the intrinsic region, then leads to luminescence from states near the GaAs band edge. This *"Auger fountain"* [103] process is mediated by the Coulomb interaction of the three particles. A more symmetric mechanism with two interacting excitons is also possible. Although the up-converted carrier would gain much more energy from the proposed Auger process than it needs to obtain even the highest level of observed UC, this does not constrain the mechanism. As long as the carrier receives enough energy to reach the GaAs states, then any excess energy can be shed through thermalisation with the lattice before recombination.

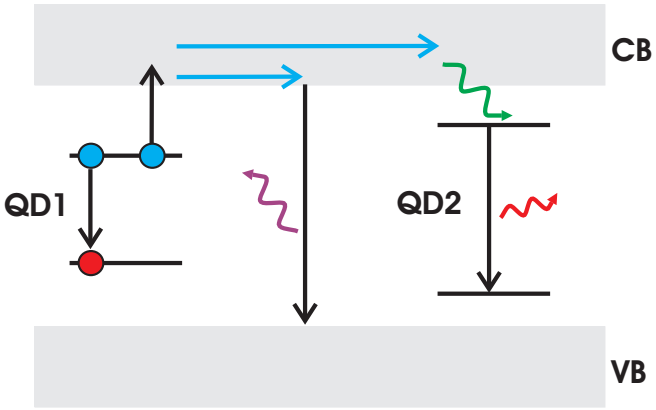

Figure 6.15: Schematic diagram of the described Auger UC and carrier redistribution process.

Auger electron relaxation times at cryogenic temperatures have been measured at 1-8ps [95, 104], making Auger UC an efficient mechanism for carrier redistribution in the QD ensemble. The up-converted carriers can diffuse through the structure and be captured by other QDs. This redistribution explains the UCEL from QDs for V<1.3 V. It could also account for the carrier thermalization between non-resonantly excited QDs observed at low T, resulting in a Stokes shift between the absorption and emission spectra [105]. Experiments

suggest that Auger processes are more efficient in samples with a high density of small QDs [86] due to the smaller inter-dot spacing and the lower energy gap between the first excited QD state and WL [106]. Thus the data shown in Figure 6.10 support Auger processes being the mechanism responsible for UC as it can clearly be seen that there is a correlation between the QD density and the strength of the UCEL.

Figure 6.16 shows how the un-normalised intensity of the UC signal varies with temperature.

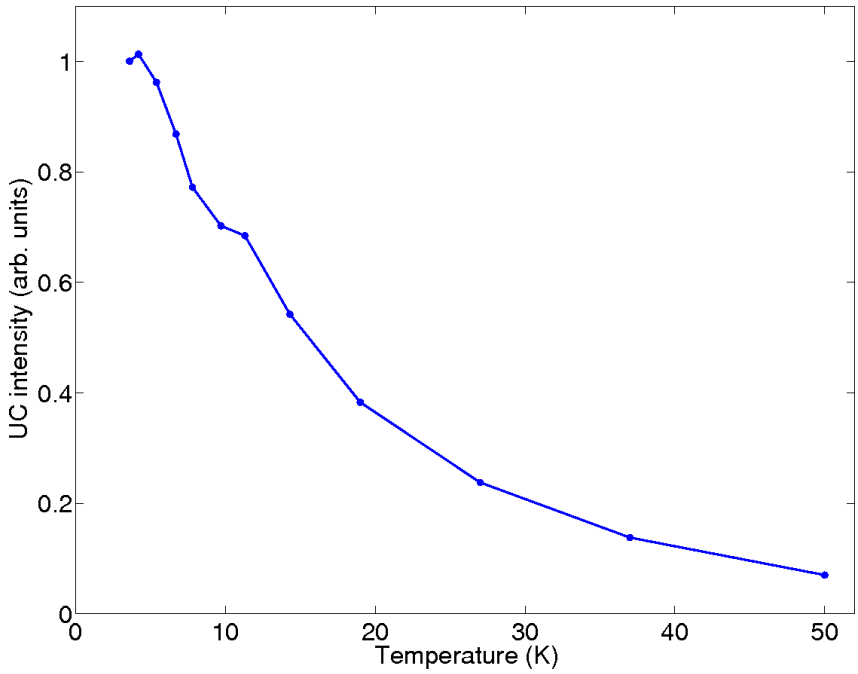

Figure 6.16: Total UC intensity versus temperature for sample B1 with V=1.30V. UC data are normalised to the value of the UC intensity at T=3.6K

The Auger rate is expected to decrease with increasing temperature due to the depopulation of holes from the QD ground states from thermal excitation [107]. Whilst the UC intensity shown in Figure 6.16 does decay with increasing temperature, it does so on a faster scale than could be attributed to thermal depopulation as the thermal energy of carriers at 50K is only $k_B T$=4meV. The

observed temperature dependence here is more likely due to thermal escape of the carriers from the GaAs *after* UC, into non-radiative recombination centers, and/or ionisation of the acceptor and donor states. This is supported by the fast decay of the eA^0 peak discussed in section 6.6.1.

When considering the B-dependence of the UCEL, it is noted that a reduction of the QD PL intensity with B has been previously attributed to the field-induced localization of carriers in potential fluctuations of the WL, leading to a reduced probability of carriers being captured into the QDs [108]. The behaviour of the UCEL in a magnetic field, shown in section 6.5, could be due to a similar mechanism in the GaAs layers. Localization of carriers may take place at impurities or minima of the disordered potential created by the InAs layer. At lower biases, the QDs are populated directly by carriers tunneling resonantly into the zero dimensional states. This process depends only weakly on B and leads to the weak sensitivity of the QD EL to B at lower bias. At low bias, tunneling is likely to be the rate-limiting process, which may mask the effects of the increased exciton oscillator strength in a magnetic field. Because of the strong confinement, the carrier wave functions in the QDs are only weakly affected by the magnetic fields considered in our experiments (B up to 14T). This suggests that the quenching of the UCEL by B is mainly controlled by the carrier dynamics above (below) the conduction (valence) band edges in the GaAs and not by the Auger UC process.

The ability to excite carriers into the GaAs conduction band whilst in a resonant injection regime leads to the novel concept of UCEL spectroscopy, which is discussed in the following section.

6.6.3 UCEL Spectroscopy

Above V_{fb}, carriers from the contact either traverse the intrinsic region and recombine with majority carriers in the opposite GaAs contact layer, or they are trapped by the QDs and recombine from the ground states by emitting light at lower energies. Below V_{fb}, however, free carriers are resonantly injected into the QD states from the GaAs. The observed UCEL therefore must mainly originate from recombination near the position of exciton generation, i.e. in the intrinsic GaAs region surrounding the QDs. UCEL therefore provides spectroscopic access to the GaAs matrix and the defects surrounding the QDs. From the widths of the UCEL emission, the depths of the GaAs potential fluctuations can be deduced. A tentative model is that the fluctuations can give rise to a continuum-like band of states in the GaAs, which are then observed in the EL, as shown schematically in Figure 6.17.

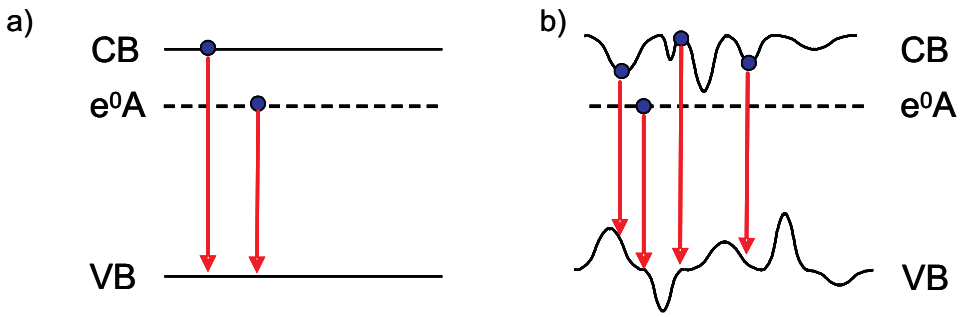

Figure 6.17: Schematic diagram showing how fluctuations, for example due to strain, alloying or dopant segregation, in the GaAs band-gap energy can lead to a broadened EL emission. The three levels shown are the conduction band, neutral electron-acceptor and valence band. Figure (a) corresponds to a system with no disorder and figure (b) to a system with a high level of disorder.

If the system has a low level of disorder as in Figure 6.17(a), then the GaAs states are essentially unperturbed. However, in the highly perturbed case shown in Figure 6.17(b), the perturbation of the conduction and valence bands

gives rise to fluctuations in the band-gap energy. These fluctuations will cause a broadened energy distribution of the exciton states, which has observed in EL as shown in Figure 6.18.

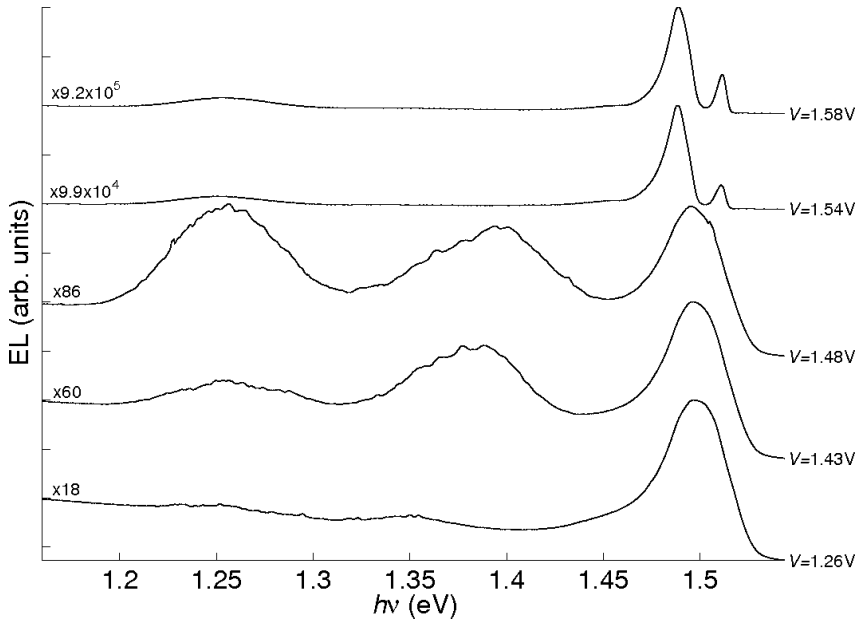

Figure 6.18: EL spectra of a device based on sample B1 at T=3.6K. The applied voltage for each curve is given on the right hand side. The curves have been normalised to the maximum peak height and offset for clarity.

6.7 Conclusion

The phenomenon of UCEL has been demonstrated in a number of p-i-n diode devices containing self-assembled InAs QDs. To the best of our knowledge, this is the first time that UC in QDs has been reported by electrical injection of carriers rather than by photo-generation of carriers. Two distinct types of UCEL have been observed: from low to high energy states within the QD band and from low energy states to the GaAs conduction band. This second type of UC has led to a UCEL being observed at an energy of ∼340meV in excess

of that provided by the applied voltage. The data presented in this chapter supports the idea that the underlying UC mechanism is non-radiative Auger recombination of electron-hole pairs in QD ground states. The observation of QD UCEL at low voltages and the magnetic field dependence suggests that the diffusion of the up-converted carriers in the GaAs is important for the carrier redistribution and thermalization in the QD ensemble. UCEL provides a useful probe for investigating carrier dynamics in LED structures and can shed light on the relaxation mechanisms and carrier-carrier interactions in QDs.

The ability to probe the GaAs close to the QDs using UCEL suggests the development of the novel concept of UCEL spectroscopy, which could be a useful tool for measuring the level of disorder in the GaAs surrounding the QDs in the intrinsic region of a device.

Part of this work has been published in *Applied Physics Letters* [109].

Chapter 7

Magnetic field experiments

7.1 Introduction

Having established in Chapter 4 that it is possible to resonantly inject carriers into the QD ground state and to observe EL from the dots, an investigation into the effect of a magnetic field on the tunneling processes and optical properties of sample A3 was carried out.

Magnetotunneling spectroscopy (MTS) is a non-destructive and non-invasive technique for probing the electron wave function of a QD [79]. MTS has been used elsewhere to study the electronic properties of semiconductor heterostructures, for example to image the probability density of the electron wave-function in k-space [110]. Applying the magnetic field perpendicular to the growth plane (z) causes an increase in the momentum of a tunneling electron in the xy plane. The magnitude of the additional in-plane momentum is given by $k_B = \frac{eBs}{\hbar}$, where B is the magnetic field and s is the tunnel distance

between the emitter and the QD. For this process the tunnel matrix element M is expressed in terms of the Fourier transforms of the real-space wave functions such that $M = \int_k \phi_i(k - k_\beta)\phi_f(k)dk$, where the subscripts refer to the initial (emitter, E) and final (QD) state. The tunnel current is then given by $I \sim |M|^2$. In real-space, the initial emitter state has a relatively weak spatial confinement, hence in k space $\phi_E(k - k_\beta)$ is a sharply peaked function with a finite value only close to $k = k_\beta$. Conversely, the QD state is strongly confined in real-space so that $\phi_{QD}(k)$ is spread over a broad range of k. The narrow spread for $\phi_E(k - k_\beta)$ relative to $\phi_{QD}(k)$ thus allows the form of $\phi_{QD}(k)$ to be determined by varying B, as shown in Figure 7.1. In the ideal case, $\phi_E(k - k_\beta)$ can be approximated as a δ function and then $M(k_\beta)$ is equal to $\phi_{QD}(k)$. A more detailed description of the MTS model is given in the appendix A.

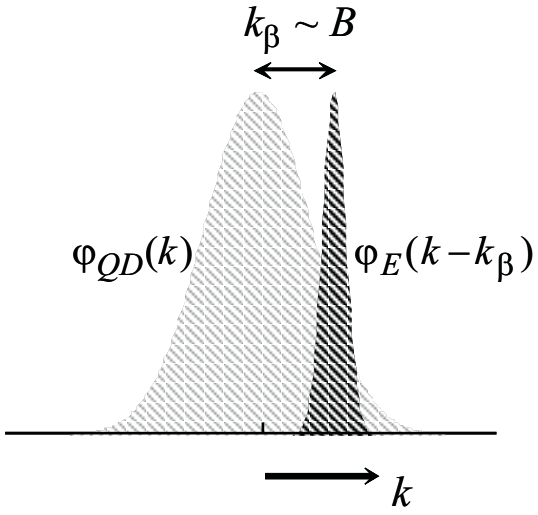

Figure 7.1: Overlap between $\phi_E(k - k_\beta)$ and $\phi_{QD}(k)$, the Fourier transforms associated with the electron wave-function in the emitter and quantum dot, respectively, at a given magnetic field. Figure taken from [79].

7.2 Current-voltage characteristics in a magnetic field

Magnetic field studies on sample A3 were performed in fields up to B=14T. The magnetic field was applied perpendicular to the growth plane of the QDs. Figure 7.2 shows $I(V)$ curves for sample A3 taken at 0T, 6T and 14T.

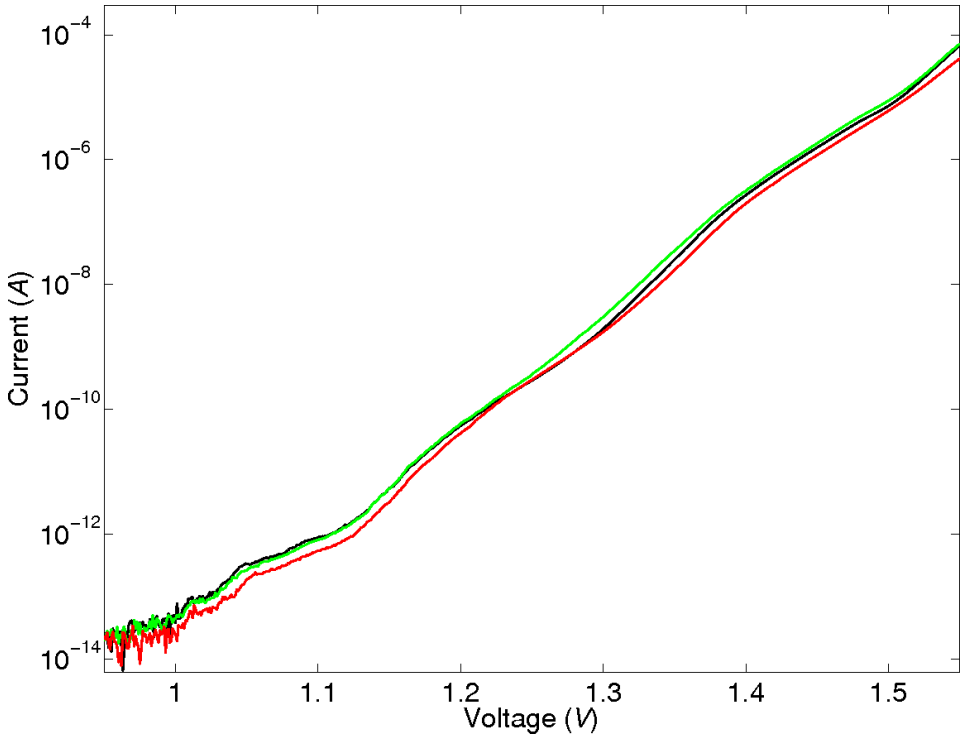

Figure 7.2: Magneto-$I(V)$s for sample A3 at T=1.8K. Curves are shown for B=0T (black), 6T (green) and 14T (red).

It is immediately clear that the B-field has an effect on the $I(V)$. It can also be seen that the current variations caused by the B-field vary with applied bias. In Figure 7.3, the $I(V)$ data for sample A3 is shown again, but with an exponential fit, I_f=$Ae^{\beta V}$, subtracted from the $I(V)$, and normalized to I_f.

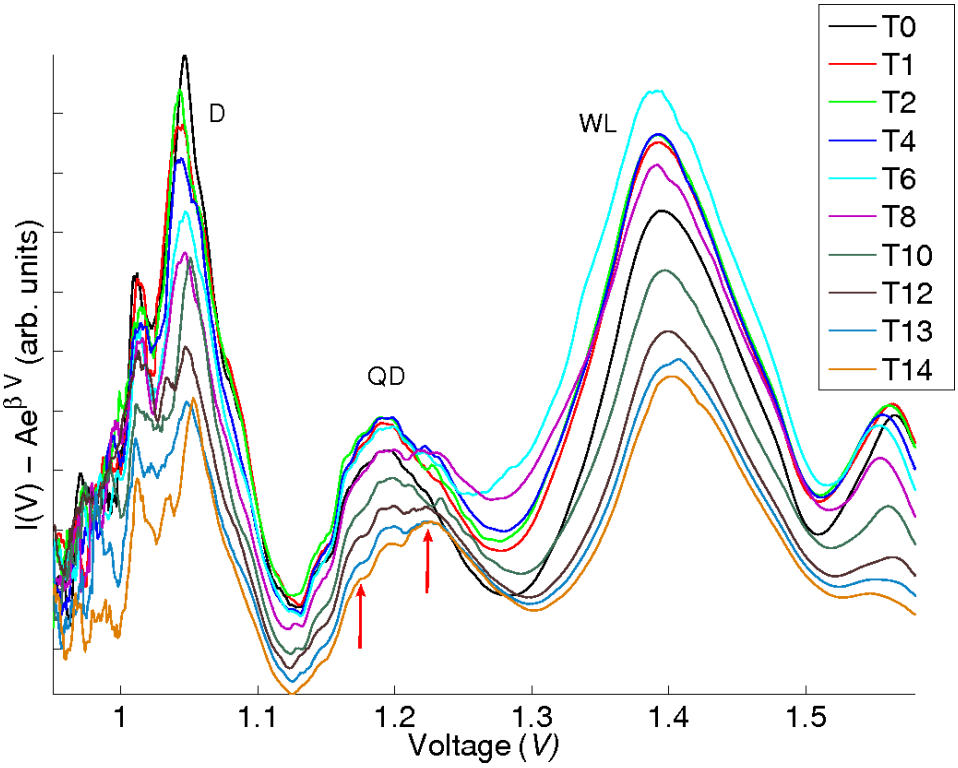

Figure 7.3: $I(V)$ data for sample A3 shown with an exponential fit to the current subtracted and then subsequently scaled by the fitted current. Curves are shown for B=0-14T at the fields indicated by the legend. The red arrows highlight two specific peaks, which are discussed in the text.

The three regions of increased current flow discussed in Section 4.2, due to defect states (D), QDs and the WL, are immediately obvious in Figure 7.3 and it is also clear that the magnetic field has a different effect in each area. The defect band, D, at V∼1.05V, is diminished by a B-field of only 1T. There is a slight anomaly in the data, in that the D band is more strongly suppressed at 1T than 2T. However, the general trend is clearly an increasing suppression of the current with increasing field. The QD band, centered on V∼1.19V, has both a different shape and B-dependence than the lower energy band. The intensity initially increases with increasing B. The 2T and 4T curves overlap at the maximum point, indicating that the true maximum probably occurs at

3T. Past this point, the band is suppressed by the increasing field such that at 8T the intensity is back to its 0T value and at 14T the intensity of the central point of the band is ∼50% of its 0T value. In addition to its effect on the intensity of the band, the increasing B-field causes the emergence of peaks in the $I(V)$ at V=1.175V and 1.225V, highlighted by red arrows in Figure 7.3. Both peaks are actually present at B=0T, but become much more pronounced at higher fields. The effect appears to be due to the band being more suppressed at lower biases than higher ones. The WL band, centered on V∼1.39V, is much broader than the other two and has a distinctive bell-shape. This band increases with increasing B-field, up to 6T, before starting to be suppressed so that at 14T it is at ∼60% of its 0T value.

7.3 Magnetotunneling spectroscopy

Having gathered data on the behaviour of sample A3 in a magnetic field, the MTS technique was used to study the behaviour of the QD band. The experimental data is determined by the variation of peak height in Figure 7.3 with magnetic field at V=1.18V, and is presented scaled to its 0T value, see Figure 7.4. The experimental error values arise from the process of subtracting the exponential fit to the $I(V)$ data used to create Figure 7.3. Due to the limitations of the equipment, the maximum B-field used was 14T, however this was still sufficient to reduce the peak height to ∼40% of its original value.

In order to apply the MTS technique, the carrier confinement in the QD along a given direction, z, was modeled by a one-dimensional harmonic oscillator. This gives the form of the ground state wave-function in z and k space:

$$\Psi(z) \sim exp\left[\frac{-z^2}{2l_c^2}\right] \tag{7.1}$$

$$\Psi(k) \sim exp\left[\frac{-l_c^2 k^2}{2}\right] \tag{7.2}$$

where w_0 is the angular frequency of the harmonic motion corresponding to a confinement length l_c=$\sqrt{\frac{\hbar}{m^* w_0}}$ and confinement energy E_c=$\hbar w_0$ [79]. Replacing k with k_β=$\frac{eBs}{\hbar}$ in equation 7.2 gives

$$\Psi(k) \sim exp\left[\frac{-e^2B^2s^2}{2\hbar m^* w_0}\right] = exp\left[\frac{-e^2B^2s^2l_c^2}{2\hbar^2}\right]. \tag{7.3}$$

The probability density of the wave-function can then be expressed as

$$|\Psi(k)|^2 \sim exp\left[\frac{-e^2B^2s^2l_c^2}{\hbar^2}\right]. \tag{7.4}$$

This allows the model to be expressed in terms of just two fitting parameters, the tunnel distance, s, and the confinement length l_c. From the growth sheet a value for s of 11.6nm is determined. Having fixed s, l_c can be used as the variable fitting parameter in order to get a good match with the experimental data. The form of the experimental data shown in Figure 7.4 maps out the general trend discussed in section 7.2.

An initial increase in the intensity for fields of up to 3T is followed by a steady decrease in intensity at higher fields. The theoretical fit to this data, shown in red, shows a reasonable agreement with the data for higher magnetic fields, however it fails to match the initial increase in intensity. Using the discussed

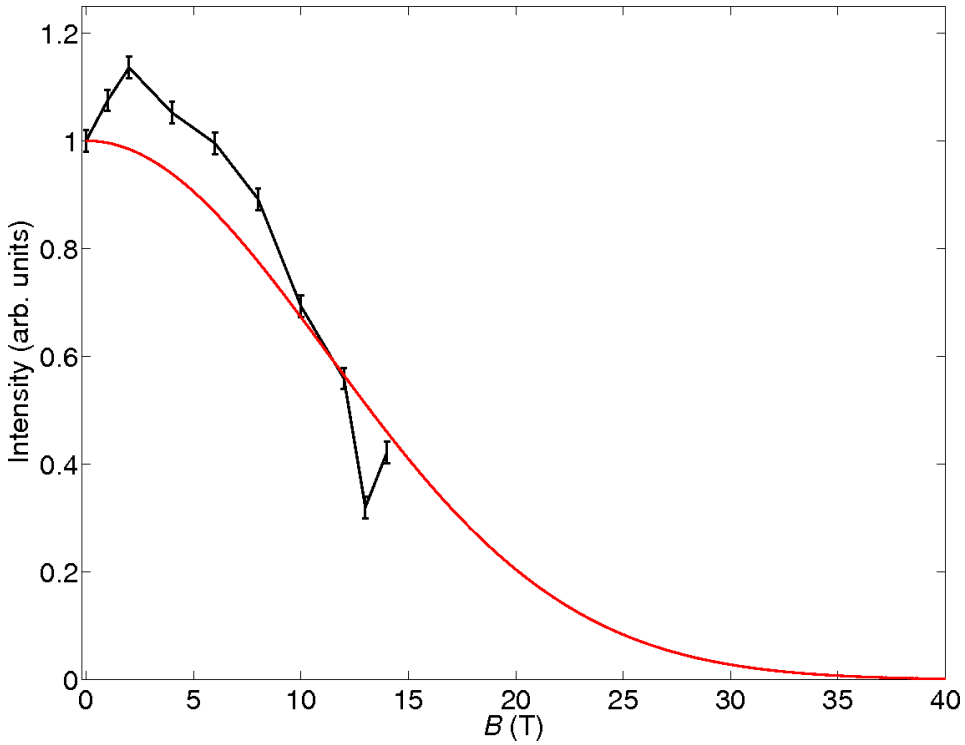

Figure 7.4: MTS data for sample A3. The experimental data is shown in black and is scaled to its value at B=0T. The theoretical fit for the probability density of an electron in the ground state produced by the MTS model is shown in red with prefactors omitted.

fitting scheme with s=11.6nm gives a confinement length, l_c=2.53nm, which corresponds to a confinement energy of 173meV, taking m^* as $0.068m_e$. This is clearly unfeasible as it is much larger than the separation of 55meV between the ground and excited states of the QD observed in EL. An alternative approach to modeling the experimental data is to use the data gathered in Chapter 4 to determine l_c and then to very s in order to produce a good fit. Using the experimental value of 55meV as the confinement energy gives a value for l_c of 4.54nm and s can now be varied to produce the fit shown in Figure 7.5.

The theoretical curves in Figure 7.5 correspond to a value of s=7nm. This is obviously less than the 11.6nm separation between the doped n-layer and

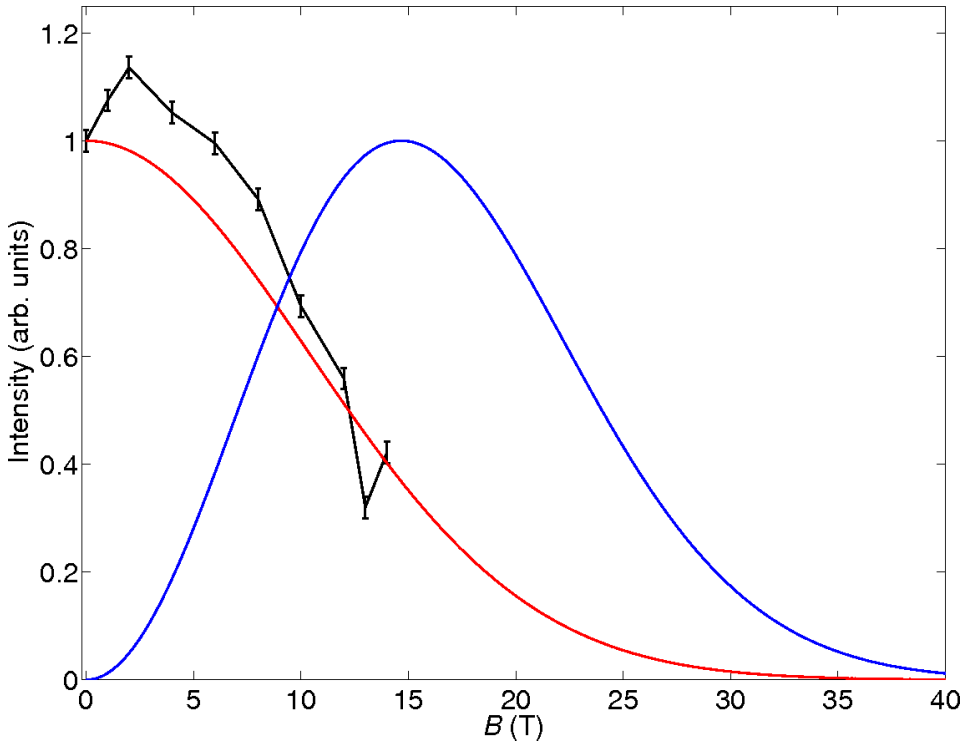

Figure 7.5: MTS data for sample A3. The experimental data is shown in black and is scaled to its value at B=0T. The theoretical fit for the probability density of an electron in the ground state produced by the MTS model is shown in red with prefactors omitted. The blue curve is the theoretical fit for the first excited electron state, normalized to its peak.

the QDs derived from the growth sheet. The reduced tunnel distance needed to produce the fit can be explained by moving away from considering the growth layers of the structure as having ideal, flat potential interfaces. The available transport channels from the heavily doped n-layer to the QDs will be strongly influenced by diffusion of dopants and segregation of indium into the nominally undoped GaAs layer, creating fluctuations in the local dopant density and providing additional carrier states and/or causing strain in the lattice. These fluctuations can create finger-like protrusions extending out from the electron "Fermi-sea" towards the QD layer [79]. These protrusions mean that the tunnel distance for some carriers can be significantly less than that

inferred from the growth sheet. Since the tunnel current depends exponentially on the tunnel distance, then the carriers tunneling from these "fingers" will make a disproportionately large contribution to the transport dynamics of the system. With this being the case, then it is understandable that the data could indicate an effective tunnel distance significantly lower than would otherwise be expected.

The excited state derived from using s=7nm and l_c=4.54nm is shown in Figure 7.5. As can be seen the model predicts a peak due to the excited state a $B\sim$14T, which is not observed in the experimental data. There are a number of possible reasons why this is the case; the transfer matrix element discussed in appendix A, which has a B-dependence independent of the tunnel matrix element, has been neglected in this model. The data indicate that there are ground and excited states of both electrons and holes within the region of interest, which could affect the ability of the model to accurately match the experimental data. The presence of the fingers in the potential could mean that carriers are tunneling from both ground and excited states within the emitter, confusing the B-field dependence. A preliminary investigation of sample A3 in the high-field facility in the Institute for Metallic Materials at IFW Dresden, which allowed measurements to be made in pulsed magnetic fields of up to 47T, with a current resolution of 1nA, was performed. The data shown in Figure 7.6 are derived from subtracting an exponential fit from the $I(V)$ in the same way described in section 7.2. In this case the intensity is taken as being the integrated area of the entire QD band rather than the maximum peak height.

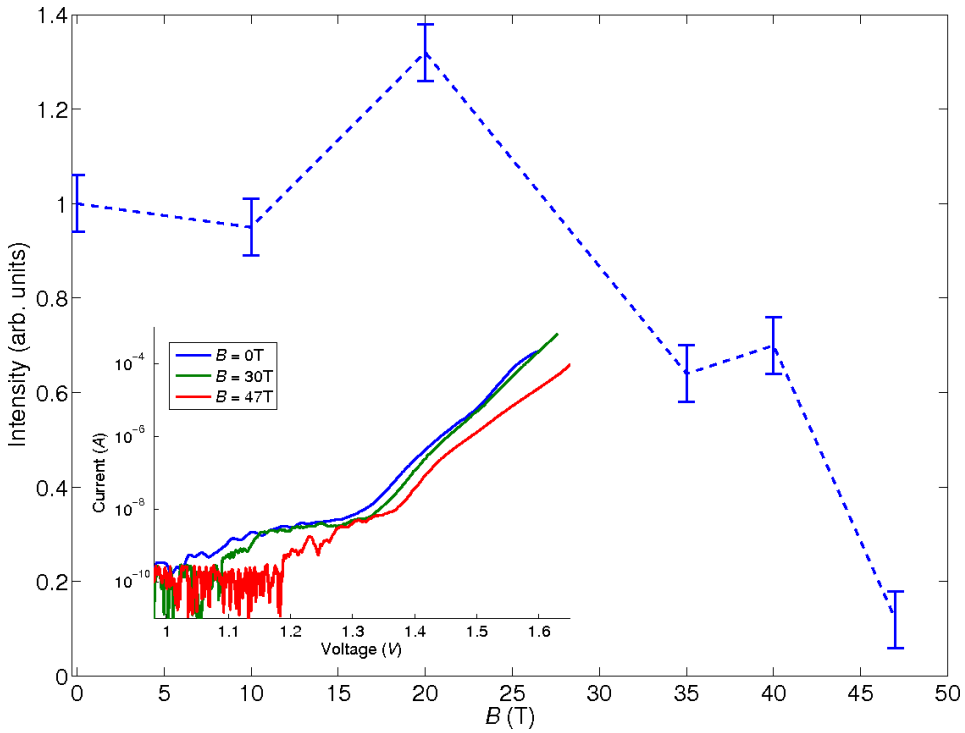

Figure 7.6: High magnetic field data for sample A3. Plot shows integrated intensity of the QD band in $I(V)$ versus magnetic field. The inset shows the I(V) curves for B=0T, 30T and 47T.

Although the data has far less points than is desirable, there is the suggestion of an excited state at $B\sim$19T, which is reasonably close to the 14T suggested by the MTS model. Whilst this is in no way conclusive, it does lend support to the analysis above and warrants further investigation.

7.4 Conclusion

The attempt to use MTS to map the QD electron ground state wave-function for sample A3 has shown that in order to obtain a good fit to the experimental data an emitter-QD tunnel distance of 7nm must be used. This is significantly less than the nominal tunnel distance given by the growth sheet. This supports

the idea that fingers in the potential profile of the emitter play a significant role in the carrier dynamics of the samples. The high-magnetic field study, although only preliminary, shows the suggestion of the first excited electron state. A good pathway for future work in this area would be a more detailed MTS study at high magnetic fields in order to improve upon the wave-function mapping presented here.

Chapter 8

Conclusion and future prospects

In this thesis it has been shown, using transport and optical studies on a series of samples, that it is possible to achieve bipolar resonant injection of carriers into the zero-dimensional states of InAs SAQDs situated in the intrinsic region of a p-i-n RTD. This concept has been used to demonstrate single QD emission from a large ensemble of QDs, without using advanced processing techniques. This is advantageous as, in order for QD based devices to be suitable for applications, they should be as simple to fabricate as possible. Single-line emission has been observed in broad-scale measurements of the whole mesa surface and subsequent analysis has shown that, at the lowest biases for which EL was still visible, the single remaining EL emission line was due to approximately 3 QDs. Single-line emission with a FWHM of 0.2meV, which shows good agreement with single QD emission linewidths reported in the literature, has been observed using μEL measurements. These experiments are sensitive to the frequency of the emitted light and showed that the single-line emission was only present at very specific energies, which is characteristic

of emission from the discrete energy levels present in QDs. This single-line emission has been observed in a number of different samples, indicating that selecting a single QD from a large ensemble can be achieved using a range of sample designs. This improves the suitability of this process for use in applications. Photon correlation measurements were attempted using the μEL set-up. However, the signal intensity was just below that required to be able to successfully perform these measurements. This opens up the next logical step in this work, which should be to design a sample with a higher current in the resonant injection regime, for example by using a thinner intrinsic region. This higher current should result in a more intense EL signal which would then allow photon correlation measurements to be performed.

Analysis of the data taken during the study into single QD emission, specifically comparing the deviation between the observed and expected behaviour of the samples, combined with a magnetic field study of the transport dynamics, has indicated that fluctuations in the emitter potential profile have a significant effect on the optical and electrical properties of the samples. Spatially inhomogeneous EL emission and the preferential selection of some QDs are attributed to the variations in emitter-QD tunnel distance across the sample caused by "fingers" in the potential profile. Modeling has shown that these fingers could cause the emitter-QD tunnel distance to be significantly shorter than the nominal tunnel distance given by the growth sheet. Proving this assertion is technically challenging. It will be difficult to precisely control the formation of these fingers in order to produce a systematic series of samples, especially as the exact origin of these fingers has yet to be determined. Although it is suggested here that the most likely cause is diffusion of dopants, it is also possible that the disorder that causes these fingers is introduced to the

system through the contacting of the sample. If this is the case then it may be possible to produce a series of samples, all contacted in slightly different ways, that would allow this phenomenon to be investigated. However, it is not clear that these two effects would be separate and distinguishable in terms of the effect they had on the apparent tunnel distance, making the analysis complex. It is clear that, if these fingers have such an important influence on the behaviour of the sample, they should be investigated further. The next step could be to produce a set of samples in which the effects of temperature dependent dopant diffusion and contacting variations are investigated. However, this would probably only serve to increase knowledge of the possible causes of these fingers, rather than provide conclusive evidence as to the origin of the fingers.

Evidence of UCEL has been provided for a sample containing an InGaAs QW and also for various samples containing InAs QDs. UCEL of up to ∼340meV, to the best of our knowledge the largest level of UC observed in QD semiconductor devices, has been reported. This is also the first time that UC in QDs has been reported by electrical injection of carriers rather than by photogeneration of carriers. The principle mechanism responsible for up-conversion has been shown to be non-radiative Auger recombination of electron-hole pairs in QD ground states. This attribution is reached as it is shown that multi-photon and phonon assisted processes, the other possible causation mechanisms discussed in the literature, cannot be responsible for the UC. The electrical injection of carriers rules out multi-photon processes. Phonon assisted processes are discounted as the intensity of the UCEL is reduced by increasing temperature and the high level of UCEL observed (∼340meV) means that a large number of phonons would be required to UC each carrier, making

this mechanism improbable. Auger processes are suggested as the observed temperature and QD-density dependence of the UCEL agrees with the dependencies reported for Auger processes in the literature. Additionally, there is an observed correlation between the level of non-radiative recombination taking place in the sample and the level of UC. As Auger processes are an efficient mechanism for non-radiative energy transfer between carriers this is further supporting evidence that Auger processes are the mechanism responsible for UC.

There are a number of avenues for the continuation and development of the work presented in this thesis. As part of the probe into the potential fluctuations, the MTS study presented in section 7.2 could be improved and expanded upon. In order to perform the high magnetic field experiments, which have a current resolution of 1nA, a new sample, with a higher current in the resonant injection regime, would need to be grown in order to obtain clearer results. Given the flexibility of sample design that can achieve bipolar resonant injection this should be possible. This should allow a detailed series of measurements to be performed at fields between 0 and 47T, which should allow a significantly more accurate map of the probability density of the electron wave-function than that presented in Chapter 7, to be obtained. However, this process would still be difficult due to complications arising from having both electrons and holes present in the structure, and indeed, electron-hole pairs. This would make the physics of developing the process of interest in itself.

The novel concept of UCEL spectroscopy proposed in section 6.7 could also be a useful tool in this study due to its ability to probe the quality of the GaAs immediately surrounding the QDs. This is potentially an area of significant

interest as the high strain experienced by the GaAs near to the QD layers should mean that carriers in this region behave differently from those in the bulk GaAs. In most studies, however, no distinction is made between the bulk and near-QD GaAs. UCEL spectroscopy could provide a useful tool to improve our understanding of the potential effects on carrier behaviour in these regions.

The work into bipolar resonant injection of carriers presented in this thesis could also be combined with the work being carried out by other members of the University of Nottingham on injecting spin polarised carriers into p-i-n RTDs [111]. In this work a layer of gallium manganese arsenide is used to generate spin polarised holes in a RTD structure. Although it is possible to inject spin polarised carriers into the QW contained within the structure, a significant number of carriers experience decoherence within the bound states, resulting in a loss of polarisation. By combining this work with the bipolar resonant injection presented here, it should be possible to inject spin polarised carriers into QD states. This should result in a much lower level of decoherence and would allow spin polarised light emission from the QDs, leading to the possibility of developing a device suitable for applications in the field of quantum information processing.

Appendix A

Magnetotunneling spectroscopy

MTS can be described theoretically using the Bardeen transfer matrix method, in which the overall system can be separated into three subsystems, each with an associated Hamiltonian, $\hat{H}_s$, where the subscript refers to either the emitter (E), a quantum dot (QD), or collector (c). The tunneling probability between the emitter and QD states is given by $I \sim |MT|^2$, where M is the tunneling matrix element and T is the Bardeen transfer matrix element [112]. The matrix elements are given by:

$$M = \int_{-\infty}^{+\infty} \varphi_{QD}^{*}(x,y)\varphi_{E}(x,y)dxdy \tag{A.1}$$

$$T = \frac{\hbar^2}{2m}\left\{\chi_E(z)\frac{\partial\chi_{QD}(z)}{\partial z} - \chi_{QD}(z)\frac{\partial\chi_E(z)}{\partial z}\right\}_{z_0} \tag{A.2}$$

It is assumed that the motion of the carriers in the xy and z planes is separable and that z_0 lies in the potential barrier between the emitter and the QD

situated in the intrinsic region. If the confinement potential is much stronger in the z plane than the xy plane, which is a valid assumption for a QD, then the QD wave function may be written in the following variational form

$$\psi_{QD}(x,y,z) = e^{iqy}\varphi^0_{QD}(x,y)\chi^0_{QD}(z). \tag{A.3}$$

In this expression, q is a variational parameter dependent upon B_z and $\varphi^0_{QD}(x,y)\chi^0_{QD}(z)$ is the zero field state of the QD. The expectation value for $\hat{H}_{QD}$ for $\psi_{QD}(x,y,z)$ is given by

$$\langle\psi_{QD}|\hat{H}_{QD}|\psi_{QD}\rangle = E^0_{QD} + \frac{1}{2}m\omega_c^2\left[\left(l_0^2 q - z_{QD}\right)^2 + \left\langle\chi^0_{QD}|(z-z_{QD})^2|\chi^0_{QD}\right\rangle\right], \tag{A.4}$$

where $z_{QD} = \langle\chi^0_{QD}|z|\chi^0_{QD}\rangle$ is the expectation value of z at B=0, $\omega_c = \frac{eB}{m^*}$ is the cyclotron energy and $l_0 = \left(\frac{\hbar}{eB}\right)^{\frac{1}{2}}$. Minimising $\langle\psi_{QD}|\hat{H}_{QD}|\psi_{QD}\rangle$ with respect to the variational parameter, q, gives $q = \frac{z_{QD}}{l_0^2}$ and

$$\psi_{QD}(x,y,z) = e^{\frac{iyz}{l_0^2}}\varphi^0_{QD}(x,y)\chi^0_{Q0D}(z) \tag{A.5}$$

and

$$E_{QD} = E^0_{QD} + \frac{1}{2}m\omega_c^2\langle\chi^0_{QD}|(z-z_{QD})^2|\chi^0_{QD}\rangle \tag{A.6}$$

These expressions show clearly that the magnetic field induces an additional phase factor $exp\left[i\left(\frac{z_{0D}}{l_0^2}\right)y\right]$ in the wave function and a diamagnetic shift of the electron energy.

The emitter wave function can be described in three dimensions by the expression

$$\psi_E(x,y,z) = e^{ik_x x}e^{ik_y y}\chi_E(z), \tag{A.7}$$

where $\chi_E(z)$ satisfies the equation

$$\left[\frac{p_z^2}{2m} + V_E(z) + \frac{1}{2}m\omega_c^2(z-Z)^2\right]\chi_E(z) = \varepsilon\chi_E(z) \tag{A.8}$$

The centre coordinate of the emitter confining potential is characterised by $Z = l_0^2 k_y$, where the wave vector is given by $k_y = \frac{eB\Delta s}{\hbar}$. The electron motion along z is governed by the electrostatic confining potential, $V_e(z)$, arising from the barrier height and the diamagnetic magnetic cyclotron confinement energy $\frac{1}{2}m\omega_c^2(z-Z)^2$. Using the QD and emitter wave functions given by equations A.5 and A.7 respectively, the tunneling matrix element becomes

$$M = \int\int \varphi_{QD}^*(x,y)e^{ik_x x}exp\left[i\left(k_y - \frac{z_e}{l_0^2}\right)y\right]dxdy \tag{A.9}$$

$$M = \varphi_{QD}^0(k_x, k_y - \frac{z_{QD}}{l_0^2}). \tag{A.10}$$

where $\varphi^0_{0D}(k_x, k_y)$ is the two-dimensional Fourier transform of $\varphi^0_{QD}(x, y)$ and z_e is the coordinate of the edge of the emitter electron states. Carriers with orbits located at this position, i.e $k_y \sim \frac{z_e}{l_0^2}$, comprise the dominant contribution to tunneling current. This is because states with $k_y \gg \frac{z_e}{l_0^2}$ are empty and states with $k_y \ll \frac{z_e}{l_0^2}$ are located deep inside the emitter and have lower probability of tunneling into a QD. It is therefore predicted that the tunneling current, I, is proportional to the squared Fourier transform of the impurity wave function, giving

$$I \propto |MT|^2 = \left|\varphi^0_{QD}\left(k_x, \frac{z_e - z_{QD}}{l_0^2}\right)\right|^2 |T|^2 = \left|\varphi^0_{QD}\left(k_x, \frac{eB\Delta s}{\hbar}\right)\right|^2 |T|^2 \quad \text{(A.11)}$$

Appendix B

Material properties for energy level model

Property	GaAs	InAs	$In_xGa_{1-x}As$
Band gap at 4K (eV)	1.52[1]	0.52[2]	0.8747[3]
electron mass (m_e)	0.067[1]	0.022[1]	0.0498[3]
heavy hole mass (m_e)	0.5[1]	0.41[1]	0.5934[3]
light hole mass (m_e)	0.082[1]	0.026[1]	0.0704[3]

Table B.1: Material properties used for modeling in chapter 4. Here x denotes the indium concentration in the $In_xGa_{1-x}As$ and the superscripts 1, 2 and 3 refer to references [16, 113] and [114] respectively.

References

[1] Reed, M. A., Bate, R., et al. *J. Vac. Sci. Tech. B* **4**, 358 (1986).

[2] Takagahara, T. *Phys. Rev. B* **36**, 9293 (1987).

[3] Yoffe, A. D. *Adv. in Phys.* **50** (2001).

[4] Maksym, P. A. and Chakraborty, T. *Phys. Rev. Lett.* **65**, 108 (1990).

[5] McEuen, P. L. *Science* **278**, 1729 (1997).

[6] Reimann, S. M. and Manninen, M. *Rev. Mod. Phys.* **74**, 1283 (2002).

[7] Averin, D. V., Korotkov, A. N., and Likharev, K. K. *Phys. Rev. B* **44**, 6199 (1991).

[8] Johnson, N. F. and Payne, M. C. *Phys. Rev. B* **45**, 3819 (1992).

[9] Kouwenhoven, L. P., Vandervaart, N. C., et al. *Zeitschrift fur Physik B* **3**, 435 (1991).

[10] Johnson, A. T., Kouwenhoven, L. P., et al. *Phys. Rev. Lett.* **69**, 1592 (1992).

[11] Alhassid, Y. *Rev. Mod. Phys.* **72**, 895 (2000).

[12] Sohn, L. L., Kouwenhoven, L. P., and Schön, G. *Mesoscopic Electron Transport.* Springer, (1997).

[13] Leon, R., Fafard, S., et al. *App. Phys. Lett.* **67**, 521 (1995).

[14] Brunner, K., Bocklemann, U., et al. *Phys. Rev. Lett.* **69**, 3216 (1992).

[15] Petroff, P. M., Lorke, A., and Imamoglu, A. *Physics Today* **54**, 46 May (2001).

[16] Davies, J. H. *The Physics of Low Dimensional Semiconductors An Introduction.* Cambridge University Press, (1998).

[17] Tang, C. L. *Fundamental of Quantum Mechanics: For Solid State Electronics and Optics.* Cambridge University Press, (2005).

[18] Khitrova, G., Gibbs, H. M., et al. *Rev. Mod. Phys.* **71**, 1591 (1999).

[19] Tarucha, S., Honda, T., and Saku, T. *Solid State Comms.* **94**, 413 (1995).

[20] Randall, J. N., Reed, M. A., et al. *J. Vac. Sci. Tech. B* **6**, 302 (1988).

[21] Lee, K. Y., Kern, D. P., et al. *J. Vac. Sci. Tech. B* **8**, 1366 (1990).

[22] Kitada, H. and Arimoto, H. *Jap. J. Appl. Phys.* **31**, L990 (1992).

[23] Petroff, P. M. and Denbaars, S. P. *Superlattices and Microstructures* **15**, 15 (1994).

[24] Booker, G. R. and Joyce, B. A. *Phil. Mag.* **14**, 289 (1966).

[25] Barnham, K. and Vvedensky, D., editors. *Low-Dimensional Semiconductor Structures.* Cambrindge University Press, (2001).

[26] Gong, Q., Offermans, P., et al. *Appl. Phys. Lett.* **85**, 5697 (2004).

[27] Stangl, J., Holy, V., and Baur, G. *Rev. Mod. Phys.* **76**, 725 (2004).

[28] Chen, Y. H., Sun, J., et al. *Appl. Phys. Lett.* **88**, 0719303 (2006).

[29] McGee, W. M., Krzyewski, T. J., and Jones, T. S. *J. Appl. Phys.* **99**, 043505 (2006).

[30] Adler, F., Giger, M., et al. *J. Appl. Phys.* **83**, 1631 (1998).

[31] Henini, M., Sanguinetti, S., et al. *Microelectronics Journal* **28**, 933 (1997).

[32] Williamson, A. J. *International Journal of High Speed Electonics and Systems* **12**, 15 (2002).

[33] Medeiros-Ribeiro, G., Pikus, F. G., et al. *Phys. Rev. B* **55**, 1573 (1997).

[34] Warburton, R. J., Miller, B. T., et al. *Phys. Rev. B* **58**, 16 221 (1998).

[35] Cornet, C., Platz, C., et al. *Phys. Rev. B* **73**, 035342 (2005).

[36] Markussen, T., Kristensen, P., et al. *Phys. Rev. B* **74**, 195342 (2006).

[37] Stier, O., Grundmann, M., and Bimberg, D. *Phys. Rev. B* **59**, 5688 (1999).

[38] Williamson, A. J., Wang, L. W., and Zunger, A. *Phys. Rev. B* **62**, 12936 (2000).

[39] Granados, D. and Garcia, J. M. *Nanotechnelogy* **16**, S282 (2005).

[40] Cusack, M. A., Briddon, P. R., and Jaros, M. *Phys. Rev. B* **54**, R2300 (1996).

[41] Engström, O., Eghtedari, A., and Kaniewska, M. *Materials Science and Engineering* **27**, 936 (2007).

[42] Itskevich, I. E., Rybchenko, S. I., et al. *App. Phys. Lett.* **76**(26), 3932 (2000).

[43] Xu, X., Williams, D. A., and Cleaver, J. R. A. *App. Phys. Lett.* **85**(15), 3238 (2004).

[44] Imamoglu, A. and Yamamoto, Y. *Phys. Rev. Lett.* **72**, 210 (1994).

[45] Michler, P., Kiraz, A., et al. *Science* **290**, 2282 (2000).

[46] Yuan, Z., Kardynal, E., et al. *Science* **295**, 102 (2002).

[47] Harris, L., Mowbray, D. J., et al. *Appl. Phys. Lett.* **73**, 969 (1998).

[48] Liu, H. Y., Hopkinson, M., et al. *Appl. Phys. Lett.* **93**, 2931 (2003).

[49] Skolnick, M. S. and Mowbray, D. J. *Physica E* **21**, 155 (2004).

[50] Sugawara, M., Hatori, N., et al. *J. Phys. D: Appl. Phys.* **38**, 2126 (2005).

[51] Jiang, L., Lee, S. S., et al. *App. Phys. Lett.* **82**, 1986 (2003).

[52] Borgström, M. T., Zwiller, V., et al. *Nano Letters* **5**, 1439 (2005).

[53] Kroutvar, M., Ducommun, Y., et al. *App. Phys. Lett.* **83**, 443 (2003).

[54] Gershenfeld, N. and Chuang, L. *Scientific American* , 66 June (1998).

[55] Bennett, C. H. *Physics Today* , p.24 October (1995).

[56] Ricco, B. and Azbel, Y. *Phys. Rev. B* **29**, 1970 (1984).

[57] Ohnishi, H., Inata, T., et al. *Appl. Phys. Lett* **49**, 1248 (1986).

[58] Weil, T. and Vinter, B. *Appl. Phys. Lett.* **50**, 1281 (1987).

[59] Evans, B. *Optical and Magnetic Studies of p-i-n Resonant Tunneling Devices*. PhD thesis, University of Nottingham, (1995).

[60] Gobalto, Y., Chevoir, F., et al. *Phys. Rev. B* **43**, 4843 (1991).

[61] Davies, J. H., Hershfield, S., et al. *Phys. Rev. B* **47**, 4603 (1993).

[62] Horowitz, P. and Hill, W. *The Art of Electronics*. Cambridge University Press, 2nd edition, (1989).

[63] Hill, R. J. A. *Tunnelling into InAs Quantum Dots*. PhD thesis, University of Nottingham, (2002).

[64] Grundmann, M. http://my.ece.ucsb.edu/mgrundmann/bandeng.htm.

[65] Massies, J., Turco, F., et al. *J. Cryst. Growth* **80**, 307 (1987).

[66] Bogardus, E. H. and Bebb, H. B. *Phys. Rev.* **176**, 993 (1968).

[67] Hooft, G. W., van der Poel, W. A. J. A., and Molenkamp, L. W. *Phys. Rev. B* **35**, 8281 (1987).

[68] Pulizzi, F., Kent, A. J., et al. *App. Phys. Lett.* **84**, 3046 (2004).

[69] Adler, F., Geiger, M., et al. *J. Appl. Phys.* **80**, 4019 (1996).

[70] Blakesley, J. C., See, P., et al. *Phys. Rev. Lett.* **94**, 067401 (2005).

[71] Pulizzi, F., Walker, D., et al. *Phys. Rev. B* **72**, 085309 (2005).

[72] Endoh, A., Nakata, Y., et al. *Jpn. J. Appl. Phys* **38**, 1085 (1999).

[73] Jang, Y. D., Lee, H., et al. *J. Appl. Phys* **99**, 096101 (2006).

[74] Steer, M. J., Mowbray, D. J., et al. *Phys. Rev. B* **54**, 17738 (1996).

[75] Jung, M., Hirakawa, K., et al. *App. Phys. Lett.* **86**, 033106 (2005).

[76] Bimberg, D., Grundmann, M., et al. *Thin Solid Films* **267**, 32 (1995).

[77] Kamada, H., Temmyo, J., et al. *Jap. J. Appl. Phys* **36**, 4194 (1997).

[78] Mowbray, D. and Skolnick, M. S. *J. Phys. D: Appl. Phys.* **38**, 2059 (2005).

[79] Patanè, A., Hill, R. J. A., et al. *Phys. Rev. B* **65**, 165308 (2002).

[80] Morris, D., Perret, N., and Fafard, S. *App. Phys. Lett.* **75**(23) (1999).

[81] Brennan, K. F. *The Physics of Semiconductors with Applications to Optoelectronic Devices.* Cambridge University Press, (1999).

[82] Uskov, A. V., McInerney, J., et al. *Appl. Phys. Lett* **72**, 58 (1998).

[83] Ferreira, R. and Bastard, G. *App. Phys. Lett.* **74**(19), 2818 (1999).

[84] Brunkov, P. N., Patanè, A., et al. *Phys. Rev. B* **65**, 085326 (2002).

[85] Oulton, R., Finley, J. J., et al. *Phys. Rev. B* **68**, 235301 (2003).

[86] Turyanska, L., Baumgartner, A., et al. *App. Phys. Lett.* **89**, 092106 (2006).

[87] Auzel, F. *Chem. Rev.* **104**, 139 (2004).

[88] Quagliano, L. G. and Nather, H. *App. Phys. Lett.* **45**, 555 (1984).

[89] Paskov, P. P., Holtz, P. O., et al. *App. Phys. Lett.* **77**, 812 (2000).

[90] Pavesi, L. and Guzzi, M. *J. App. Phys.* **75**(10), 4779 (1994).

[91] Kiesslich, G., Wacker, A., et al. *Phys. Rev. B* **68**, 125331 (2003).

[92] Rakovicj, Y. P., Donegan, J. F., et al. *Physica E* **17**, 99 (2003).

[93] Kim, J. H., Kyhm, K., et al. *J. Appl. Phys.* **101**, 103108 (2007).

[94] Kammerer, C., Cassabois, G., et al. *Phys. Rev. Lett.* **87**(20), 207401 December (2001).

[95] Narvaez, G. A., Bester, G., and Zunger, A. *Phys. Rev. B* **74**, 075403 (2006).

[96] Schmidt, K. H. and Medeiros-Ribeiro, G. *Phys. Rev. B* **54**, 11346 (1996).

[97] Ortner, G., Oulton, R., et al. *Phys. Rev. B* **72**, 165353 (2005).

[98] Heitz, R., Born, H., et al. *Phys. Rev. B* **64**, 241305(R) (2001).

[99] Bogaart, E. W., Haverkort, J. E. M., et al. *Phys. Rev. B* **72**, 195301 (2005).

[100] Heitz, R., Born, H., et al. *App. Phys. Lett.* **68**, 361 (1996).

[101] Polimeni, A., Patanè, A., et al. *Phys. Rev. B* **59**, 5064 (1999).

[102] Verzelen, O., Ferreira, R., and Bastard, G. *Phys. Rev. B* **62**, R4809 (2000).

[103] Seidel, W., Titkov, A., et al. *Phys. Rev. Lett.* **73**, 2356 (1994).

[104] Sosnowski, T. S., Norris, T. B., et al. *Phys. Rev. B* **57**, R9423 (1998).

[105] Patanè, A., Levin, A., et al. *Phys. Rev. B* **62**, 11084 (2000).

[106] Magnusdottir, I., Bischoff, S., et al. *Phys. Rev. B* **67**, 205326 (2003).

[107] Ghosh, S., Bhattacharya, P., et al. *Appl. Phys. Lett.* **79**, 722 (2001).

[108] Larsson, M., Moskalenko, E. S., et al. *Phys. Rev. B* **74**, 245312 (2006).

[109] Baumgartner, A., Chaggar, A., et al. *Appl. Phys. Lett* **92**, 091121 (2008).

[110] Vdovin, E. E., Levin, A., et al. *Science* **290**, 122 (2000).

[111] Thomas, O., Makarovsky, O., et al. *Appl. Phys. Lett.* **90**, 082106 (2007).

[112] Bardeen, J. *Phys. Rev. Lett* **6**, 57 (1961).

[113] Levinshtein, M. and Rumyantsev, S., editors. *Handbook Series on Semiconductor Parameters*, volume 2. World Scientific, (1999).

[114] Pan, S. H., Shen, H., et al. *Phys. Rev. B* **38**, 3375 (1998).